

# Study of conserved quantities and their correlations in the RHIC Beam Energy Scan Program

*By*

**ARGHYA CHATTERJEE**

PHYS04201304005

Variable Energy Cyclotron Centre, Kolkata

*A thesis submitted to*

*The Board of Studies in Physical Sciences*

*In partial fulfillment of requirements*

*For the Degree of*

**DOCTOR OF PHILOSOPHY**

*of*

**HOMI BHABHA NATIONAL INSTITUTE**



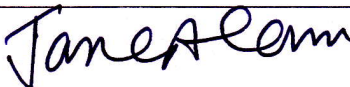
March, 2019

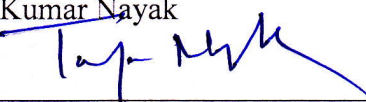


# Homi Bhabha National Institute<sup>1</sup>

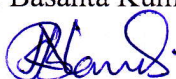
## Recommendations of the Viva Voce Committee

As members of the Viva Voce Committee, we certify that we have read the dissertation prepared by Arghya Chatterjee entitled "Study of conserved quantities and their correlations in the RHIC Beam Energy Scan Program" and recommend that it may be accepted as fulfilling the thesis requirement for the award of Degree of Doctor of Philosophy.

Chairman – Prof. Jane Alam  Date: 8/3/2019

Guide / Convener – Prof. Tapan Kumar Nayak  Date: 8/3/2019

Co-guide - <Name> (if any) Date:

\*Examiner – Prof. Basanta Kumar Nandi  Date: 14/03/2019

Member 1- Prof. Subhasish Chattopadhyay  Date: 8/3/2019  
 8/3/2019

Member 2- Prof. Sanjay Ghosh Date:

Final approval and acceptance of this thesis is contingent upon the candidate's submission of the final copies of the thesis to HBNI.

I/We hereby certify that I/we have read this thesis prepared under my/our direction and recommend that it may be accepted as fulfilling the thesis requirement.

Date: 8 March 2019

Place: Kolkata

  
<Signature>

Guide (Prof. Tapan Kumar Nayak)

<sup>1</sup> This page is to be included only for final submission after successful completion of viva voce.

\* I joined the thesis presentation of Mr. Arghya Chatterjee on March 08, 2019 at 4:00PM through SKYPE.  14/03/2019



## STATEMENT BY AUTHOR

This dissertation has been submitted in partial fulfillment of requirements for an advanced degree at Homi Bhabha National Institute (HBNI) and is deposited in the Library to be made available to borrowers under rules of the HBNI.

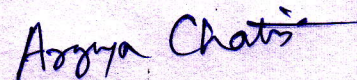
Brief quotations from this dissertation are allowable without special permission, provided that accurate acknowledgement of source is made. Requests for permission for extended quotation from or reproduction of this manuscript in whole or in part may be granted by the Competent Authority of HBNI when in his or her judgment the proposed use of the material is in the interests of scholarship. In all other instances, however, permission must be obtained from the author.

*Arghya Chatterjee*  
Arghya Chatterjee



## DECLARATION

I, hereby declare that the investigation presented in the thesis has been carried out by me. The work is original and has not been submitted earlier as a whole or in part for a degree / diploma at this or any other Institution / University.



Arghya Chatterjee



## List of Publications arising from the thesis

### List of Publications (As a Primary Authors):

- [1] **“Diagonal and off-diagonal susceptibilities of conserved quantities in relativistic heavy-ion collisions,”** \*
- A. Chatterjee, S. Chatterjee, T. K. Nayak and N. R. Sahoo.  
J. Phys. G **43**, no. 12, 125103 (2016)
- [2] **“Isothermal compressibility of hadronic matter formed in relativistic nuclear collisions,”** \*
- M. Mukherjee, S. Basu, A. Chatterjee, S. Chatterjee, S. P. Adhya, S. Thakur and T. K. Nayak,  
Phys. Lett. B **784**, 1 (2018)
- [3] **“Collision energy dependence of second-order off-diagonal and diagonal cumulants of net-charge, net-proton and net-kaon multiplicity distributions in Au+Au collisions,”** \*
- J. Adam *et al.* [STAR Collaboration],  
arXiv:1903.05370 [nucl-ex]. Submitted to Physics Review C.

### Conferences and Symposia

- [4] **“Study of Event-by-Event correlations of charge, baryon number and strangeness in heavy-ion collisions”** \*
- A. Chatterjee, S. Chatterjee, N. R. Sahoo and T. K. Nayak.  
Proceedings of the DAE-BRNS Symp. on Nucl. Phys. 60, 782 (2015)
- [5] **“Susceptibilities of conserved quantities in relativistic heavy-ion collisions at RHIC”** \*
- A. Chatterjee, N. R. Sahoo, S. Chatterjee and T. K. Nayak.  
Proceedings of the DAE-BRNS Symp. on Nucl. Phys. 61, 738 (2016).
- [6] **“Estimation of the isothermal compressibility from event-by-event multiplicity fluctuation studies”** \*

Maitreyee Mukherjee, Sumit Basu, Sanchari Thakur, Souvik P. Adhya, Arghya Chatterjee,  
Sandeep Chatterjee and Tapan K. Nayak  
EPJ Web of Conferences 171, 14010 (2018).

## List of STAR Collaboration Papers

- [7] **“Low- $p_T$   $e^+e^-$  pair production in Au+Au collisions at  $\sqrt{s_{NN}} = 200$  GeV and U+U collisions at  $\sqrt{s_{NN}} = 193$  GeV at STAR,”**  
J. Adam *et al.* [STAR Collaboration],  
Phys. Rev. Lett. **121**, no. 13, 132301 (2018)
- [8] **“Longitudinal Double-Spin Asymmetries for  $\pi^0$ s in the Forward Direction for 510 GeV Polarized  $pp$  Collisions,”**  
J. Adam *et al.* [STAR Collaboration],  
Phys. Rev. D **98**, no. 3, 032013 (2018)
- [9] **“Longitudinal double-spin asymmetries for dijet production at intermediate pseudorapidity in polarized  $pp$  collisions at  $\sqrt{s_{NN}} = 200$  GeV,”**  
J. Adam *et al.* [STAR Collaboration],  
Phys. Rev. D **98**, no. 3, 032011 (2018)
- [10] **“Global polarization of  $\Lambda$  hyperons in Au+Au collisions at  $\sqrt{s_{NN}} = 200$  GeV,”**  
J. Adam *et al.* [STAR Collaboration],  
Phys. Rev. C **98**, 014910 (2018)
- [11] **“ $J/\psi$  production cross section and its dependence on charged-particle multiplicity in  $p + p$  collisions at  $\sqrt{s} = 200$  GeV  $J/\psi$  production cross section and its dependence on charged-particle multiplicity in  $p + p$  collisions at  $\sqrt{s} = 200$  GeV,”**  
J. Adam *et al.* [STAR Collaboration],  
Phys. Lett. B **786**, 87 (2018)
- [12] **“Beam energy dependence of rapidity-even dipolar flow in Au+Au collisions,”**  
J. Adam *et al.* [STAR Collaboration],  
Phys. Lett. B **784**, 26 (2018)
- [13] **“Correlation Measurements Between Flow Harmonics in Au+Au Collisions at RHIC,”**

- J. Adam *et al.* [STAR Collaboration],  
Phys. Lett. B **783**, 459 (2018)
- [14] **“Azimuthal anisotropy in Cu+Au collisions at  $\sqrt{s_{NN}} = 200$  GeV,”**  
L. Adamczyk *et al.* [STAR Collaboration],  
Phys. Rev. C **98**, no. 1, 014915 (2018)
- [15] **“Transverse spin-dependent azimuthal correlations of charged pion pairs measured in  $p^\uparrow+p$  collisions at  $\sqrt{s} = 500$  GeV,”**  
L. Adamczyk *et al.* [STAR Collaboration],  
Phys. Lett. B **780**, 332 (2018)
- [16] **“Measurement of the  ${}^3_\Lambda\text{H}$  lifetime in Au+Au collisions at the BNL Relativistic Heavy Ion Collider,”**  
L. Adamczyk *et al.* [STAR Collaboration],  
Phys. Rev. C **97**, no. 5, 054909 (2018)
- [17] **“Collision Energy Dependence of Moments of Net-Kaon Multiplicity Distributions at RHIC,”**  
L. Adamczyk *et al.* [STAR Collaboration],  
Phys. Lett. B **785**, 551 (2018)
- [18] **“Beam-Energy Dependence of Directed Flow of  $\Lambda$ ,  $\bar{\Lambda}$ ,  $K^\pm$ ,  $K_s^0$  and  $\phi$  in Au+Au Collisions,”**  
L. Adamczyk *et al.* [STAR Collaboration],  
Phys. Rev. Lett. **120**, no. 6, 062301 (2018)
- [19] **“Azimuthal transverse single-spin asymmetries of inclusive jets and charged pions within jets from polarized-proton collisions at  $\sqrt{s} = 500$  GeV,”**  
L. Adamczyk *et al.* [STAR Collaboration],  
Phys. Rev. D **97**, no. 3, 032004 (2018)
- [20] **“Beam Energy Dependence of Jet-Quenching Effects in Au+Au Collisions at  $\sqrt{s_{NN}} = 7.7, 11.5, 14.5, 19.6, 27, 39,$  and  $62.4$  GeV,”**  
L. Adamczyk *et al.* [STAR Collaboration],  
Phys. Rev. Lett. **121**, no. 3, 032301 (2018)
- [21] **“Coherent diffractive photoproduction of  $\rho_0$  mesons on gold nuclei at 200 GeV/nucleon-pair at the Relativistic Heavy Ion Collider,”**

- L. Adamczyk *et al.* [STAR Collaboration],  
Phys. Rev. C **96**, no. 5, 054904 (2017)
- [22] **“Measurements of jet quenching with semi-inclusive hadron+jet distributions in Au+Au collisions at  $\sqrt{s_{NN}} = 200$  GeV,”**  
L. Adamczyk *et al.* [STAR Collaboration],  
Phys. Rev. C **96**, no. 2, 024905 (2017)
- [23] **“Bulk Properties of the Medium Produced in Relativistic Heavy-Ion Collisions from the Beam Energy Scan Program,”**  
L. Adamczyk *et al.* [STAR Collaboration],  
Phys. Rev. C **96**, no. 4, 044904 (2017)
- [24] **“Harmonic decomposition of three-particle azimuthal correlations at energies available at the BNL Relativistic Heavy Ion Collider,”**  
L. Adamczyk *et al.* [STAR Collaboration],  
Phys. Rev. C **98**, no. 3, 034918 (2018)
- [25] **“Measurement of  $D^0$  Azimuthal Anisotropy at Midrapidity in Au+Au Collisions at  $\sqrt{s_{NN}} = 200$  GeV,”**  
L. Adamczyk *et al.* [STAR Collaboration],  
Phys. Rev. Lett. **118**, no. 21, 212301 (2017)
- [26] **“Measurement of the cross section and longitudinal double-spin asymmetry for di-jet production in polarized  $pp$  collisions at  $\sqrt{s} = 200$  GeV,”**  
L. Adamczyk *et al.* [STAR Collaboration],  
Phys. Rev. D **95**, no. 7, 071103 (2017)
- [27] **“Dijet imbalance measurements in  $Au + Au$  and  $pp$  collisions at  $\sqrt{s_{NN}} = 200$  GeV at STAR,”**  
Phys. Rev. Lett. **119**, no. 6, 062301 (2017)  
L. Adamczyk *et al.* [STAR Collaboration],
- [28] **“ $\Upsilon$  production in U + U collisions at  $\sqrt{s_{NN}} = 193$  GeV measured with the STAR experiment,”**  
L. Adamczyk *et al.* [STAR Collaboration],  
Phys. Rev. C **94**, no. 6, 064904 (2016)

- [29] **“Charge-dependent directed flow in Cu+Au collisions at  $\sqrt{s_{NN}} = 200$  GeV,”**  
L. Adamczyk *et al.* [STAR Collaboration],  
Phys. Rev. Lett. **118**, no. 1, 012301 (2017)
- [30] **“Energy dependence of  $J/\psi$  production in Au+Au collisions at  $\sqrt{s_{NN}} = 39, 62.4$  and 200 GeV,”**  
L. Adamczyk *et al.* [STAR Collaboration],  
Phys. Lett. B **771**, 13 (2017)
- [31] **“Direct virtual photon production in Au+Au collisions at  $\sqrt{s_{NN}} = 200$  GeV,”**  
L. Adamczyk *et al.* [STAR Collaboration],  
Phys. Lett. B **770**, 451 (2017)
- [32] **“Jet-like Correlations with Direct-Photon and Neutral-Pion Triggers at  $\sqrt{s_{NN}} = 200$  GeV,”**  
L. Adamczyk *et al.* [STAR Collaboration],  
Phys. Lett. B **760**, 689 (2016)
- [33] **“Near-side azimuthal and pseudorapidity correlations using neutral strange baryons and mesons in d+Au, Cu+Cu and Au+Au collisions at  $\sqrt{s_{NN}} = 200$  GeV,”**  
B. Abelev *et al.* [STAR Collaboration],  
Phys. Rev. C **94**, no. 1, 014910 (2016)
- [34] **“ $J/\psi$  production at low transverse momentum in p+p and d+Au collisions at  $\sqrt{s_{NN}} = 200$  GeV,”**  
L. Adamczyk *et al.* [STAR Collaboration],  
Phys. Rev. C **93**, no. 6, 064904 (2016)
- [35] **“Measurement of elliptic flow of light nuclei at  $\sqrt{s_{NN}} = 200, 62.4, 39, 27, 19.6, 11.5,$  and 7.7 GeV at the BNL Relativistic Heavy Ion Collider,”**  
L. Adamczyk *et al.* [STAR Collaboration],  
Phys. Rev. C **94**, no. 3, 034908 (2016)

(\*) indicates papers on which this thesis is based.



Arghya Chatterjee



*Dedicated to my parents*



## ACKNOWLEDGEMENTS

I would like to thank my supervisor, Prof. Tapan K. Nayak, for his constant guidance, support, inspiration and encouragement for accomplishing my thesis. It is my privilege to work with you, Sir, for four years. I would like to express my sincere gratitude to Dr. Nihar R. Sahoo, Dr. Pritwish Tribedy and Dr. Sandeep Chatterjee for their continuous support, discussion, and encouragement for my understanding on experimental high energy physics, data analysis and most useful physics discussions. I am also fortunate to have Prof. Jane Alam, Prof. Subhasish Chattopadhyay, and Prof. Sanjay Ghosh as the members of my doctoral committee. I would like to thank them all for helpful suggestions and useful physics discussions. My especially thank to Dr. Swagota Mukherjee, Dr. Sayantan Sharma, Prof. Frithjof Karsch, Prof. Xiaofeng Luo, Prof. W. J. Llope, Prof. Gang Wang, Prof. Rene Bellwied, Prof. Jacquelyn Noronha-Hostler, Dr. Volodymyr Vovchenko for their support and discussion during data analysis. I thank all my fellow collaborators of the STAR experiment at RHIC. I am thankful to my seniors Dr. Sumit Basu, Dr. Maitreyee Mukherjee, Dr. Souvik Priyam Adhya, Dr. Sudipan De, Dr. Debojit Sarkar, Dr. Arindam Roy, Dr. Subikash Choudhury and Dr. Noor Alam for helping me with with advices and suggestions. I also take this opportunity to thank my friends Rajendra Nath Patra, Pingal Dasgupta, Somnath Mukhopadhyay, Prabrisa Das, Snigdha Ghosh, Md. Hasanujjaman and Vijay Iyer with whom I have enjoyed working together and spent lots of funny moments over the years. I would like to thank my juniors, numerous names to list, for their cooperation and friendly discussion.

I am fortunate to have a wonderful family that has been the source of endless love and support. I am grateful to my parents (Balaram Chatterjee & Tapasi Chatterjee) and Shilpa for their continuous and unwavering inspiration, and encouragement helped me a lot in the completion of the thesis.

  
Arghya Chatterjee



# Contents

<b>Synopsis</b>	<b>xxx</b>
<b>List of Figures</b>	<b>xli</b>
<b>List of Tables</b>	<b>xliii</b>
<b>1 Introduction</b>	<b>1</b>
1.1 Standard Model and QCD . . . . .	2
1.2 Quark-Gluon Plasma and QCD Phase Diagram . . . . .	4
1.3 Experimental signals of Quark-Gluon Plasma . . . . .	7
1.4 Signals for QCD phase transition . . . . .	16
1.4.1 Fluctuations in a thermal system . . . . .	17
1.4.2 Event-by-event fluctuations and correlations of conserved charges . . . . .	19
1.4.3 QCD phase transition and critical point study at RHIC . . . . .	20
1.5 Organization of the thesis . . . . .	23
<b>2 Cumulants of net-particle multiplicity distributions</b>	<b>25</b>
2.1 Cumulant-generating function . . . . .	25
2.1.1 Single variable cumulant-generating function . . . . .	26
2.1.2 Bivariate cumulant generating function . . . . .	29

2.2	Properties of the cumulants . . . . .	30
2.3	Cumulants in Heavy-Ion Collision . . . . .	31
2.3.1	Connection to thermodynamic susceptibilities . . . . .	32
2.4	Beam Energy Scan Program at RHIC . . . . .	35
<b>3</b>	<b>Estimation of susceptibilities of conserved charges from model calculations</b>	<b>39</b>
3.1	UrQMD and HRG Model . . . . .	40
3.2	Observables and methods . . . . .	43
3.3	Collision energy dependence of cumulant ratio . . . . .	45
3.4	Particle species dependence of cumulant . . . . .	46
3.5	Acceptance dependence of cumulant . . . . .	49
3.5.1	Acceptance dependence susceptibilities from HRG model . . . . .	51
3.5.2	Acceptance dependence cumulants from UrQMD model . . . . .	52
3.5.3	Normalized cumulants and susceptibilities from UrQMD and HRG . . . . .	53
<b>4</b>	<b>The Experimental Details</b>	<b>57</b>
4.1	Relativistic Heavy-Ion Collider (RHIC) . . . . .	57
4.2	The STAR detector . . . . .	58
4.2.1	The Time Projection Chamber (TPC) . . . . .	61
4.2.2	Time of Flight (TOF) . . . . .	67
<b>5</b>	<b>Analysis Details</b>	<b>71</b>
5.1	Data sets . . . . .	71
5.2	Event Selection . . . . .	73
5.3	Track Quality Cuts . . . . .	76
5.4	Collision Centrality Selection . . . . .	77

5.5	Particle Identification . . . . .	83
5.6	Centrality Bin width Correction . . . . .	88
5.7	Efficiency correction . . . . .	89
5.7.1	Efficiency Correction for moments/cumulants . . . . .	91
5.7.2	Efficiency estimation for protons and kaons . . . . .	94
5.7.3	Efficiency estimation for $Q^+$ and $Q^-$ . . . . .	97
5.8	Uncertainty estimation . . . . .	105
5.8.1	Statistical uncertainty . . . . .	105
5.8.2	Systematic uncertainties . . . . .	107
<b>6</b>	<b>Results from STAR data</b>	<b>111</b>
6.1	Net-particles multiplicity distributions and correlations . . . . .	111
6.2	Centrality dependence of diagonal and off-diagonal cumulants . . . . .	116
6.3	Pseudorapidity window dependence of cumulants . . . . .	118
6.4	Beam energy dependence cumulant ratios . . . . .	121
<b>7</b>	<b>Isothermal compressibility estimation from multiplicity fluctuations</b>	<b>125</b>
7.1	Observables . . . . .	126
7.2	Multiplicity fluctuations from experimental data . . . . .	128
7.3	Multiplicity fluctuations from event generators . . . . .	130
7.4	Isothermal compressibility from HRG model . . . . .	132
7.5	Compilation of $k_T$ . . . . .	134
7.6	Summary . . . . .	135
<b>8</b>	<b>Summary</b>	<b>137</b>

<b>Appendix A</b>	<b>Effect of <math>\Lambda</math> decay using UrQMD</b>	<b>141</b>
<b>Appendix B</b>	<b>Net <math>\pi</math>, K, p correlation</b>	<b>143</b>
<b>Bibliography</b>		<b>158</b>

# Synopsis

Quantum Chromodynamics (QCD), the theory of ‘strong’ interaction, predicts that at very high temperature and/or high density quarks and gluons will be no longer confined within the hadrons. This deconfined state of partons called the Quark-Gluon-Plasma (QGP) [1] might have existed within a few microseconds after the Big Bang. The QGP matter could be created in the laboratory by colliding heavy-ions at ultra-relativistic energies. The formation of QGP and the nature of phase transition from ordinary hadronic matter to the state of QGP have been studied experimentally by colliding  $Au + Au$  ions at the Relativistic Heavy-Ion Collider (RHIC), Brookhaven National Laboratory (BNL). To map the phase diagram in terms of the baryonic chemical potential ( $\mu_B$ ) and temperature ( $T$ ) as well as to understand the intricacies of the phase transition, the STAR experiment has collected large amount of data for  $Au + Au$  collisions during the year 2010, 2011, and 2014 as a part of the first phase of RHIC Beam Energy Scan (BES-I) program. At high baryon density the phase transition between hadronic matter to QGP phase is expected to be first order whereas, at high temperature and low  $\mu_B$ , the transition is a smooth cross over between the two phases. At the junction between crossover and first-order transition, the critical point (CP) of the phase diagram is expected. The subject matter of the thesis concentrates on exploring the phase diagram and the critical point by using fluctuations of conserved quantities.

One of the proposed methods to study the nature of the phase transition is through the study of the fluctuations of conserved quantities from their average values and the correlation among

them [2, 3]. Higher order cumulants ( $\kappa_\alpha^n[\delta N]$ ) of the net-baryon, net-charge, and net-strangeness multiplicity distributions are related to the higher order thermodynamic susceptibilities ( $\chi_\alpha^n$ ) of the respective conserved charges ( $\alpha$ ) [4, 5] and can be used to extract the signal of the presence of QCD CP [6]. In addition, the measured cumulants of different multiplicity distributions can be used to extract the freeze-out parameters ( $T$  and  $\mu_B$ ), at given collision energy and centrality, by comparing the data with lattice QCD and hadron resonance gas (HRG) calculations [7, 8, 9]. In past few years STAR and PHENIX experiment have measured such higher order diagonal cumulants of the net-proton (as an experimental proxy of net-baryon) [10], net-charge [7, 11] and net-kaon (the experimental proxy for the net-strangeness) [12].

Similar to the diagonal cumulants, the study of off-diagonal cumulants ( $\kappa_{\alpha,\beta}^{m,n}$ ) between the net-proton, net-kaon and net-charge multiplicity distributions in heavy-ion collision experiment provide complementary information. The off-diagonal cumulants are related to mixed susceptibilities ( $\chi_{\alpha,\beta}^{m,n}$ ) that carry the correlation between different flavors in QCD [13, 14]. The measurement of off-diagonal cumulants has specific advantages over diagonal cumulants. For the same order, the off-diagonal cumulants are more sensitive than the diagonal cumulants for distinguishing the partonic and hadronic phases [15]. The goal of this thesis is to study  $2^{nd}$  order off-diagonal and diagonal cumulants of net-proton, net-kaon and net-charge multiplicity distribution within same kinematic acceptance ( $|\eta| < 0.5$  and  $0.4 < p_T < 1.6$  GeV/C) in  $Au + Au$  collisions at RHIC energies.

In the STAR experiment at RHIC, the charge particles can be identified on an event-by-event basis over a large transverse momentum range ( $p_T$ ) with high precisions. As it is not possible to identify neutral baryons on an event-by-event basis and event-by-event reconstruction of higher mass baryon and strangeness has its limitations, we use proxy in diagonal cumulants analysis. On the other hand, measurements of off-diagonal cumulants such as  $\kappa_{Q,B}^{m,n}$  or  $\kappa_{Q,S}^{m,n}$  are

less affected by the experimental inability to measure neutral baryons or neutral strange particles, as they do not contribute to such correlations. They can be approximated as  $\kappa_{Q,B}^{m,n} \approx \kappa_{Q,p}^{m,n}$  and  $\kappa_{Q,S}^{m,n} \approx \kappa_{Q,k}^{m,n}$  [1]. However,  $\kappa_{B,S}^n$  cannot be simply approximated by  $\kappa_{p,k}^n$  although one expects a reasonable connection between two quantities [16]. Measurement of  $\kappa_{p,k}^n$ , therefore, provides access to essential albeit qualitative features of a rapid change of baryon-strangeness correlations near the transition region as predicted in [17]. We will also discuss how the off-diagonal cumulants provide further constraint in freezeout parameters [18, 19]. Observables of this analysis include both diagonal and off-diagonal susceptibilities [20] such that  $\chi_\alpha^2 = \frac{1}{VT^3}\sigma_\alpha^2$  and  $\chi_{\alpha,\beta}^{1,1} = \frac{1}{VT^3}\sigma_{\alpha,\beta}^{1,1}$ . Here,  $V$  and  $T$  are the volume and temperature of the system.  $\alpha, \beta$  represent net-charge ( $Q = Q^+ - Q^-$ ), net-proton ( $p = p - \bar{p}$ ), and net kaon ( $k = k^+ - k^-$ ). The diagonal and off-diagonal cumulants are defined as  $\sigma_\alpha^2 = \langle (N_\alpha - \langle N_\alpha \rangle)^2 \rangle$  and,  $\sigma_{\alpha,\beta}^{1,1} = \langle (N_\alpha - \langle N_\alpha \rangle)(N_\beta - \langle N_\beta \rangle) \rangle$ . Here  $\langle \cdot \rangle$  denotes the ensemble average.

In the thesis work, data analysis have been performed for eight different collision energies,  $\sqrt{s_{NN}} = 7.7, 11.5, 14.5, 19.6, 27, 39, 62.4, 200$  GeV in  $Au + Au$  collisions which are recorded by the STAR experiment [21] during the first phase of RHIC BES run. The charge particle Identification has done using ionization energy loss mechanism ( $dE/dx$ ) in the Time Projection Chamber (TPC) at lower momentum range. At higher momentum range, an additional mass<sup>2</sup> cut is used using Time of Flight (ToF) detector to identify protons, pions or kaons. The measured cumulants of net multiplicity distributions need to be corrected for finite detector efficiencies. Embedding Monte Carlo simulation techniques have been used to obtain the efficiencies. It is found that the detection efficiency of protons range from 60-80%, kaons from 30-50% and unidentified charges particles from 70-85%. Efficiency correction is done by assuming the binomial efficiency response of the detectors [22]. Additionally, the centrality bin width correction (CBWC) has been used to suppress artificial fluctuations in multiplicity due to the selection of wide centrality bins. Estimation of

uncertainties in the measurement is one of the most crucial aspects of any experimental analysis. Uncertainties in the measurements are mainly classified in two types, one is the statistical uncertainty representing the precision of the experimental results and the second one is the systematic uncertainty, which represents the accuracy of the measurement. The statistical uncertainty estimation is based on the numerical error propagation method of multivariate cumulants [23]. The systematic uncertainties are estimated by varying different track quality cuts, tracking efficiency and conditions for particle identification.

A detailed analysis task has been taken up as a part of the thesis work. The final results of diagonal and off-diagonal cumulants have been obtained for all collision energies and collision centralities. We observe that both diagonal and off-diagonal cumulants increase linearly as a function of  $\Delta\eta$ -window for all eight BES energies Au+Au collisions up to our experimental acceptance.  $\sigma_{p,k}^{1,1}$  shows negative values towards larger  $\Delta\eta$ -window which may imply that the anti-correlation between net-proton and net-kaon increases with acceptance window. The diagonal cumulants of net-charge, net-proton and net-kaon increase as a function of  $\langle N_{\text{part}} \rangle$  because of the increase in system volume as a function of centrality. The width of net-proton distribution decreases as a function of beam energy in a central collision because of baryon stopping at lower energies. The correlations between net-charge – net-kaon and net-charge – net-proton increase with centrality. On the contrary, there is a growing anti-correlation behaviour observed between net-proton and net-kaon with centrality. At low beam energy ( $\sqrt{s_{\text{NN}}} < 27$  GeV) this correlation becomes positive. The centrality dependence of the off-diagonal cumulants  $\sigma_{Q,k}^{1,1}$  and  $\sigma_{Q,p}^{1,1}$  are very similar to that of the diagonal cumulants. To explore the excess correlation in  $\sigma_{Q,k}^{1,1}$  and  $\sigma_{Q,p}^{1,1}$  compared to the self-correlation, we also study the ratios of off-diagonal to diagonal cumulants defined:  $C_{p,k} = \sigma_{p,k}^{1,1}/\sigma_k^2$ ,  $C_{Q,p} = \sigma_{Q,p}^{1,1}/\sigma_p^2$ , and  $C_{Q,k} = \sigma_{Q,k}^{1,1}/\sigma_k^2$ . The ratio,  $C_{\alpha,\beta}$ , also referred to as "Koch ratio", is motivated by [17]. The trivial system volume dependence of the cumulants is also expected to cancel in

such ratios. An excess correlation between net-proton and net-charge and between net-charge and net-kaon is observed in comparison to self-correlation between net-protons and net-kaons. The values of  $C_{Q,p}$  and  $C_{Q,k}$  are observed to increase with beam energy, and this increasing trend cannot be explained in HRG and UrQMD model calculations. These correlations may have origins in the partonic phases. But it is very difficult to pin down the exact origin, and more theoretical input is needed to see if the excess correlations, seen for  $C_{Q,p}$  and  $C_{Q,k}$ , indeed come from the resonance states that have not been included in the existing hadronic models. In this work, a complete set of systematic studies is reported for different  $\Delta\eta$  acceptance and different collision centrality for eight BES energies in RHIC. This systematic study provides useful input to constrain the freezeout parameters that help map the QCD phase diagram.

A detailed simulation study has been carried out as a part of the thesis using the Hadron Resonance Gas (HRG) and Ultra-relativistic Quantum molecular dynamics (UrQMD) models [16] in a broad range of energies from  $\sqrt{s_{NN}}= 4$  GeV to 200 GeV. UrQMD is a microscopic transport model [24], which has been quite successful in explaining heavy-ion collision experimental data. HRG model consists of all hadron and resonances listed in the Particle Data Book within the framework of a multiple species, non-interacting, ideal gas in complete thermal and chemical equilibrium [25]. We have studied the particle species dependence for all second order susceptibilities using a different combination of particle sets. We have made a comprehensive study of the effect of conserved quantities in full phase space. An acceptance ( $|\eta_{max}| \leq 0.5$ ) is ideal for observing grand canonical fluctuations [16]. Suitably normalized susceptibilities show a conserved charge ordering in the transverse momentum acceptance in HRG as well as in UrQMD.

In addition, as a part of the thesis work, an estimation of isothermal compressibility ( $k_T$ ) at the chemical freeze-out has been carried out using experimentally observed quantities [26].  $k_T$  is related to the fluctuation in particle multiplicity. The dynamical part from the observed multi-

plicity fluctuation is extracted by removing the contribution from the variation of participating nucleons [27]. In the existing available data, we have observed a constant  $k_T$  as a function of collision energy within the uncertainties. We compared the results with the calculation from AMPT, UrQMD, EPOS event generators and estimated the  $k_T$  for Pb+Pb collision at the CERN Large Hadron Collider. We have used HRG model to estimate the isothermal compressibility for a wide range of collision energy. It is observed that the  $k_T$  values decrease up to 20 GeV, beyond which it remains almost constant. This indicates that the collision system is more compressible at lower energies compared to higher energies.

# Bibliography

- [1] P. Braun-Munzinger and J. Stachel, *Nature* **448**, 302 (2007). doi:10.1038/nature06080
- [2] F. Karsch and K. Redlich, *Phys. Lett. B* **695**, 136 (2011) doi:10.1016/j.physletb.2010.10.046  
[arXiv:1007.2581 [hep-ph]].
- [3] J. Randrup, V. Koch and A. Majumder, *AIP Conf. Proc.* **842**, 95 (2006).  
doi:10.1063/1.2220199
- [4] M. A. Stephanov, *Phys. Rev. Lett.* **102**, 032301 (2009) doi:10.1103/PhysRevLett.102.032301  
[arXiv:0809.3450 [hep-ph]].
- [5] M. Asakawa, S. Ejiri and M. Kitazawa, *Phys. Rev. Lett.* **103**, 262301 (2009)  
doi:10.1103/PhysRevLett.103.262301 [arXiv:0904.2089 [nucl-th]].
- [6] M. A. Stephanov, K. Rajagopal and E. V. Shuryak, *Phys. Rev. D* **60**, 114028 (1999)  
doi:10.1103/PhysRevD.60.114028 [hep-ph/9903292].
- [7] L. Adamczyk *et al.* [STAR Collaboration], *Phys. Rev. Lett.* **113**, 092301 (2014)  
doi:10.1103/PhysRevLett.113.092301 [arXiv:1402.1558 [nucl-ex]].
- [8] A. Bazavov *et al.*, *Phys. Rev. Lett.* **109**, 192302 (2012) doi:10.1103/PhysRevLett.109.192302  
[arXiv:1208.1220 [hep-lat]].

- [9] S. Borsanyi, Z. Fodor, S. D. Katz, S. Krieg, C. Ratti and K. K. Szabo, Phys. Rev. Lett. **111**, 062005 (2013) doi:10.1103/PhysRevLett.111.062005 [arXiv:1305.5161 [hep-lat]].
- [10] L. Adamczyk *et al.* [STAR Collaboration], Phys. Rev. Lett. **112**, 032302 (2014) doi:10.1103/PhysRevLett.112.032302 [arXiv:1309.5681 [nucl-ex]].
- [11] A. Adare *et al.* [PHENIX Collaboration], Phys. Rev. C **93**, no. 1, 011901 (2016) doi:10.1103/PhysRevC.93.011901 [arXiv:1506.07834 [nucl-ex]].
- [12] L. Adamczyk *et al.* [STAR Collaboration], Phys. Lett. B **785**, 551 (2018) doi:10.1016/j.physletb.2018.07.066 [arXiv:1709.00773 [nucl-ex]].
- [13] R. V. Gavai and S. Gupta, Phys. Rev. D **73**, 014004 (2006) doi:10.1103/PhysRevD.73.014004 [hep-lat/0510044].
- [14] A. Majumder and B. Muller, Phys. Rev. C **74**, 054901 (2006) doi:10.1103/PhysRevC.74.054901 [nucl-th/0605079].
- [15] F. Karsch, Nucl. Phys. A **967**, 461 (2017) doi:10.1016/j.nuclphysa.2017.06.011 [arXiv:1706.01620 [hep-lat]].
- [16] A. Chatterjee, S. Chatterjee, T. K. Nayak and N. R. Sahoo, J. Phys. G **43**, no. 12, 125103 (2016) doi:10.1088/0954-3899/43/12/125103 [arXiv:1606.09573 [nucl-ex]].
- [17] V. Koch, A. Majumder and J. Randrup, Phys. Rev. Lett. **95**, 182301 (2005) doi:10.1103/PhysRevLett.95.182301 [nucl-th/0505052].
- [18] P. Alba, W. Alberico, R. Bellwied, M. Bluhm, V. Mantovani Sarti, M. Nahrgang and C. Ratti, Phys. Lett. B **738**, 305 (2014) doi:10.1016/j.physletb.2014.09.052 [arXiv:1403.4903 [hep-ph]].

- 
- [19] J. Noronha-Hostler, R. Bellwied, J. Gunther, P. Parotto, A. Pasztor, I. P. Vazquez and C. Ratti, arXiv:1607.02527 [hep-ph].
- [20] M. Cheng *et al.*, Phys. Rev. D **79**, 074505 (2009) doi:10.1103/PhysRevD.79.074505 [arXiv:0811.1006 [hep-lat]].
- [21] K. H. Ackermann *et al.* [STAR Collaboration], Nucl. Instrum. Meth. A **499**, 624 (2003). doi:10.1016/S0168-9002(02)01960-5
- [22] X. Luo, Phys. Rev. C **91**, no. 3, 034907 (2015) Erratum: [Phys. Rev. C **94**, no. 5, 059901 (2016)] doi:10.1103/PhysRevC.91.034907, 10.1103/PhysRevC.94.059901 [arXiv:1410.3914 [physics.data-an]].
- [23] Kendall, Maurice G, Advanced Theory Of Statistics Vol-I, 1943, [Charles Griffin: London]
- [24] S. A. Bass *et al.*, Prog. Part. Nucl. Phys. **41**, 255 (1998) [Prog. Part. Nucl. Phys. **41**, 225 (1998)] doi:10.1016/S0146-6410(98)00058-1 [nucl-th/9803035].
- [25] A. Andronic, P. Braun-Munzinger and J. Stachel, Nucl. Phys. A **772**, 167 (2006) doi:10.1016/j.nuclphysa.2006.03.012 [nucl-th/0511071].
- [26] M. Mukherjee, S. Basu, A. Chatterjee, S. Chatterjee, S. P. Adhya, S. Thakur and T. K. Nayak, Phys. Lett. B **784**, 1 (2018) doi:10.1016/j.physletb.2018.07.021 [arXiv:1708.08692 [nucl-ex]].
- [27] H. Heiselberg, Phys. Rept. **351**, 161 (2001) doi:10.1016/S0370-1573(00)00140-X [nucl-th/0003046].



# List of Figures

1.1	Overview of the standard model. Reproduced from <a href="https://cds.cern.ch/record/1473657?ln=de">https://cds.cern.ch/record/1473657?ln=de</a>	3
1.2	Summary of measurements of $\alpha_s(q)$ as a function of energy scale $q$ [6]. . . . .	5
1.3	The pressure (left panel) and energy density (right panel) in QCD as a function of temperature for three different flavor degrees of freedom. The arrows indicate the Stefan-Boltzmann limit in both the figures. Reproduced from reference [10]. . . . .	6
1.4	Schematic of the QCD phase diagram. Reproduced from <a href="http://www.gauss-centre.eu/gauss-centre">http://www.gauss-centre.eu/gauss-centre</a> . . . . .	6
1.5	Columbia plot for the QCD phase diagram at $\mu_B = 0$ as a function of the degenerate quark mass $m_{ud}$ and $m_s$ . Reproduced from [16]. . . . .	7
1.6	Direct photon measurements for $p+p$ and $Au+Au$ collisions at RHIC. Reproduced from reference [17]. . . . .	9
1.7	The enhancement factor for (multi-)strange particles in $Au+Au$ and $Cu+Cu$ collisions at $\sqrt{s_{NN}} = 200$ GeV. This figure has been taken from reference [19]. . . . .	10
1.8	$J/\psi$ versus $R_{AA}$ for $Au+Au$ collisions at $\sqrt{s_{NN}} = 200$ GeV. This figure has been taken from reference [22]. . . . .	12

1.9	<i>Left panel:</i> the nuclear modification factor ( $R_{AB}$ ) as a function of transverse momentum for $d + Au$ and $Au + Au$ collisions and <i>Right panel:</i> two particle azimuthal correlation of $p + p$ , $d + Au$ and $Au + Au$ collisions. This figure has been taken from reference [25]. . . . .	13
1.10	Schematic diagram for the initial-state anisotropy in the collision zone converting into the final-state elliptic flow measured as anisotropy in particle momentum. This figure has been taken from reference [26]. . . . .	14
1.11	Measurement of $v_2$ for identified particles as a function of $p_T$ at RHIC. This figure has been taken from reference [30]. . . . .	15
1.12	Elliptic flow of hadrons scaled by the constituent quarks number as a function of $p_T/n_q$ and $(m_T - m_0)/n_q$ . This figure has been taken from reference [31]. . . . .	15
1.13	Sketch of the various rapidity scales relevant to conserved charge fluctuation in Heavy-ion collisions. The figure is taken form [41]. . . . .	19
1.14	The collision energy dependence $\kappa\sigma^2$ of net-charge (top left), net-proton (bottom right) and net-kaon (bottom left) multiplicity distribution in $Au + Au$ collisions are measured in STAR experiment. The $\kappa\sigma^2$ of net-charge from PHENIX experiment is presented in the top right panel. The figure is taken from [54]. . . . .	21
2.1	Visual example of distribution with positive/negative skewness (left panel) and positive/negative kurtosis (right panel). Reproduced from [69]. . . . .	28
2.2	Graphical example of positive/negative and null $2^{nd}$ -order off-diagonal cumulants. . . . .	30
2.3	The correlation coefficients $C_{BS}$ and $C_{QS}$ in a hadron gas at $\mu_B = \mu_Q = \mu_S = 0$ and from lattice calculation at $\mu = 0$ (Ref. [57]). The value of $T_c$ is assumed to lie in the range $T_c = 170 \pm 10$ . The figure is from [58]. . . . .	33
2.4	. . . . .	34

2.5	A schematic of the QCD phase diagram. $T_{ch}$ , and $\mu_B$ based on the statistical model fit to the measured particle ratios. The yellow curves show the estimated trajectories of the possible collision energies at RHIC. The figure is taken from [76]. . . . .	35
2.6	Energy dependence of the chemical freeze-out parameters $T$ and $\mu_B$ . The figure is taken from reference [78]. . . . .	37
3.1	Collision energy dependence of "Koch ratios" for central (0-5%) Au+Au collisions predicted by the HRG and UrQMD models. Error bars are within the marker size in URQMD calculations. . . . .	45
3.2	Particle species dependence diagonal and off-diagonal susceptibilities and their ratios in central (0-5%) Au+Au collisions using the UrQMD model calculations. . . . .	47
3.3	The measurements for $C_{SQ}$ and $C_{BQ}$ are robust under the different choices of the particle set for central (0-5%) Au+Au collisions. . . . .	48
3.4	Ratios of net baryon (top panel) and total baryon (bottom panel) numbers within the analysis acceptance (system size) to the full phase space (bath + system) for 0-5% central Au+Au collisions as a function of $\sqrt{s_{NN}}$ using the UrQMD model. The results are presented for three different $\eta$ windows. . . . .	50
3.5	The $p_T$ -acceptance dependence of the second-order off-diagonal and diagonal susceptibilities in the HRG model for central Au+Au collisions at $\sqrt{s_{NN}} = 7.7, 39$ and 200 GeV. . . . .	50
3.6	The $\eta$ -acceptance dependence of the second-order off-diagonal and diagonal susceptibilities in the HRG model for central Au+Au collisions at $\sqrt{s_{NN}} = 7.7, 39$ and 200 GeV. . . . .	51

3.7	The $p_T$ -acceptance dependence of the second-order off-diagonal and diagonal susceptibilities in the UrQMD model for 0-5% central Au+Au collisions at $\sqrt{s_{NN}}= 7.7, 39$ and 200 GeV. . . . .	52
3.8	The $\eta$ -acceptance dependence of the second-order off-diagonal and diagonal susceptibilities in the UrQMD model for 0-5% central Au+Au collisions at $\sqrt{s_{NN}}= 7.7, 39$ and 200 GeV. . . . .	53
3.9	The $p_T$ -acceptance dependence second-order diagonal and off-diagonal susceptibilities and cumulants normalized by their values at $p_{T_{max}} = 2$ GeV and $ \eta_{max}  < 0.5$ for central Au+Au collisions at $\sqrt{s_{NN}} = 7.7$ GeV (upper panel) and 200 GeV (lower panel) for both the HRG and UrQMD model. . . . .	54
3.10	The maximum $p_T$ -acceptance dependence of the second-order susceptibility normalized by the value for $p_{T_{max}} = 2$ GeV and $\eta_{max} = 0.5$ for a single particle system for three different masses of the particle. . . . .	55
3.11	The $\eta_{max}$ dependence of all second-order diagonal and off-diagonal susceptibilities normalized by their values for $p_{T_{max}} = 2$ GeV and $\eta_{max} = 0.5$ in the UrQMD and HRG models. . . . .	56
4.1	A schematic of the RHIC accelerator complex layout . . . . .	59
4.2	STAR detector system layout. . . . .	60
4.3	The three-dimensional schematic diagram of the STAR TPC. . . . .	61
4.4	A cutaway view of the Outer and Inner field cage. . . . .	63
4.5	Schematic of a single anode sector of the TPC. . . . .	64
4.6	The energy loss distribution for charge particles in the STAR TPC. . . . .	67
4.7	A scale drawing of the locations of pVPD and TOFp detectors. . . . .	68

4.8	Momentum dependence of the particle identification capabilities of a TOF system with a time resolution of 100 ps . . . . .	69
4.9	TOF $1/\beta$ as a function of momentum from 200 GeV $d + Au$ collisions . . . . .	70
5.1	Analysis Flow-chart. . . . .	72
5.2	Distribution of z-component of event vertex for eight different center-of-mass energies. Shaded portion represents the acceptance cuts used in this analysis. . . . .	74
5.3	TOF match as a function of reference multiplicity. The red line corresponds to the pile-up rejection cut. . . . .	75
5.4	Run by Run QA for 200 GeV $Au + Au$ collisions $\langle \text{Refmult} \rangle$ and $\langle \phi \rangle$ . . . . .	75
5.5	Distribution of transverse plane component of event vertex for different centre-of-mass energies. . . . .	76
5.6	NFitsPoints and DCA distributions for Au+Au 39 GeV . . . . .	77
5.7	An illustration of the nucleus-nucleus collision. . . . .	78
5.8	An illustration of a Glauber MC event for $Au + Au$ collisions at $\sqrt{s_{NN}} = 200$ GeV with impact parameter $b = 6$ fm viewed (a) in the transverse plane and (b) along the beam axis. The nucleons are drawn with a radius $\sqrt{\sigma_{NN}/\pi}/2$ . Participating nucleons ( $N_{part}$ ) are represented by darker disks and the lighter circle represents spectator. The figures are taken from [24]. . . . .	79
5.9	An illustrated example of the correlation of the final state observable total charged particle multiplicity $N_{ch}$ with Glauber-calculated quantities ( $b, N_{part}$ ). The figure is taken from [24]. . . . .	79
5.10	$\eta$ vs $p_T$ distributions for Au+Au 39 GeV . . . . .	81
5.11	Efficiency uncorrected reference multiplicity (Refmult2) distributions for $Au + Au$ collisions at eight different BES energies. . . . .	82

5.12	Illustration of traditional particle physics experiment components [110]. . . . .	83
5.13	Track $dE/dx$ vs momentum distribution for different centre-of-mass energies. . . . .	86
5.14	TOF Mass square vs momentum distribution for different center-of-mass energies. . . . .	87
5.15	Diagonal and off-diagonal cumulants for 5% (0-5%,.....75-80%) and 10% (0-10%,.....70-80%) centrality bins with CBWC correction for Au+Au collisions at $\sqrt{s_{NN}} = 7.7$ GeV. . . . .	89
5.16	Diagonal and off-diagonal cumulants for 5% (0-5%,.....75-80%) and 10% (0-10%,.....70-80%) centrality bins with CBWC correction for Au+Au collisions at $\sqrt{s_{NN}} = 7.7$ GeV. . . . .	90
5.17	An illustrated example of incident and detected particle distribution with 50% detection efficiency. The incident particles are distributed according normal distribution. . . . .	91
5.18	Top: Number of MC tracks and matched pairs for positive kaons in 0-5% central Au + Au collisions at $\sqrt{s_{NN}} = 200$ GeV; Bottom: estimated pair efficiency vs $p_T$ . . . . .	95
5.19	$p_T$ dependence TPC tracking efficiencies for $\pi^+, k^+, p$ at Au + Au 39 GeV. . . . .	96
5.20	$p_T$ dependence TOF matching efficiencies for $\pi^+, k^+, p$ at Au + Au 39 GeV. . . . .	96
5.21	$p_T$ dependence TPC tracking, TOF matching and combined efficiencies for $\pi^+, k^+, p$ at Au+Au 39 GeV. . . . .	97
5.22	$p_T$ dependence $p$ and $\bar{p}$ efficiencies . . . . .	98
5.23	$p_T$ dependence $k^+$ and $k^-$ efficiencies. . . . .	98
5.24	Average charge particle efficiencies for 39 GeV. . . . .	104

5.25	$p_T$ average protons, kaons, and charge particle efficiencies as a function of centrality in Au+Au collisions. For charge and proton in lower $p_T$ range ( $0.4 < p_T < 0.8$ GeV/c) only TPC is used. For kaons ( $0.4 < p_T < 1.6$ GeV/c) and proton in higher $p_T$ range ( $0.8 < p_T < 1.6$ GeV/c) both TPC and TOF are used. Solid points for positive particle and open points for negative particle. . . . .	104
5.26	Systematic uncertainty estimation flowchart . . . . .	107
5.27	$\langle \text{net-proton} \rangle$ as a function of different systematic cuts . . . . .	108
5.28	Systematic variation of $C_{p,k}$ , $C_{Q,k}$ and $C_{Q,p}$ for different cuts at Au+Au 7.7 (top row), 39 (middle row), and 200 (bottom row) GeV. . . . .	109
6.1	Efficiency uncorrected net-proton ( $\Delta p = p - \bar{p}$ ) multiplicity distributions in Au+Au collisions at $\sqrt{s_{NN}} = 7.7, 11.5, 14.5, 19.6, 27, 39, 62.4$ and 200 GeV measured within kinematic range $ \eta  < 0.5$ and $0.4 < p_T < 1.6$ GeV/c in three different centralities (0-5%, 30-40%, and 60-70%). . . . .	113
6.2	Efficiency uncorrected net-kaon ( $\Delta k = k^+ - k^-$ ) multiplicity distributions in Au+Au collisions at $\sqrt{s_{NN}} = 7.7, 11.5, 14.5, 19.6, 27, 39, 62.4$ and 200 GeV measured within kinematic range $ \eta  < 0.5$ and $0.4 < p_T < 1.6$ GeV/c in three different centralities (0-5%, 30-40%, and 60-70%). . . . .	113
6.3	Efficiency uncorrected net-pion ( $\Delta \pi = \pi^+ - \pi^-$ ) multiplicity distributions in Au+Au collisions at $\sqrt{s_{NN}} = 7.7, 11.5, 14.5, 19.6, 27, 39, 62.4$ and 200 GeV measured within kinematic range $ \eta  < 0.5$ and $0.4 < p_T < 1.6$ GeV/c in three different centralities (0-5%, 30-40%, and 60-70%). . . . .	114

6.4	Efficiency uncorrected net-charge ( $\Delta Q = Q^+ - Q^-$ ) multiplicity distributions in $Au + Au$ collisions at $\sqrt{s_{NN}} = 7.7, 11.5, 14.5, 19.6, 27, 39, 62.4$ and $200$ GeV measured within kinematic range $ \eta  < 0.5$ and $0.4 < p_T < 1.6$ GeV/c in three different centralities (0-5%, 30-40%, and 60-70%). . . . .	114
6.5	Efficiency uncorrected net-proton ( $\Delta p$ ) vs net-kaon ( $\Delta k$ ) multiplicity distributions in $Au + Au$ collisions at $\sqrt{s_{NN}} = 7.7, 11.5, 14.5, 19.6, 27, 39, 62.4$ and $200$ GeV measured within kinematic range $ \eta  < 0.5$ and $0.4 < p_T < 1.6$ GeV/c in 0-5% central collisions. . . . .	115
6.6	Efficiency uncorrected net-kaon ( $\Delta k$ ) vs net-charge ( $\Delta Q$ ) multiplicity distributions in $Au + Au$ collisions at $\sqrt{s_{NN}} = 7.7, 11.5, 14.5, 19.6, 27, 39, 62.4$ and $200$ GeV measured within kinematic range $ \eta  < 0.5$ and $0.4 < p_T < 1.6$ GeV/c in 0-5% central collisions. . . . .	115
6.7	Efficiency uncorrected net-proton ( $\Delta p$ ) vs net-charge ( $\Delta Q$ ) multiplicity distributions in $Au + Au$ collisions at $\sqrt{s_{NN}} = 7.7, 11.5, 14.5, 19.6, 27, 39, 62.4$ and $200$ GeV measured within kinematic range $ \eta  < 0.5$ and $0.4 < p_T < 1.6$ GeV/c in 0-5% central collisions. . . . .	116
6.8	Centrality dependence of 2nd order diagonal cumulants (variances) of net-proton, net-kaon and net-charge (top to bottom) for Au+Au collisions at $\sqrt{s_{NN}} = 7.7, 11.5, 14.5, 19.6, 27, 39, 62.4$ and $200$ GeV (left to right). Error bars are statistical and box are systematic errors. The red dashed lines represent scaling predicted by central limit theorem. . . . .	117

- 6.9 Centrality dependence of second-order off-diagonal cumulants of net-proton, net-charge and net-kaon for Au+Au collisions at  $\sqrt{s_{NN}}= 7.7, 11.5, 14.5, 19.6, 27, 39, 62.4$  and 200 GeV (left to right). Error bars are statistical and box are systematic errors. The red dashed lines represent scaling predicted by central limit theorem. . . . . 118
- 6.10 Centrality dependence of 2nd order off-diagonal to diagonal cumulants ratios of net-proton, net-charge and net-kaon for Au+Au  $\sqrt{s_{NN}}= 7.7, 11.5, 14.5, 19.6, 27, 39, 62.4$  and 200 GeV (left to right) within kinematic range  $|\eta| < 0.5$  and  $0.4 < p_T < 1.6$  GeV/c. Error bars are statistical and box are systematic errors. The red dashed lines represent UrQMD points. . . . . 119
- 6.11  $|\eta|$  acceptance dependence of  $2^{nd}$  order diagonal ( $\sigma_Q^2, \sigma_p^2, \sigma_k^2$ ) and off-diagonal ( $\sigma_{p,k}^{11}, \sigma_{Q,p}^{11}, \sigma_{Q,k}^{11}$ ) cumulants of net-proton ( $p$ ), net-charge ( $Q$ ) and net-kaon ( $k$ ) for Au+Au collisions at  $\sqrt{s_{NN}} = 7.7, 11.5, 14.5, 19.6, 27, 39, 62.4$  and 200 GeV (left to right). The vertical bars represent statistical uncertainties. Red lines represent UrQMD 0-5% points. . . . . 120
- 6.12  $|\eta|$  acceptance dependence mean of net-proton, net-charge and net-kaon for Au+Au collisions at  $\sqrt{s_{NN}} = 7.7, 11.5, 14.5, 19.6, 27, 39, 62.4$  and 200 GeV (left to right). Error bars are statistical error. . . . . 120
- 6.13 Beam energy dependence of off-diagonal to diagonal cumulants ratios of net-charge and net-proton (upper panel) and for net-charge and net-kaon (lower panel) for Au+Au collisions at  $\sqrt{s_{NN}}= 7.7, 11.5, 14.5, 19.6, 27, 39, 62.4$  and 200 GeV. Vertical line and box represent statistical and systematic error, respectively. The broken lines represent the Poisson baseline. The band represents the UrQMD results for 0-5% central collisions. . . . . 121

7.1	Collision-energy dependence of $\omega_{ch}$ of charged particle multiplicity distributions for central (0-5%) A+A collisions from the available experimental data [135, 129, 130, 131, 134]. The statistical component has been shown using participant model. The dynamical fluctuation is obtained by subtraction the statistical component from the measured values. . . . .	128
7.2	Collision energy dependence of $\omega_{ch}$ of multiplicity distributions for 0-5% central A + A (Au+Au or Pb+Pb) collisions for AMPT (both DEF and SM), UrQMD and EPOS. The dynamical multiplicity fluctuations ( $\omega_{ch,dyn}$ ) are obtained after subtracting the statistical fluctuations from participant model. . . . .	131
7.3	Isothermal compressibility ( $k_T$ ) for available experimental data for 0-5% central Au+Au (Pb+Pb) collisions as a function of collision energy. Results for presented for three different event generators, AMPT, UrQMD and EPOS. A uniform pseudo-rapidity cut ( $ \eta  < 0.5$ ) has been maintained for all cases. Results from HRG calculations are superimposed. . . . .	134
A.1	Effect of $\Lambda^0$ decay on second order diagonal and off-diagonal cumulants of net-proton, net-charge and net-kaon multiplicity distributions for Au+Au collisions at $\sqrt{s_{NN}} = 7.7$ (open markers) and 200 (solid markers) GeV using UrQMD model. .	141
A.2	Effect of $\Lambda^0$ decay on average $p$ and $\bar{p}$ as a function of $\langle N_{part} \rangle$ for Au+Au collisions at $\sqrt{s_{NN}} = 7.7$ (open markers) and 200 (solid markers) GeV using UrQMD model.	142
B.1	Centrality and acceptance dependence of $2^{nd}$ -order diagonal and off-diagonal cumulants of net-pion, net-kaon and net-proton multiplicity distributions for Au + Au collisions at $\sqrt{s_{NN}} = 7.7, 11.5, 14.5, 19.6, 27, 39, 62.4$ and 200 GeV. Error bars are statistical. . . . .	144

- B.2 Beam energy dependence of the ratios of off-diagonal to diagonal cumulants net-charge and net-proton (upper panel) and for net-pion and net-kaon (lower panel) for Au+Au collisions at  $\sqrt{S_{NN}}= 7.7, 11.5, 14.5, 19.6, 27, 39, 62.4$  and 200 GeV. . 145



# List of Tables

2.1	RHIC operating modes for BES-I program and proposed data that will be obtained during BES-II. . . . .	37
3.1	The chemical freezeout parameters extracted from mid-rapidity data at different $\sqrt{s_{NN}}$ [87, 44]. . . . .	42
5.1	Trigger ID's of Beam Energy Scan phase-I . . . . .	73
5.2	Event selection cuts used in BES-I energies . . . . .	74
5.3	Event selection cuts used in BESI energies . . . . .	76
5.4	Refmult2 cuts for centrality selection used in BES-I energies . . . . .	82
5.5	Particle identification cuts used in this analysis. . . . .	85
5.6	Average efficiency ( $\langle\varepsilon\rangle$ ) values for $p$ , $\bar{p}$ , $k^+$ , $k^-$ , $Q^+$ , and $Q^-$ for two different $p_T$ bin and $Q^-$ at $\sqrt{s_{NN}} = 7.7, 11.5, 14.5, 19.6, 27, 39, 62.4,$ and $200$ GeV in different centralities. . . . .	103



# Chapter 1

## Introduction

According to the Big Bang theory, at the very beginning of time, the Universe was a singularity with infinite energy density. At around 13.8 billion years ago just after the Big Bang the Universe started expanding and underwent several types of phase transitions. At that time, the matter-energy was so hot and dense that all fundamental forces were unified as a single force. As time evolved, roughly  $10^{-43}$  seconds to  $10^{-36}$  seconds after the singularity, the gravitational force decoupled first, then the strong force decoupled from the electroweak force ( $10^{-35}$  seconds to  $10^{-10}$  seconds), and the Universe underwent a sudden expansion known as cosmic inflation. It is believed that elementary particles such as photons, gluons, and quarks were created as a result of the inflation. After electro-weak decoupling, when the Universe reached the age of nanosecond to the microsecond, it consisted mostly of a soup of quark, gluons, and other elementary particles, in a state of phase called quark-gluon plasma (QGP). Further expansion and cooling caused the transition from the QGP to a hadron phase after which no bare quark would be found. In the 1970s, [1] Quantum Chromodynamics (QCD) was established to describe the theory of strong interaction. QCD predicts that a deconfined system of weakly interacting quarks and gluons can exist at a very high energy density ( $1 \text{ GeV}/fm^3$ ) and high temperature. High energy heavy-ion

collision experiments are built to discover this quark-gluon plasma state by creating enormous high energy/temperature due to the collision of two highly relativistic ionized heavy ions. In normal/low temperature and pressure, quarks are confined within hadrons by the inter-quark potential.

## 1.1 Standard Model and QCD

As indicated by Standard Model (SM), our present understanding of the visible Universe is that the fundamental constituents of matter are quarks, leptons, Higgs bosons, gauge bosons, and their antiparticles as shown in Fig. 1.1. The dynamics of these fundamental particles are described by the quantum field theories (QFT), like Electroweak and QCD theory. The electromagnetic and weak interactions can be described as the electroweak theory in a unified way. QCD is developed to describe the strong interaction between quarks and gluons. QCD is a non-Abelian gauge theory, has two very important properties: *Asymptotic freedom*; and *Color Confinement*.

### Color Confinement and Asymptotic freedom

The discovery of baryons with three same flavors (like  $\Omega^-(sss)$ ,  $\Delta^-(ddd)$  and  $\Delta^{++}(uuu)$ ) required an additional quantum number in order to fulfil the Pauli Exclusion principle within the quark model [2]. Three colors (an additional quantum number) states are assigned to the quark flavors (named red, green, and blue), whereas the hadrons remain colorless. There are eight different gluons, and the gluon exchange can change the color state of a quark but not its flavor. This is analogous to the exchange of photons in the electromagnetic force between charge particles. In QCD, the potential  $V_{q\bar{q}}$  for a quark and anti-quark pair can be approximated by [3],

$$V_{q\bar{q}} = -\frac{4}{3} \frac{\alpha_s(q^2)}{r} + kr. \quad (1.1)$$

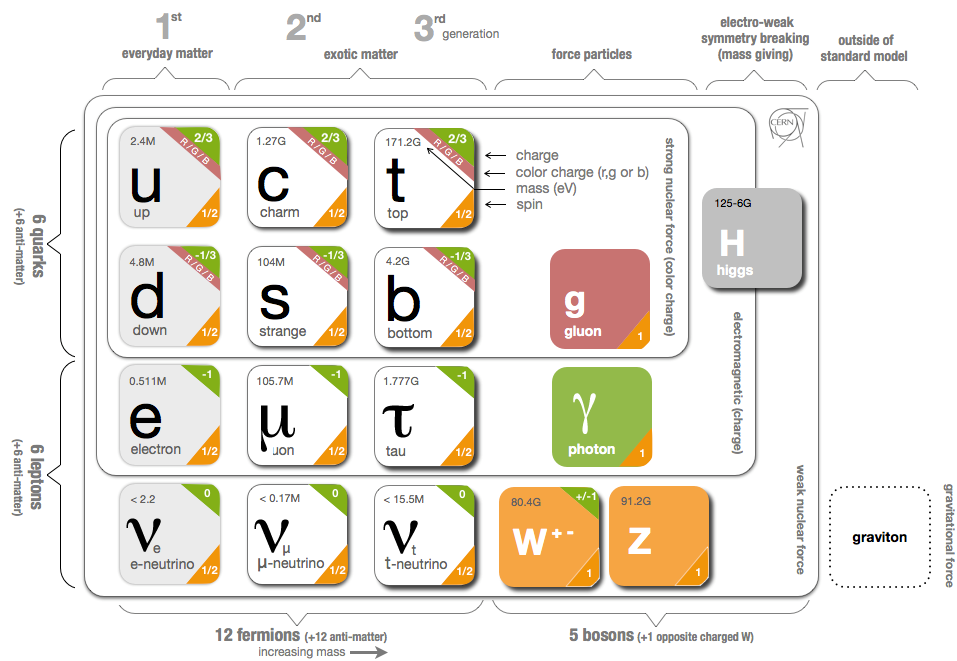


Figure 1.1: Overview of the standard model. Reproduced from <https://cds.cern.ch/record/1473657?ln=de>

The first term in equation 1.1 is the Coulomb-like part and the second term is called the confinement term, where the  $\alpha_s(q^2)$  is the running coupling constant of the strong interaction, which changes with the square of the 4-momentum transfer ( $q^2$ ) and  $r$  is the distance between  $q\bar{q}$  pair.  $k \approx 1$  GeV/fm [3] is the color string tension. It describes the potential energy stored in the string when the quark-antiquark pair is being pulled apart. If the potential energy stored in the string reaches a sufficient value, another  $q\bar{q}$  pair can be created spontaneously.

Another essential property of quantum chromodynamics is asymptotic freedom. This property was discovered by David Gross and Frank Wilczek [4] and independently by David Politzer [5] in 1973. The effective coupling constant ( $\alpha_s$ ) can be expressed as,

$$\alpha_s(q^2) = \frac{12\pi}{(33 - 2N_f)\log(q^2/\Lambda_{QCD}^2)}, \quad (1.2)$$

where,  $N_f$  is the number of quark flavors and  $\Lambda_{QCD}$  is the QCD scale parameter, which is  $\sim 200$  MeV. Figure 1.2 demonstrates that for high momentum transfer ( $q^2 \rightarrow \infty$ ), the partons are weakly interacting and asymptotically free (i.e.,  $\alpha_s(q^2) \rightarrow 0$ ). This implies that in this limit, quarks behave as free non-interacting particles. As a consequence, at very high temperature the QCD medium is predicted to be a gas of free quarks and gluons.

## 1.2 Quark-Gluon Plasma and QCD Phase Diagram

The discovery of asymptotic freedom suggests that at very high momentum transfer, there is a possibility of Quark-Gluon Plasma (QGP) [7, 8] formation. Under the condition of high enough temperature, around  $T_c \approx 150$  MeV (which is equivalent to  $\approx 10^{12}$  K), the interaction among quarks and gluons within hadrons become very weak. As a result, they behave like quasi-free particles.

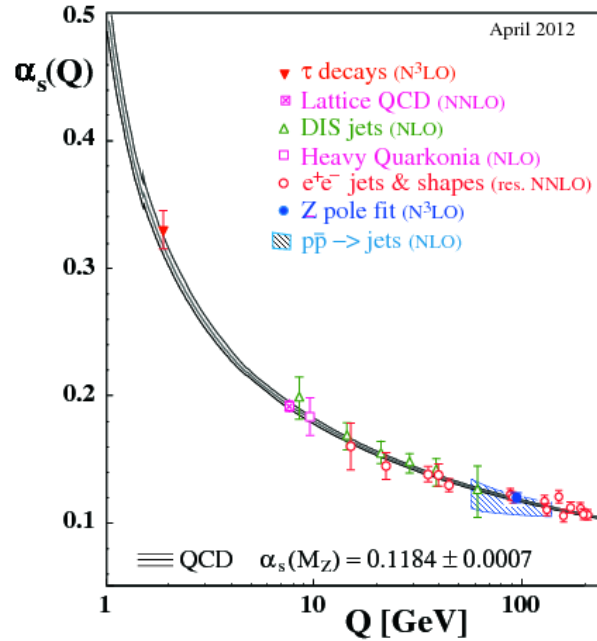


Figure 1.2: Summary of measurements of  $\alpha_s(q)$  as a function of energy scale  $q$  [6].

Additionally, if the nuclear matter density is high enough ( $\epsilon \approx 1 \text{ GeV}/\text{fm}^3$ ) [9], the hadrons begin to overlap and may form a system of quarks and gluons. A phase transition occurs when the intensive parameters (like temperature, pressure, the chemical potential of the matter) varied to a critical value. The transition properties can be characterized by a thermodynamic potential (such as free energy) and its derivative w.r.t. these intensive parameters. In the finite volume limit, if there exists a finite discontinuity in the first derivative of free energy, then the transition is called 1<sup>st</sup>-order phase transition. A first-order phase transition is associated with mixed-phase regimes. If the second derivative of the free energy is discontinuous, then the transition is known as a second order phase transition. If no such discontinuity were encountered, the transition is said to be a cross-over.

Figure 1.3 shows the pressure and energy density as a function of temperature predicted by lattice QCD calculations. The  $P$  and  $T$  are calculated for 2, 2+1, and 3 flavor QCD after normalized with  $T^4$  [10]. The energy density ( $\epsilon = gT^4$ ) is proportional to the system degrees of freedom

(g). The quantity  $\epsilon/T^4$  changes steeply when the temperature approaches the critical transition temperature  $T_c$  around 173 MeV. Latest lattice QCD calculations show that  $T_c$  could be even lower, around 154 MeV [11].

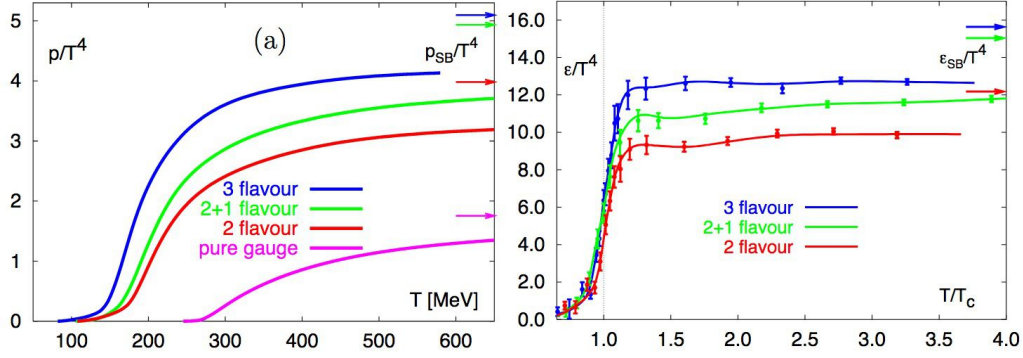


Figure 1.3: The pressure (left panel) and energy density (right panel) in QCD as a function of temperature for three different flavor degrees of freedom. The arrows indicate the Stefan-Boltzmann limit in both the figures. Reproduced from reference [10].

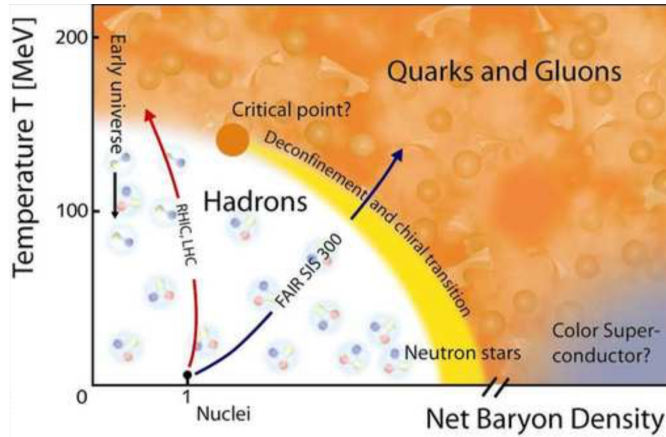


Figure 1.4: Schematic of the QCD phase diagram. Reproduced from <http://www.gauss-centre.eu/gauss-centre>.

Figure 1.4 shows a schematic of the QCD phase diagram in  $T-\mu_B$  plane, where  $\mu_B$  is defined as the amount of energy needed to add or remove an additional baryon in the system. At low  $\mu_B$  a crossover might take place within  $T_c = 150-170$  MeV [12, 13]. At higher  $\mu_B$  region, QCD calculation indicates that the transition is first order [14]. At the end of the first order line, a critical point may

exist. At extremely large baryon density ( $\mu_B \gg \Lambda_{QCD}$ ), the coupling become asymptotically free, which leads to the formation of color superconductor at low temperature, analogous to Cooper pair in condensed matter [15]. Quark mass, flavor and color play an important role in the order of the phase transition [16]. In the limit of infinite quark mass ( $m_q \rightarrow \infty$ ) at  $\mu_B = 0$ , the transition from hadronic to deconfined state is first order. At  $m_q \rightarrow 0$ , it is also a first-order transition for  $u, d$  and  $s$  quark flavor. At intermediate quark masses, the phase transition from confinement to deconfinement is a crossover.

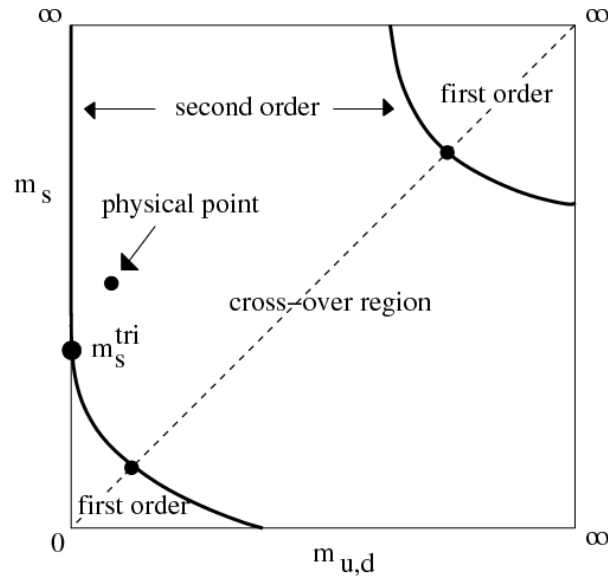


Figure 1.5: Columbia plot for the QCD phase diagram at  $\mu_B = 0$  as a function of the degenerate quark mass  $m_{u,d}$  and  $m_s$ . Reproduced from [16].

### 1.3 Experimental signals of Quark-Gluon Plasma

The search for QGP started about four decades ago at the Bevalac accelerator located at the Lawrence Berkeley National Laboratory, USA, where a gold beam of 1 GeV/nucleon was bombarded on a fixed  $Au$  target. Soon this experiment followed by a series of experiments at the Alternate Gradient Synchrotron (AGS) at BNL, USA and at the Super Proton Synchrotron (SPS)

at CERN, Switzerland. From the year 2000, a dedicated facility for QGP search became operational at Relativistic Heavy-Ion Collider (RHIC) at BNL. Data collected by the RHIC experiments for Au-Au collisions at top-RHIC energy provided compelling evidence for the formation of a new state of matter.

The system created in these collisions undergoes several stages during evolution, including a pre-equilibrium, thermalization, a mixed phase of partons and hadrons, a hadron gas phase and last free streaming of hadrons. Each stage is related to specific associated properties depending upon their production mechanism and carry corresponding signals. The thermal stage of the system is very short-lived ( $\sim 5\text{-}10$  fm/c) and can not be observed directly in the experiment. Nonetheless various probes can be used to extract the bulk properties of the medium. In the next few paragraphs, I will briefly discuss a few of them.

### **Electromagnetic probe**

Direct photons and dileptons radiation are considered to be a valuable probe for QGP diagnostic. They are emitted from the entire space-time volume of the medium, whereas the hadrons are emitted from the corresponding freeze-out surface. Besides, they interact only via electromagnetic interaction. As a result, their mean free path is much larger, and they are expected to come out from the medium without undergoing much collisions with the medium. So photons and dileptons carry the precise information of the state of the thermal medium where they are produced. The main challenge in detecting them comes from the vast background of photons from hadron decays, predominantly from the two-photon decays of neutral pions and mesons. However, in the thermal region ( $p_T$  range, 1-4 GeV/c), a much larger excess of photons is observed in  $Au + Au$  collisions compared to  $p + p$  collision, as shown in Fig. 1.6, whereas for  $p_T$  range above 4 GeV there is no clear enhanced observed. Also, the inverse slope parameter measured by RHIC  $\sim 221$  MeV, is well

above the transition temperature ( $T_c$ ) of 150-160 MeV.

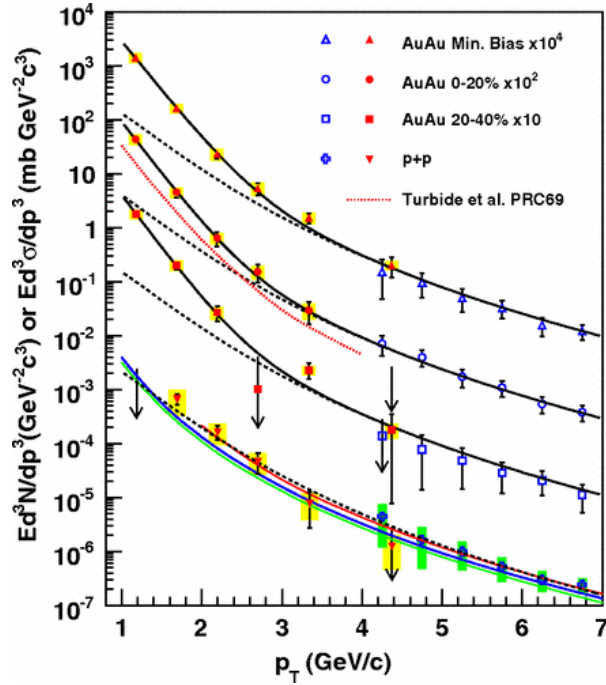


Figure 1.6: Direct photon measurements for  $p + p$  and  $Au + Au$  collisions at RHIC. Reproduced from reference [17].

## Strangeness Enhancement

At normal temperature and pressure, nuclear matter contains only up and down quarks. The strangeness particle is produced at sufficiently high temperature. Strangeness enhancement is considered one of the key signatures of QGP formation in the heavy-ion collision [18]. In QGP it is expected that the threshold energy required to produce a  $s\bar{s}$  pair would be much smaller compared to elementary hadronic collisions. As a result, the relative (anti)hyperon production is more abundant in heavy-ion collisions compared to  $p + p$  or  $p + A$  collisions [19].

Figure 1.7 shows the relative production of strange hadrons for  $Au + Au$  and  $Cu + Cu$  collisions at  $\sqrt{s_{NN}} = 200\text{GeV}$  compared to the production observed in  $p + p$  collisions as a function of  $\langle N_{part} \rangle$ .

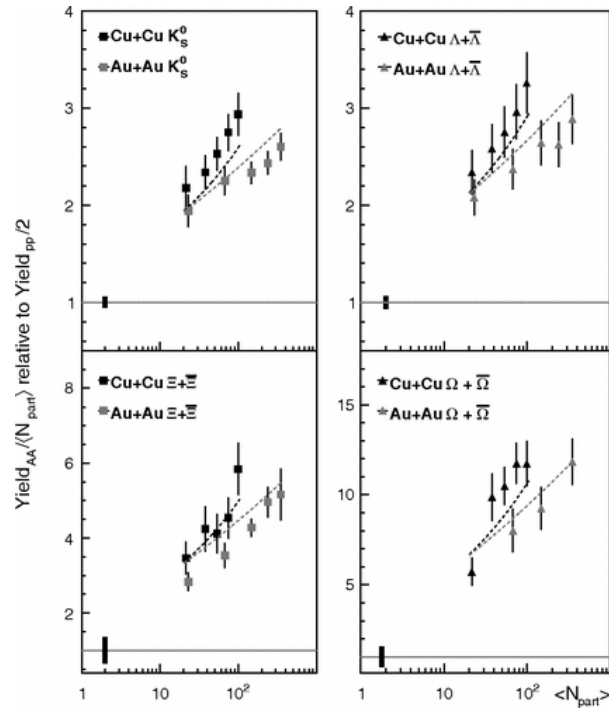


Figure 1.7: The enhancement factor for (multi-)strange particles in  $Au+Au$  and  $Cu+Cu$  collisions at  $\sqrt{s_{NN}} = 200$  GeV. This figure has been taken from reference [19].

The enhancement strange particle yields compared to elementary collisions hints to the formation of a dense medium in these collisions.

### Quarkonium Suppression

Quarkonia particles are consist of bound states of heavy quarks (like charm and bottom). They are produced early in collisions, and their survival is affected by the medium. Suppression of quarkonia production in heavy-ion collisions compared to  $p + p$  collisions are an important probe of the QGP [20]. In the partonic state, the color charge of heavy quarks is screened due to the presence of quarks and gluons of the medium. Due to the screening effect, interactions between heavy quarks and anti-quarks are diluted. Pairs are broken up into open charm or bottom particles and coupled with other lighter quarks inside the QGP medium. The magnitude of the suppression depends on the binding energies of the quarkonia and the temperature of the system. At RHIC, the  $J/\psi$  (a bound state of  $c\bar{c}$ ) production was studied in  $Au + Au$  collisions [21, 22]. Figure 1.8 shows the  $p_T$  integrated normalized  $J/\psi$  yield ratios for  $p + p$  and  $Au + Au$  collisions (defined by  $R_{AA}$ ) as a function  $\langle N_{part} \rangle$ . In central  $Au + Au$  collisions, a significant  $J/\psi$  suppression relative to the p+p collisions was observed.

### Jet Quenching

Jets are collimated beams of energetic partons. High momentum particles, ( $p_T > 4-5$  GeV), are generally considered to be produce via hard process [23]. In p+p collisions, dijets, consisting of a pair of jets, are formed with back to back momenta and both are carrying an equal amount of energy. In heavy-ion collisions, if dijets are produced near fireball surface, then one of two jets traverses the medium and lose more energy than the other which is emitted away from the fireball without interactions. This phenomenon is known as jet-quenching and described by the nuclear

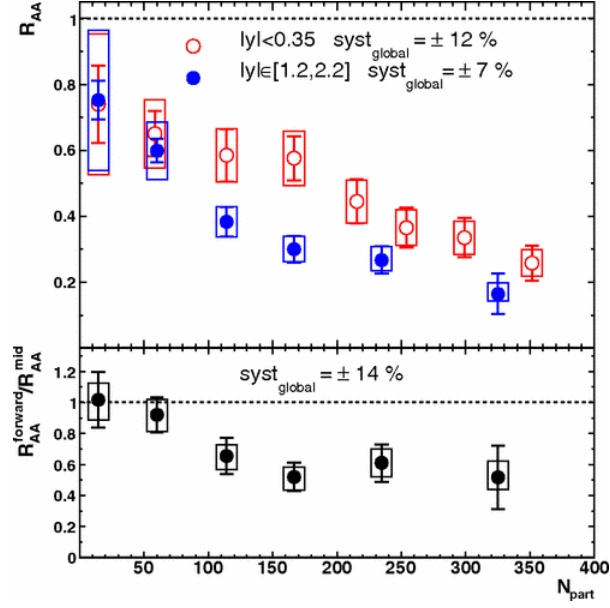


Figure 1.8:  $J/\psi$  versus  $R_{AA}$  for  $Au + Au$  collisions at  $\sqrt{s_{NN}} = 200$  GeV. This figure has been taken from reference [22].

modification factor ( $R_{AB}$ ),

$$R_{AB} = \frac{d^2 N_{AB}/dp_T d\eta}{T_{AB} d^2 \sigma_{pp}/dp_T d\eta}, \quad (1.3)$$

where  $T_{AB} = \langle N_{bin} \rangle / \sigma_{incl}^{pp}$  is the nuclear thickness function and  $\langle N_{bin} \rangle$  is the average number of binary collision calculated from Glauber Model [24] for a specific collision centrality.

Figure 1.9 shows nuclear modification factor (left panel) and the two particles azimuthal distribution (right panel) measured in  $d + Au$  and  $Au + Au$  collisions at RHIC.  $R_{AB}$  shows a strong suppression in 200 GeV central  $Au + Au$  collisions compared to  $d + Au$  collisions at the higher  $p_T$  region. The high  $p_T$  particles production is suppressed due to partonic energy-loss in the dense medium. This further indicates the production of a hot and dense medium in central  $Au + Au$  collisions. The right panel plot in Fig. 1.9 displays the two particles azimuthal distributions measured

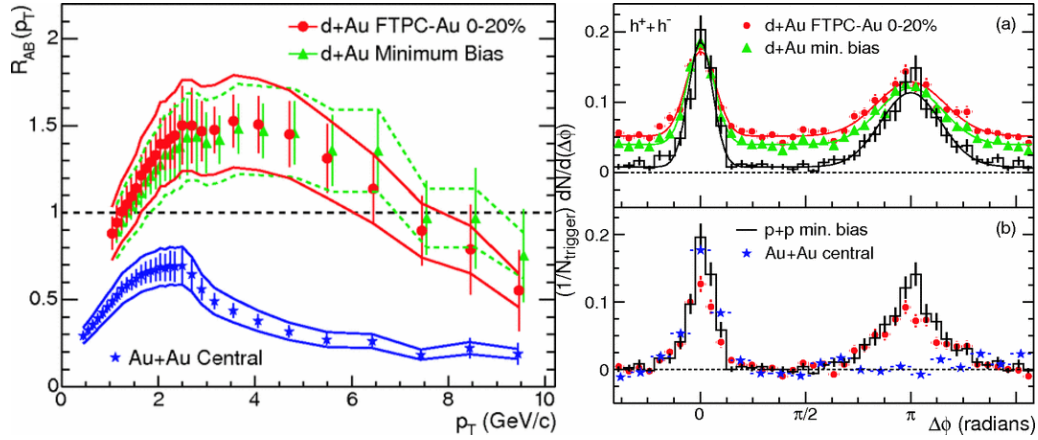


Figure 1.9: *Left panel*: the nuclear modification factor ( $R_{AB}$ ) as a function of transverse momentum for  $d + Au$  and  $Au + Au$  collisions and *Right panel*: two particle azimuthal correlation of  $p + p$ ,  $d + Au$  and  $Au + Au$  collisions. This figure has been taken from reference [25].

with various collision systems. The azimuthal distribution shows an enhancement in the near-side ( $\Delta\phi = 0$ ) compares to the away-side ( $\Delta\phi = \pi$ ). This comprehensive study strongly indicates the formation of quark-gluon plasma in high energy heavy-ion collisions.

## Collective flow

In non-central heavy-ion collisions, the overlap region of two colliding nuclei is spatially asymmetric having an almond-like shape as shown in Fig. 1.10. This initial spatial anisotropy gives rise to an azimuthal anisotropic pattern in the momentum distribution of final state particles due to subsequent interaction among the constituents.

The azimuthal distribution of the final state particle can be represented in terms of Fourier expansion with respect to the reaction plane. The reaction plane is the plane containing the centers of the colliding nuclei and the beam axis.

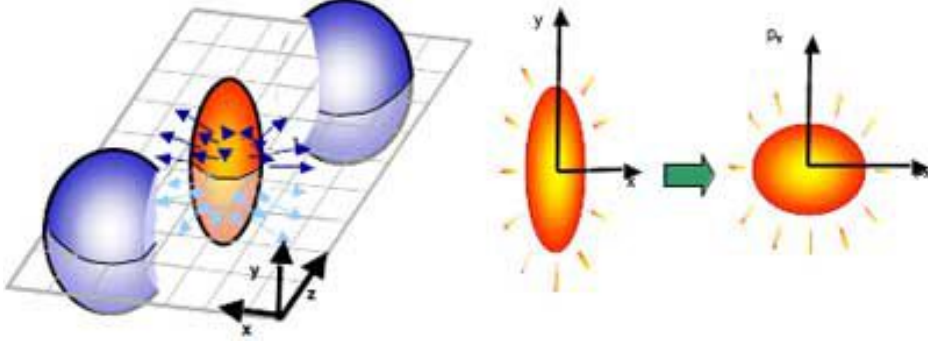


Figure 1.10: Schematic diagram for the initial-state anisotropy in the collision zone converting into the final-state elliptic flow measured as anisotropy in particle momentum. This figure has been taken from reference [26].

$$\frac{dN}{d\phi} \propto 1 + 2v_1 \cos(\phi - \psi) + 2v_2 \cos(2(\phi - \psi)) + \dots \quad (1.4)$$

where  $v_n$  is the  $n$ -th harmonic coefficient,  $\phi$  and  $\psi$  are the azimuthal and reaction plane angle respectively. The reaction plane angle is defined by the angle between the reaction plane and  $x$ -axis. The coefficient  $v_1$  is known as directed flow,  $v_2$  is called elliptic flow. In general  $v_2$  is larger than other coefficients. Figure 1.11 shows the elliptic flow for identified particles at  $\sqrt{s_{NN}} = 200$  GeV  $Au + Au$  collisions at RHIC. Up to  $p_T = 1.6$  GeV, heavier particles have a smaller  $v_2$ . At intermediate  $p_T$ , a clear difference is observed in  $v_2$  for identified baryons or mesons. This can be explained by assuming hadronization via quark coalescence or recombination [27, 28]. In the intermediate  $p_T$  region,  $v_2$  values can be scaled by the number of constituent quarks ( $n_q$ ) of the hadrons (i.e.,  $n_q = 3$  for baryons and  $n_q = 2$  for mesons). This is called the Number of Constituent Quark (NCQ) scaling [29]. This scaling suggests that the quark degrees of freedom are prevalent in the system produced in heavy-ion collisions.

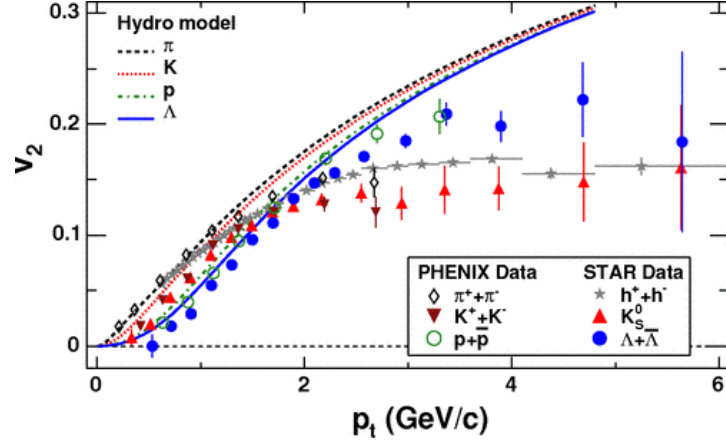


Figure 1.11: Measurement of  $v_2$  for identified particles as a function of  $p_T$  at RHIC. This figure has been taken from reference [30].

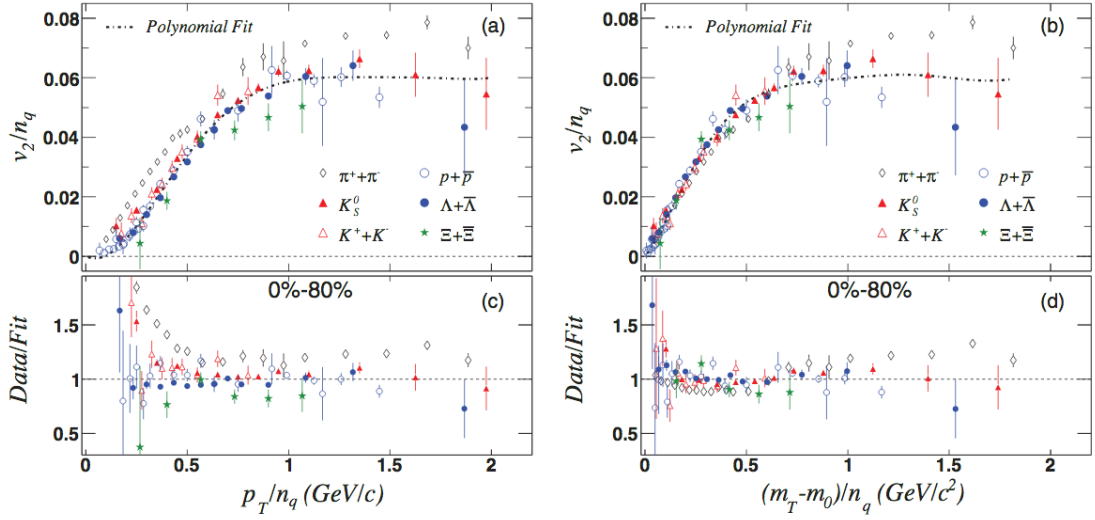


Figure 1.12: Elliptic flow of hadrons scaled by the constituent quarks number as a function of  $p_T/n_q$  and  $(m_T - m_0)/n_q$ . This figure has been taken from reference [31].

## 1.4 Signals for QCD phase transition

One of the proposed methods to study the nature of the phase transition is through the study of the fluctuations of thermodynamic quantities [32, 33]. Fluctuations of thermodynamic quantities provide important information about physical systems. In particular, the study of fluctuation and correlation provide essential information about the effective degrees of freedom of the system. Fluctuations can be grouped in several classes; First, at a fundamental level, there are quantum fluctuations. It happens if the particular observable does not commute with the Hamiltonian of the system. In the heavy-ion collisions, those fluctuations are not much significant for physics. Second, dynamical fluctuations and correlations, which play a significant role in the characterisation of the bulk properties of the system.

In high-energy heavy-ion collisions experiments, like the STAR experiment at RHIC, a large number of particles is produced in each event which makes the event-by-event fluctuation studies possible with accuracy. In heavy-ion collisions event-by-event fluctuations include studies of mean transverse momentum fluctuations, particle ratio fluctuations, multiplicity fluctuations, conserved charge fluctuations and correlations, etc. Event-by-event fluctuations of the mean transverse momentum ( $\langle P_T \rangle$ ) of final-state charge particles are sensitive to the temperature fluctuations [34] and might provide a measure of the heat capacity ( $c_v$ ) of the system [35, 36]. Near the critical point, the  $c_v$  can be expressed in terms of a power law,  $c_v \propto |T - T_c|^{-\alpha}$ , where  $T_c$  and  $\alpha$  are the critical temperature and critical exponent respectively. Thus the transverse momentum or temperature fluctuations may provide a probe of the critical point of the QCD phase diagram [37]. Event-by-event particle ratio fluctuations, such as proton-to-pion ( $p/\pi$ ), kaon-to-pion ( $K/\pi$ ) and proton-to-kaon ( $p/K$ ) are connected to the baryon number fluctuations, strangeness number fluctuations and baryon-strange correlation respectively.

### 1.4.1 Fluctuations in a thermal system

The system created in the high-energy heavy-ion collisions can be approximately considered to be a close to thermal equilibrium [38, 39]. In that context, one can consider the created thermal system within the grand-canonical ensemble. This is because, for heavy-ion collision experiment, typically particles at mid-rapidity (or, sometimes pseudo-rapidity) are considered for the analysis. We will discuss this point later on chapter 3.

In the grand-canonical ensemble, a system in thermal equilibrium is characterized by the partition function [40],

$$Z = \text{Tr} \left[ \exp \left( -\beta \left( H - \sum_i \mu_i Q_i \right) \right) \right], \quad (1.5)$$

where  $H$  is the Hamiltonian of the system,  $\beta$  represents the inverse temperature ( $1/T$ ) of the system,  $Q_i$  and  $\mu_i$  represent the  $i$ th conserved charge and corresponding chemical potential, respectively. In the three flavored QCD case,  $Q_i$  represents, the conserved charges – electric charge number, baryon number and strangeness number or equivalently, three quark flavors – up, down and strange. The free energy ( $F$ ) can be calculated by taking the logarithmic of the partition function,

$$F = k_B T \log Z, \quad (1.6)$$

where  $k_B$  is the Boltzmann constant. For a random variable  $X$ , fluctuations can be characterized by [40],

$$\langle \delta X^2 \rangle = \langle X^2 \rangle - \langle X \rangle^2, \quad (1.7)$$

where  $\langle \dots \rangle$  represents an average over events. In grand-canonical ensemble, fluctuations of macroscopic quantities can provide information about different response functions of the system. Such as energy fluctuation is related to specific heat ( $C_V$ ) of the system,

$$\begin{aligned} \langle \delta E^2 \rangle &= \frac{\partial^2}{\partial \beta^2} (\log Z) = -\frac{\partial \langle E \rangle}{\partial \beta} \\ &= -\left( \frac{\partial \langle E \rangle}{\partial T} \right) \left( \frac{\partial T}{\partial \beta} \right) = k_B T^2 C_V. \end{aligned} \quad (1.8)$$

The magnitude of fluctuations of the number of particles ( $N$ ) is related to the isothermal compressibility ( $k_T$ ),

$$\langle \delta N^2 \rangle = k_B T \frac{\partial \langle N \rangle}{\partial \mu} = \frac{\langle N \rangle^2 k_B T}{V} k_T. \quad (1.9)$$

Similarly, conserved charge susceptibilities are related to cumulants of conserved charge fluctuations and can be expressed by taking derivative of the partition function with respect to corresponding chemical potential,

$$\langle \delta Q_i^2 \rangle = -\frac{1}{V} \frac{\partial^2 F}{\partial^2 \mu_i} = VT \chi_{Q_i}^2. \quad (1.10)$$

One can define different combinations and higher order susceptibilities, by differentiating multiple times with respect to the corresponding chemical potentials,

$$\chi^{n_i, n_j, n_k} = \frac{1}{VT} \frac{\partial^{n_i}}{\partial(\mu_i/T)^{n_i}} \frac{\partial^{n_j}}{\partial(\mu_j/T)^{n_j}} \frac{\partial^{n_k}}{\partial(\mu_k/T)^{n_k}} \log Z. \quad (1.11)$$

### 1.4.2 Event-by-event fluctuations and correlations of conserved charges

As discussed in the previous section, fluctuations of conserved charges are related to thermodynamic susceptibilities. However, if one look at the entire system, none of the conserved charges will fluctuate event-by-event. Therefore, by analyzing a sufficiently small part of the entire system, the study of event-by-event fluctuation may become meaningful. The smaller sub-system then exchange both energy and conserved quanta, similar to grand canonical assumptions.

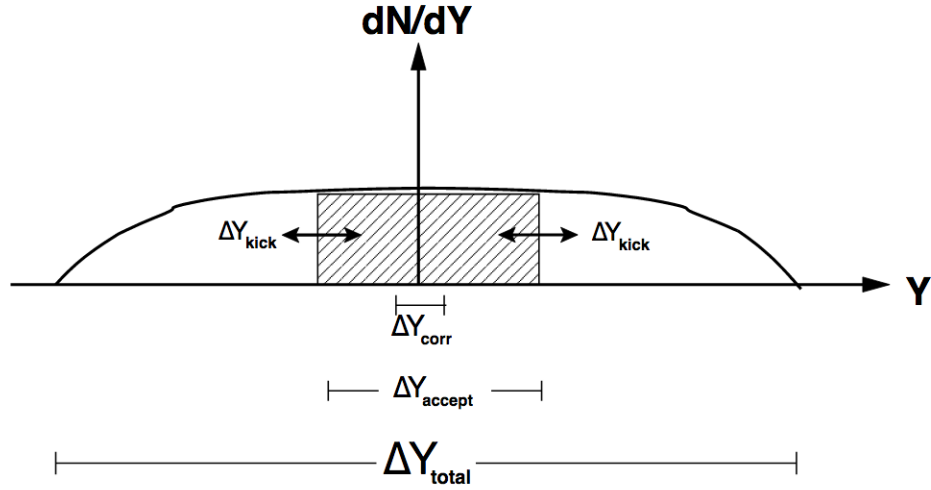


Figure 1.13: Sketch of the various rapidity scales relevant to conserved charge fluctuation in Heavy-ion collisions. The figure is taken from [41].

Figure 1.13 illustrates the various relevant rapidity scale in a heavy-ion collision experiment.  $\Delta Y_{\text{total}}$  corresponds to full phase-space interval of all particles.  $\Delta Y_{\text{accept}}$  is a small sub-system within  $\Delta Y_{\text{total}}$  corresponding the intervals of accepted rapidity window.  $\Delta Y_{\text{corr}}$  is the change in

correlation length, whereas  $\Delta Y_{\text{kick}}$  is the typical shift in rapidity received during after hadronization. The properties of the QGP system can be extracted by studying conserved charge fluctuations if the following criteria are fulfilled.

$$\Delta Y_{\text{accept}} \gg \Delta Y_{\text{corr}} \tag{1.12}$$

$$\Delta Y_{\text{total}} \gg \Delta Y_{\text{accept}} \gg \Delta Y_{\text{kick}} \tag{1.13}$$

The first equation is the necessary condition to extract the relevant physics, The second equation ensures that the total charge conservation does not affect the signal and also the signal survives hadronization and hadronic phase. The charge kick,  $Y_{\text{kick}}$  due to re-scattering in the hadronic phase can be estimated in the order of  $\Delta Y_{\text{kick}} \simeq 1.5$  using transport model [42]. These suggest that charge fluctuations in a sufficiently high collision energies give the more clear signal from QGP phase than lower energies. Whereas, at low collision energies the total rapidity acceptance ( $\Delta Y_{\text{total}}$ ) is comparable to the typical rapidity shifts ( $\Delta Y_{\text{kick}}$ ), which makes the interpretation of conserved charge fluctuations and correlations rather difficult.

### 1.4.3 QCD phase transition and critical point study at RHIC

Higher order cumulants ( $c_n^\alpha[\delta N]$ ) of the net-baryon, net-charge, and net-strangeness multiplicity distributions are related to the higher-order thermodynamic susceptibilities ( $\chi_n^\alpha = 1/VT^3 c_3^\alpha[\delta N]$ ) of the respective conserved charges ( $\alpha$ ) [43]. QCD based calculations show that the correlation length ( $\xi$ ) is sensitive to these higher-order cumulants of conserved charges [44, 45]. For instance the third order cumulant  $c_3$  is proportional to  $\xi^{4.5}$  and fourth order cumulants scales as  $c_4 \sim \xi^7$ . In the vicinity of the critical point, the correlation length is expected to diverge. The QCD based Ising model calculation [46] exhibits the negative kurtosis around the phase transition line manifests the

presence of critical point approaching from the crossover line. Several other theoretical calculations which include interactions of quarks with effective gluon fields such as the Polyakov loop extended Nambu-Jona-Lasinio (PNJL) [47] and the quarkmeson (PQM) [48] models also show that ratios of  $\chi^4/\chi^2$  exhibit large peaks at the critical temperature in the chiral limit [49]. Motivated by this, in the past few years, STAR and PHENIX experiment at RHIC has been measured higher order diagonal cumulant ratios ( $\frac{c_4}{c_2} = \kappa\sigma^2$ ) of the net-proton (as an experimental proxy of net-baryon) [50], net-charge [51, 52] and net-kaon (the experimental proxy for the net-strangeness) [53] multiplicity distributions.

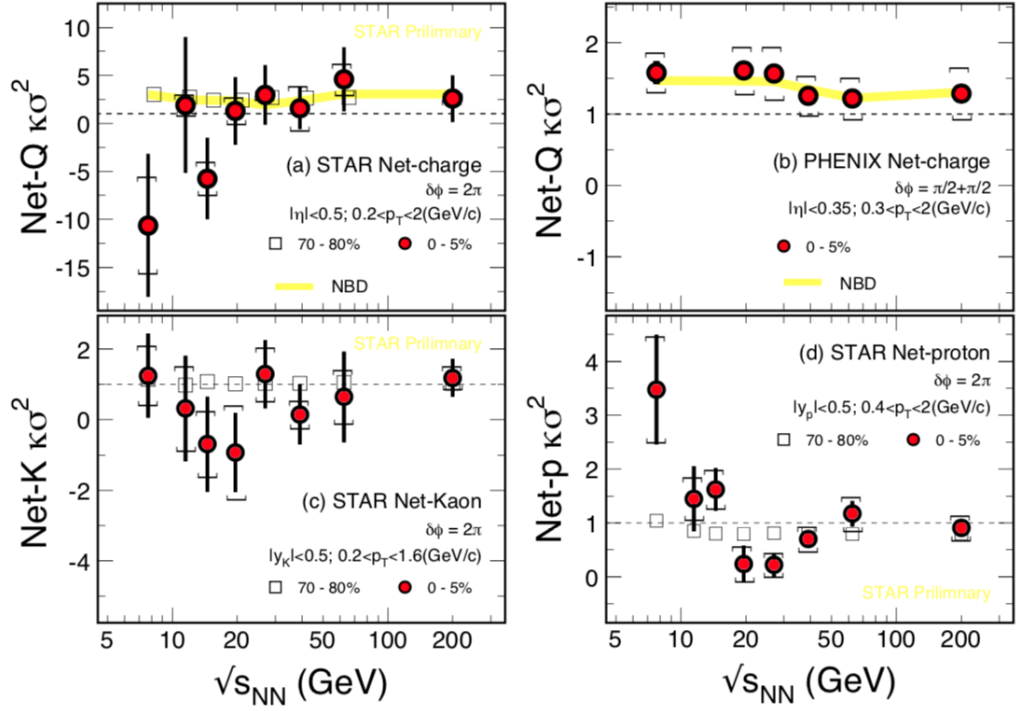


Figure 1.14: The collision energy dependence  $\kappa\sigma^2$  of net-charge (top left), net-proton (bottom right) and net-kaon (bottom left) multiplicity distribution in  $Au + Au$  collisions are measured in STAR experiment. The  $\kappa\sigma^2$  of net-charge from PHENIX experiment is presented in the top right panel. The figure is taken from [54].

Figure 1.14 shows the beam energy dependence  $\kappa\sigma^2$  ( $= \frac{c_4[\delta N]}{c_2[\delta N]}$ ) of net-charge, net-proton and net-kaon multiplicity distributions in  $Au + Au$  collisions for two different centralities (0-5% and

70-80%) measured by the STAR and PHENIX experiments. For net-charge and net-kaon results, no non-monotonic energy variation have been observed within the statistical uncertainties. The dashed lines represent Poisson expectation. For the distribution of uncorrelated variables, which follows Poisson statistics, the value of  $\kappa\sigma^2$  is unity [54]. Non-monotonic energy dependence is observed in  $\kappa\sigma^2$  of net-proton with minima near 19.6 GeV. This non-monotonic energy dependence cannot be described by any model without critical point physics [55, 56]. However, there are several constraints and/or effects in the experimental measurement which need to be properly understood to interpret the result and compare the measured data with theoretical calculations. In chapter 3, we will discuss some of these constraints and effects on cumulant analysis.

Similar to the diagonal cumulants, one can study  $(m + n)$ -th order off-diagonal cumulants ( $c_{\alpha,\beta}^{m,n}$ ) of net-charge, net-proton and net-kaon multiplicity distribution in heavy-ion experiment. These off-diagonal cumulants are related to mixed susceptibilities ( $\chi_{\alpha,\beta}^{m,n}$ ) that represent the correlations between different flavours in QCD [57, 58]. The importance of studying these off-diagonal cumulants was first highlighted in the context of baryon-strange correlations in reference [59]. Off-diagonal cumulants of conserved charges are expected to feature a rapid change in the confinement to the deconfinement phase transition [59, 58, 60, 61]. The measurement of off-diagonal cumulants has specific advantages over diagonal cumulants. For the same order, the off-diagonal cumulants are more sensitive than the diagonal cumulants to distinguishing between the partonic and hadronic phases [62, 63]. On the other hand, in Heavy-ion collision experiments we can only identify the charge particles on an event-by-event basis. A measurement of the total number of produced baryons is challenged by the lack of neutral baryons (e.g., neutrons). The same is true for the strange particles. Also, experimentally the event-by-event reconstruction of higher mass baryon and strange particles has its limitations in terms of low purity and efficiency. One, therefore, uses proxies the number of net-protons (p) and net-kaons (k) as proxies for the measurements of

$c_B^n$  and  $c_S^n$ . Measurement of off-diagonal cumulants such as  $c_{Q,B}^{m,n}$  and  $c_{Q,S}^{m,n}$  are less affected by these experimental limitations because neutral-baryons or neutral-strange particles do not contribute to these off-diagonal cumulants. They can be approximated  $c_{Q,B}^{m,n} \approx c_{Q,p}^{m,n}$  and  $c_{Q,S}^{m,n} \approx c_{Q,k}^{m,n}$  [64]. However,  $c_{B,S}^{m,n}$  cannot be simply approximated by  $c_{p,k}^{m,n}$  without measuring strange-baryons, although one expects a reasonable connection between the two quantities [64, 65]. In the following chapters, I discuss the measurement of these off-diagonal cumulants at eight beam energies at RHIC and compare the experimental results with different model predictions.

## 1.5 Organization of the thesis

The thesis is organized as follows. In chapter 2, I discuss the properties of the statistical cumulants and their connection to the thermodynamic susceptibilities. In chapter 3, a detailed simulation study is presented for different conserved charge (including baryon number, strangeness number, and electric charge) susceptibilities and cumulants using the Hadron Resonance Gas (HRG) and the Ultrarelativistic Quantum Molecular dynamics (UrQMD) models. In chapter 4, the experimental facilities at Relativistic Heavy-Ion Collider (RHIC) are briefly described. In the present work, particle identification is done based on signals from the Time Projection Chamber (TPC) and Time of Flight (TOF) detectors. The STAR data analysis details is presented in chapter 5. In this chapter, data sets, events and track selection, particle identification, and centrality selection procedures are discussed. Additionally, centrality bin width correction, efficiency estimation and correction, both systematic and statistical uncertainty estimation are also discussed in details in chapter 5. In chapter 6, the centrality and  $\eta$ -acceptance dependence of all  $2^{nd}$ -order diagonal and off-diagonal cumulants are presented collisions measured at  $\sqrt{s_{NN}} = 7.7, 11.5, 14.5, 19.6, 27, 39, 62.4$  and 200 GeV. A first estimate of the isothermal compressibility ( $k_T$ ) at the chemical freeze-out from multiplicity fluctuation is done in chapter 7. In chapter 8, the summary and outlook of the

thesis have been discussed.

## Chapter 2

# Cumulants of net-particle multiplicity distributions

In statistics, cumulants are quantitative measure of the shape of a probability distribution. For example, square root of  $2^{nd}$ -order diagonal cumulant ( $\sigma = \sqrt{c_2}$ ) measures the width of a distribution, and second-order off-diagonal cumulant ( $\sigma^{1,1} = c_{1,1}$ ) is measures of correlation between two different random variables. The degree of symmetry and tailedness of a distribution is quantified by cumulants ratios, like, Skewness ( $c_3/c_2^{3/2}$ ) and Kurtosis ( $c_4/c_2^2$ ), respectively. For Gaussian variables, cumulants of order greater than two are zero. So, higher-order cumulants are often used in testing for gaussianity. In this chapter, we will discuss the properties of the cumulants and their connection to the thermodynamic susceptibilities.

### 2.1 Cumulant-generating function

In this thesis, we are interested in both diagonal as well as off-diagonal cumulants of net-particles (like net-charge, net-proton, etc.) multiplicity distribution. Diagonal cumulants can be constructed

from single-variate cumulant generating function whereas the off-diagonal cumulants are defined from bivariate cumulant generating functions. In the next two sections, we will discuss the single and bivariate cumulant generating function. However, in heavy-ion collision, these net-particles are counted by the number of positive particles minus the number of negative particles with different efficiencies. These positive/negative particle efficiencies also depend on different phase-space bins. So, for efficiency correction, this single and bivariate cumulants needs to be express in terms of multivariate factorial moments. Corrections for such losses are discussed in chapter 5 in details.

### 2.1.1 Single variable cumulant-generating function

The cumulants ( $c_n$ ) of a random variable  $X$  are defined based on derivative of the cumulant-generating function (CGF) ( $G(t)$ ) [66, 67]. The CGF is defined as,

$$G_X(t) = \ln[M_X(t)], \quad (2.1)$$

where,  $M_X(t)$  is the moment generating function (MGF) of the random variable  $X$ , defined as

$$M_X(t) = E(e^{tX}) = E\left(\sum_{n=0}^{\infty} \frac{t^n X^n}{n!}\right). \quad (2.2)$$

The moments  $\mu'_n = E(X^n) = \langle X^n \rangle$  can be extracted by taking the derivative of MGF evaluated at  $t = 0$ ,

$$\mu'_n = \left. \frac{\partial^n \left( E \sum_{n=0}^{\infty} \frac{t^n X^n}{n!} \right)}{\partial t^n} \right|_{t=0}, \quad (2.3)$$

where  $E$  denotes the ensemble average of the random variable  $X$ . The cumulant generating function can be expressed in terms of the moments as:

$$G_X(t) = \ln M_X(t) = \sum_{m=1}^{\infty} \frac{(-1)^{(m+1)}}{m} (M_X(t) - 1)^m. \quad (2.4)$$

Finally, the  $n$ -th order cumulant can be represented in terms of moments by taking derivative of  $G_X(t)$  (at  $t = 0$ ) [68],

$$c_1 = \mu'_1 \quad (2.5)$$

$$c_2 = \mu'_2 - \mu_1'^2 \quad (2.6)$$

$$c_3 = \mu'_3 - 3\mu'_2\mu'_1 + 2\mu_1'^3 \quad (2.7)$$

$\vdots$

$$c_n = \mu'_n - \sum_{m=1}^{n-1} \binom{n-1}{m-1} c_m \mu_{n-m}' \quad [68, 66] \quad (2.8)$$

The diagonal cumulants describe the shape of a distribution. The second order cumulant ( $c_2 = \sigma^2$ ) called variance is used to describe the width of the distribution. The normalized third and fourth order central moment are called Skewness ( $S = c_3/c_2^{3/2}$ ), and Kurtosis ( $\kappa = c_4/c_2^2$ ), respectively. They describe the asymmetry and peakiness of the distribution, respectively, as shown in Fig. 2.1.

Skewness and Kurtosis both vanishes for Gaussian distributions. Hence, the measurements of skewness and kurtosis are ideal probes of non-gaussian fluctuations.

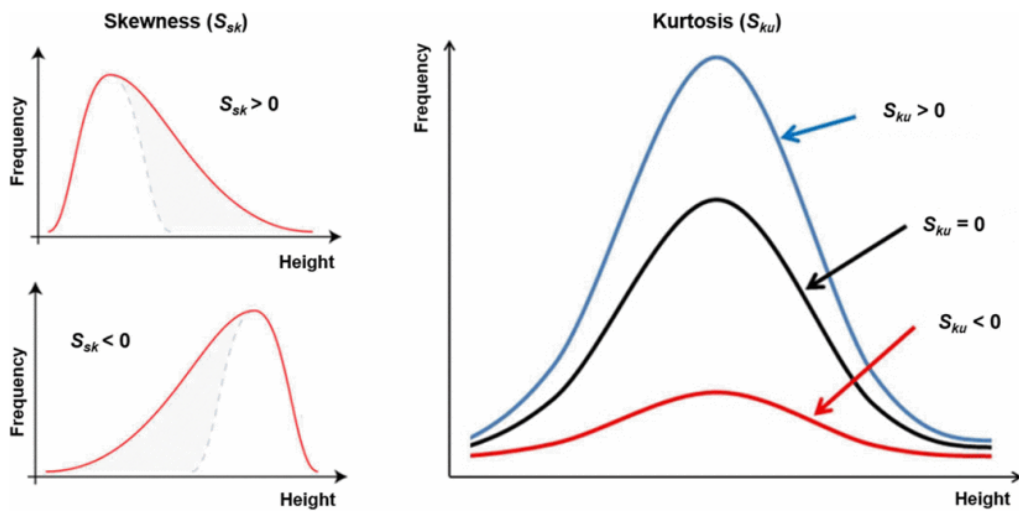


Figure 2.1: Visual example of distribution with positive/negative skewness (left panel) and positive/negative kurtosis (right panel). Reproduced from [69].

### 2.1.2 Bivariate cumulant generating function

The joint-cumulant generating function of the multivariate random variables  $X_1, X_2, \dots, X_n$  is defined as,

$$G(t_1, t_2, \dots, t_n) = \ln E(e^{t_1 X_1 + t_2 X_2 + \dots + t_n X_n}). \quad (2.9)$$

The joint cumulants are expressed as,

$$c(X_1, X_2, \dots, X_n) = \sum_{\pi} (|\pi| - 1)! (-1)^{|\pi|-1} \prod_{B \in \pi} E\left(\prod_{i \in \pi} X_i\right), \quad (2.10)$$

where  $\pi$  runs through the list of all partitions of  $1, 2, \dots, n$  and  $B$  runs through the list of all blocks of the partition  $\pi$ , and  $|\pi|$  is the number of parts in the partition [70]. From Equation 2.10 the bivariate ( $\pi = 2$ ) cumulants ( $c_{m,n}$ ) can be expressed in terms of mixed moments ( $\mu'_{n_1, n_2}$ ) as follows:

$$c_{1,1} = \mu'_{1,1} - \mu'_{1,0} \mu'_{0,1} \quad (2.11)$$

$$c_{2,1} = \mu'_{2,1} - 2\mu'_{1,0} \mu'_{1,1} - \mu'_{2,0} \mu'_{0,1} + 2\mu'^2_{1,0} \mu'_{0,1} \quad (2.12)$$

$$c_{3,1} = \mu'_{3,1} - 6\mu'_{0,1} \mu'^3_{1,0} + 6\mu'_{1,1} \mu'^2_{1,0} + 6\mu'_{0,1} \mu'_{2,0} \mu'_{1,0} - 3\mu'_{2,1} \mu'_{1,0} - 3\mu'_{1,1} \mu'_{2,0} - \mu'_{0,1} \mu'_{3,0}. \quad (2.13)$$

The  $2^{nd}$ -order mixed cumulant ( $c_{1,1}$ ) is called co-variance and used to characterise the correlation between two random variables. Figure 2.2 presents a visual example of  $2^{nd}$  order off-diagonal cumulants, where the left panel corresponds to  $c_{1,1} > 0$ , the middle panel corresponds to  $c_{1,1} < 0$ ,

whereas the third, right panel corresponds to  $c_{1,1} \approx 0$ .

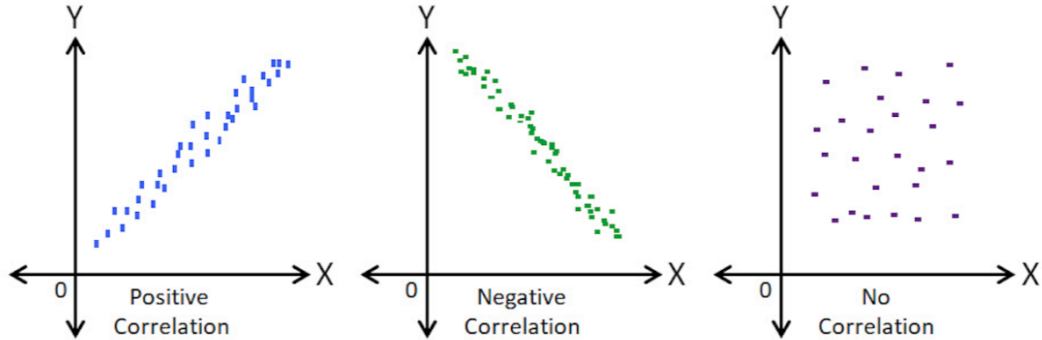


Figure 2.2: Graphical example of positive/negative and null  $2^{nd}$ -order off-diagonal cumulants.

## 2.2 Properties of the cumulants

The primary properties of moments and cumulants are discussed below.

- Additivity:

If  $X_1, X_2, \dots, X_n$  are independent random variables, then:

$$c_n(X_1 + X_2 + \dots + X_n) = \sum_{r=1}^n c_n(X_r), \quad (2.14)$$

- Shifting invariance:

If  $X$  is a random variable, Then for any constant  $a$ ,

$$c_n(X + a) = c_n(X), n > 1 \quad (2.15)$$

For,  $n = 1$ ,  $c_1(X + a) = c_1(X) + a$ ,

- Homogeneity:

For a random variable  $X$  and a constant  $a$ ,

$$c_n(aX) = a^n c_n(X). \quad (2.16)$$

### 2.3 Cumulants in Heavy-Ion Collision

Heavy-ion collision experiments measure particle multiplicities on an event-by-event basis.  $N_\alpha, N_\beta$  represents the number of  $\alpha, \beta$  (can be net- $p$ ,  $K$ , or  $Q$ ) species in an event. Then,  $2^{nd}$ -order diagonal and off-diagonal cumulants can be expressed as,

$$c_\alpha^2 = \sigma_\alpha^2 = \langle (\delta N_\alpha - \langle \delta N_\alpha \rangle)^2 \rangle, \quad (2.17)$$

and

$$c_{\alpha,\beta}^{1,1} = \sigma_{\alpha,\beta}^{1,1} = \langle (\delta N_\alpha - \langle \delta N_\alpha \rangle)(\delta N_\beta - \langle \delta N_\beta \rangle) \rangle. \quad (2.18)$$

Here,  $\langle \dots \rangle$  represents an average over the event ensemble. With the above definition, various  $2^{nd}$ -order diagonal and off-diagonal cumulants, as well as cumulant ratios of net-charge, net-proton and net-kaon, can be measured in heavy-ion collisions. Off-diagonal cumulants of conserved charges, such as net-charge, net-proton and net-strangeness number are predicted to provide useful insight into the QCD phase diagram [62] because they are directly linked to thermodynamic susceptibilities. These thermodynamic susceptibilities were computed in Lattice QCD [58, 60, 44, 45], the Hadron Resonance Gas model, as well as with transport event generator (like UrQMD). Some of these calculations will be discussed in chapter 3.

### 2.3.1 Connection to thermodynamic susceptibilities

Within the Grand Canonical Ensemble (GCE), the dimensionless pressure for a system in thermal equilibrium can be defined as the logarithm of the partition function [71]:

$$\frac{P}{T^4} = \frac{1}{VT^3} \ln[Z(V, T, \mu_X)], \quad (2.19)$$

where  $V$  and  $T$  are the volume and temperature of the system, respectively.  $\mu_X$  represents conserved charge chemical potentials, like the baryon chemical potentials ( $\mu_B$ ), the charge chemical potential ( $\mu_Q$ ) and the strangeness chemical potential ( $\mu_S$ ).

The  $n(= i + j + k)$ -th order conserved charge susceptibilities of net-charge ( $Q$ ), net-proton ( $B$ ) and net-strangeness ( $S$ ) are defined as,

$$\chi_{BQS}^{ijk} = \frac{\partial^{i+j+k}(P/T^4)}{\partial^i(\mu_B/T) \partial^j(\mu_Q/T) \partial^k(\mu_S/T)}. \quad (2.20)$$

Different order diagonal (any of two among  $i, j, k = 0$ ) and off-diagonal ( $i$  or  $j$  or  $k = 0$ ) susceptibilities are connected to the cumulants of corresponding conserved charge distribution ( $Q$ ,  $B$ , and  $S$ ) by,

$$c_{B,Q,S}^{i,j,k} = VT^3 \chi_{B,Q,S}^{i,j,k}. \quad (2.21)$$

Let us now discuss the off-diagonal cumulants. In reference [59], off-diagonal susceptibilities were first discussed in the context of baryon-strange and charge-strange correlations. Normalized baryon-strange correlations can be defined as [59, 58],

$$C_{BS} = -3 \frac{\chi_{BS}}{\chi_S} = -3 \frac{c_{B,S}^{1,1}}{c_S^2} = -3 \frac{\langle \delta B \delta S \rangle}{\langle \delta S^2 \rangle}. \quad (2.22)$$

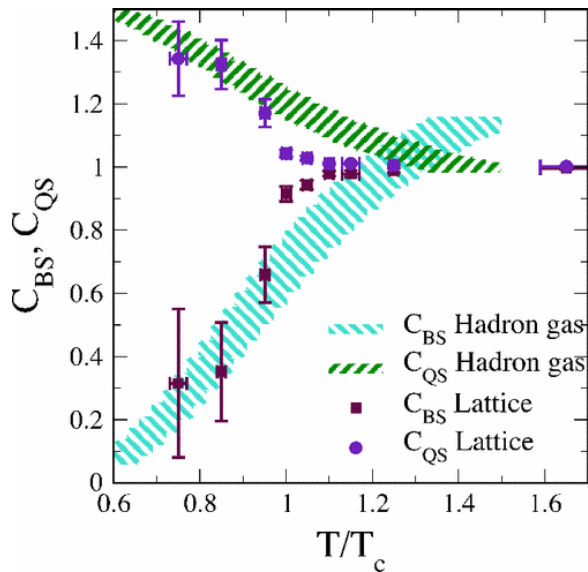


Figure 2.3: The correlation coefficients  $C_{BS}$  and  $C_{QS}$  in a hadron gas at  $\mu_B = \mu_Q = \mu_S = 0$  and from lattice calculation at  $\mu = 0$  (Ref. [57]). The value of  $T_c$  is assumed to lie in the range  $T_c = 170 \pm 10$ . The figure is from [58].

In a system of uncorrelated quark flavors, the conserved charges are carried by quark flavors: upness ( $\Delta u = u - \bar{u}$ ), downness ( $\Delta d = d - \bar{d}$ ), and strange-quarkness ( $\Delta s = s - \bar{s}$ ). The normalized correlations can be expressed as,

$$\begin{aligned}
 C_{BS} &= -3 \frac{\langle \delta B \delta S \rangle}{\langle \delta S^2 \rangle} = -3 \frac{\langle (\frac{1}{3}(\Delta u + \Delta d + \Delta s))(-\Delta s) \rangle}{\langle \Delta s^2 \rangle} \\
 &= 1 + \frac{\langle \Delta u \Delta s \rangle + \langle \Delta d \Delta s \rangle}{\langle \Delta s^2 \rangle}.
 \end{aligned} \tag{2.23}$$

For a system of uncorrelated quarks,  $\langle \Delta d \Delta s \rangle = \langle \Delta u \Delta s \rangle = 0$ . Hence, Equation 2.23 become,

$$C_{BS} = 1. \tag{2.24}$$

Similar to Equation 2.23, the correlation coefficient  $C_{QS}$  for uncorrelated quarks flavor can be

expressed as [41],

$$\begin{aligned}
 C_{QS} = 3 \frac{\langle \delta Q \delta S \rangle}{\langle \delta S^2 \rangle} &= 3 \frac{\langle (\frac{2}{3} \Delta u - \frac{1}{3} \Delta d - \frac{1}{3} \Delta s) (-\Delta s) \rangle}{\langle \Delta s^2 \rangle} \\
 &= 1.
 \end{aligned}
 \tag{2.25}$$

On the other hand, in a gas of uncorrected hadrons,  $C_{BS}$  can be approximated from the mean hadron yields [41],

$$C_{BS} \approx 3 \frac{\langle \Lambda \rangle + \langle \bar{\Lambda} \rangle + \dots + 3 \langle \Omega^- \rangle + 3 \langle \bar{\Omega}^+ \rangle}{\langle K \rangle + \langle K^0 \rangle + \dots + 9 \langle \Omega^- \rangle + 9 \langle \bar{\Omega}^+ \rangle},
 \tag{2.26}$$

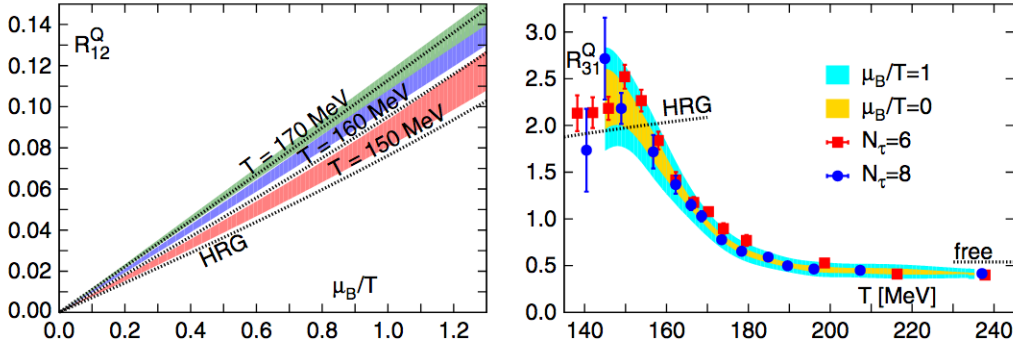


Figure 2.4

where the numerator receives contributions from strange-baryons (and anti-strange-baryons), while all strange (and anti-strange) hadrons contribute to the denominator. In addition, off-diagonal cumulants ratios ( $R_{12}^Q, R_{31}^Q$ ) show a significant strong sensitivity to  $\mu_B$  and  $T$ . Therefore, measurements of off-diagonal cumulants will help extraction of freeze-out parameters [72, 73, 74].

In the following chapters, we discuss measurement of these off-diagonal cumulants in the RHIC beam energy scan program (BES-I). We also compare the experimental results with different model

predictions.

## 2.4 Beam Energy Scan Program at RHIC

The first decade of Relativistic Heavy-Ion Collider operation was devoted to studying the quark-gluon plasma state of matter formed in the early stages of Au+Au collision at  $\sqrt{s_{NN}} = 200$  GeV. Preliminary results revealed that this new kind of matter has unique properties which indicate that a QGP phase is created in high-energy heavy-ion collisions. However, many questions remain unaddressed. In particular, the nature of the transformation from hadronic degrees of freedom to the QGP degrees of freedom, and back to the state of hadron gas, is not clear. Although the exact boundary of first-order phase transition, as well as the position of the QCD critical point, is not known, there are lattice calculations that suggest the most probable location of critical point would be somewhere between  $\mu_B = 150$ -500 MeV [75].

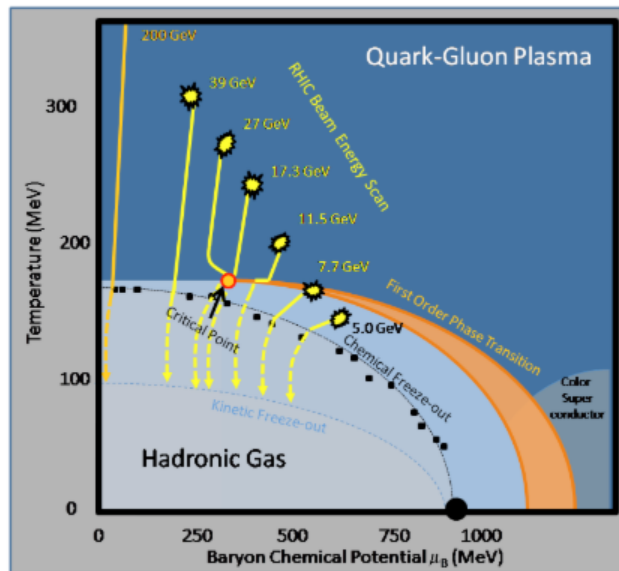


Figure 2.5: A schematic of the QCD phase diagram.  $T_{ch}$ , and  $\mu_B$  based on the statistical model fit to the measured particle ratios. The yellow curves show the estimated trajectories of the possible collision energies at RHIC. The figure is taken from [76].

The system produced in  $Au + Au$  collisions at lower energies can be able to reach the region of interest, therefore allow to investigation the first-order phase transition, and possibly of the Critical Point (CP).  $Au + Au$  data are taken in the year 2010 (at  $\sqrt{s_{NN}} = 7.7, 11.5, 39, 62.4$  GeV), 2011 (at  $\sqrt{s_{NN}} = 19.6, 27$  GeV), and 2014 (at  $\sqrt{s_{NN}} = 14.5$  GeV) in the first phase of the Beam Energy Scan (BES-I) program at RHIC. Figure 2.5 shows the reach of BES-I data in the  $T-\mu_B$  plane. This data along with the earlier collected data at higher energies (62, 130 and 200 GeV), covers a wider range of phase diagram,  $\mu_B$  interval from 20 to 420 MeV [77]. This also implies that The Large Hadron Collider at CERN will cover small  $\mu_B$ , where the cross-over is expected and future FAIR experiment at Darmstadt, Germany will cover much higher  $\mu_B$  region. Figure 2.6 shows the relation between freeze-out temperature (top panel) and chemical potential with respect to collision energies [77].

The primary goals of this program are:

- to scan the phase diagram with variable collision energy (for different  $\mu_B$  and  $T$ ),
- to find the evidence of critical point and first-order phase transition in the QCD phase diagram, and
- to study the properties of QGP as a function of  $\mu_B$ .

Table 2.1 briefly describes the details of BES-I program and the plan for upcoming BES-II program. In the thesis work, data analysis have been performed for eight collision energies,  $\sqrt{s_{NN}} = 7.7, 11.5, 14.5, 19.6, 27, 39, 62.4, 200$  GeV in  $Au + Au$  collisions, which are recorded by the STAR experiment during the first phase of RHIC beam energy scan (BES-I) run.

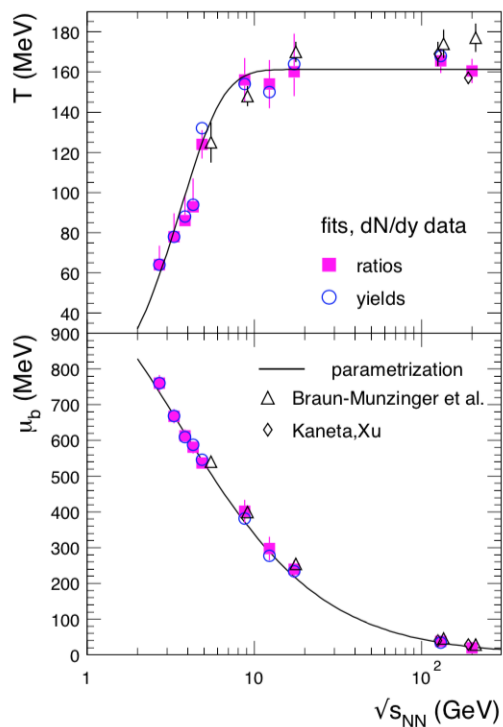


Figure 2.6: Energy dependence of the chemical freeze-out parameters  $T$  and  $\mu_B$ . The figure is taken from reference [78].

$\sqrt{s_{NN}}$ (GeV)	Events ( $10^6$ )	BES-II/ BES-I	$\mu_B$ (MeV)	$T_{ch}$ (MeV)
200	350	2010	25	166
62.4	67	2010	73	165
54.4	1200	2017		
39	39	2010	112	164
27	70	2011	156	162
19.6	400/ 36	2019-20/ 2011	206	160
14.5	300/ 20	2019-20/ 2014	264	156
11.5	230/ 12	2019-20/ 2010	315	152
9.2	160/ 0.3	2019-20/ 2008	355	140
7.7	100/ 4	2019-20/ 2010	420	140

Table 2.1: RHIC operating modes for BES-I program and proposed data that will be obtained during BES-II.



## Chapter 3

# Estimation of susceptibilities of conserved charges from model calculations

In this chapter, I will discuss thermal model and transport model predictions of different  $2^{nd}$ -order diagonal and off-diagonal conserved charged susceptibilities. In the previous chapter, we have discussed that the baryon number, strangeness number, and electric charge susceptibilities are expected to be sensitive to the quantum chromodynamics phase transition. So the event-by-event fluctuations of net-baryon, net-strangeness and net-charge from their ensemble average within a fixed appropriate phase space are expected to provide information on the matter produced in heavy-ion collision experiment. This chapter provides a detailed comprehensive study of second-order susceptibility and cumulant matrix elements within a thermal model approach of the hadron resonance gas (HRG) model as well as with a hadronic transport model, the ultra-relativistic quantum molecular dynamics (UrQMD v3.3) [64]. There are several limitation and/or effects in experimental measurements which need to be properly understood to interpret the re-

sults and compare with theoretical calculations. In this chapter, we will also discuss effects of the detector acceptances as well as particle species dependence on the experimental measurements of the susceptibilities in heavy-ion collisions corresponding to  $\sqrt{s_{\text{NN}}} = 4 \text{ GeV}$  to  $200 \text{ GeV}$ .

Ideally, to observe grand canonical fluctuations of the conserved charges, the fraction  $\mathcal{R}$  of the conserved charge carried by the system relative to the total available charge should be much smaller than half. In a full overlap  $A + A$  collisions, the net-charge ( $\Delta N_Q$ ) equals to double of the atomic number, and net-baryon ( $\Delta N_B$ ) equals to twice the mass number of the nucleus and that are distributed within the momentum rapidity ( $y$ ) direction. Thus the final distributions of  $\Delta N_Q$  and  $\Delta N_B$  depend on the system phase-space acceptance, the colliding beam energies, and baryon stopping. In this chapter, first we briefly discuss the UrQMD and HRG model in section 3.1. In section 3.2, we will discuss the observables used for this model study. Collision energy dependence of these susceptibilities will be discussed in section 3.3. Particle species and acceptance dependence will be discussed in section 3.4 and section 3.5 respectively. This model study will give some guidance to STAR data analysis.

### 3.1 UrQMD and HRG Model

UrQMD is a microscopic transport model [79, 80], featuring hadron-hadron interactions and the space-time system evolution are studied based on the covariant propagation of all hadrons in combination with stochastic binary scatterings, color string formation, and resonance decay. This model has been quite successful and is widely applied towards heavy-ion phenomenology [79, 80]. UrQMD has also been used to compute several cumulants of particle distributions [81, 82, 83, 84, 85]. The acceptance window plays an important role in such studies. The rapidity distribution of  $\Delta N_B$  and  $\Delta N_Q$  is a consequence of the baryon stopping phenomenon which has a strong beam energy dependence. The mid-rapidity region for high  $\sqrt{s_{\text{NN}}}$  is almost free of net-baryon and net-

charge while, at lower  $\sqrt{s_{\text{NN}}}$ , almost all the net baryon and charge are deposited in the mid-rapidity region. Thus, this is expected to have a significant effect on the conserved charge cumulants. This collision energy dependence baryon stopping phenomenon is dynamically included in the UrQMD model. In this study, we have used nearly a million events per beam energy from  $\sqrt{s_{\text{NN}}} = 4.4$  to 200 GeV. In this work, we study different second-order susceptibilities using a thermal HRG model and compare those results with conserved charge cumulants from UrQMD model. The HRG results are expected to reflect the susceptibilities at chemical freezeout whereas the UrQMD results reveal the observables at the kinetic freezeout. The HRG results serve as a useful guide for a qualitative understanding of the experimental data. It is a framework of multiple species non-interacting ideal gas in complete chemical and thermal equilibrium. The Hadron Resonance Gas model uses masses of hadrons and resonances as listed in the Particle Data Book [86] and few thermodynamic parameters, such as temperature ( $T$ ), volume ( $V$ ) and three chemical potentials  $\mu_Q, \mu_B, \mu_S$ . The HRG model can successfully describe the mean hadron yield at freezeout [87]. In this work, we have used the same parametrization for the  $\sqrt{s_{\text{NN}}}$  dependence of  $T, \mu_B, \mu_Q$  and  $\mu_S$  as given in Reference [44]. The chemical freezeout volumes,  $V(\sqrt{s_{\text{NN}}})$  are taken from Reference [87]. These parameters are listed in table 3.1 and extracted by fits to experimental data.

Susceptibilities have been employed to study the freeze-out conditions of the fireball within the HRG model [72]. All the quantities of interest can be computed from the partition function  $Z(V, T, \mu_B, \mu_Q, \mu_S)$ ,

$\sqrt{s_{\text{NN}}}$ (GeV)	$10^4 V$ (MeV $^{-3}$ )	$T$ (MeV)	$\mu_B$ (MeV)	$\mu_Q$ (MeV)	$\mu_S$ (MeV)
6.27	1.4	130.8	482.4	12.7	106.5
7.62	1.3	139.2	424.6	11.7	96.1
7.7	1.3	139.6	421.6	11.6	95.5
8.76	1.1	144.2	385.7	10.9	88.8
11.5	1.5	151.6	316.0	9.5	75.0
17.3	2.0	158.6	228.6	7.4	56.5
39	1.7	164.2	112.3	4.1	29.4
62.4	1.8	165.3	72.3	2.8	19.4
130	2.1	165.8	35.8	1.4	9.8
200	2.5	165.9	23.5	1.0	6.4

Table 3.1: The chemical freezeout parameters extracted from mid-rapidity data at different  $\sqrt{s_{\text{NN}}}$  [87, 44].

$$\begin{aligned}
\ln Z &= \sum_i \ln Z_i \\
&= \sum_i \frac{aV g_i}{(2\pi)^3} d^3 p \ln(1 + a e^{-(p^2+m^2)+\mu_i}/T) \\
&= VT3 \sum_i \frac{g_i}{(2\pi)^2} \left(\frac{m_i}{T}\right)^2 \sum_{l=1}^{\infty} (-a)^{l+1} l^{-2} K_2(lm_i/T) \\
&\quad \exp[l(B_i\mu_B + Q_i\mu_Q + S_i\mu_S)/T],
\end{aligned} \tag{3.1}$$

where  $a = -1$  for mesons and 1 for baryons.  $B_i$ ,  $Q_i$ ,  $S_i$ ,  $g_i$ ,  $m_i$  and  $\mu_i (= B_i\mu_B + Q_i\mu_Q + S_i\mu_S)$  refers to the baryon number, electric charge number, strangeness number, degeneracy factor, mass, and hadron chemical potential respectively of the  $i^{\text{th}}$  hadron species,  $V$  is the system volume inside the fireball and  $K_2$  is the modified Bessel function of the second kind. In principle, all thermodynamic quantities can be computed from  $\ln Z$ .

## 3.2 Observables and methods

Conserved charge susceptibilities of the strongly interacting matter in thermal and chemical equilibrium are defined as partial derivatives of the pressure ( $P$ ) with respect to the chemical potentials within the grand canonical ensemble (GCE),

$$\chi_{BQS}^{ijk} = \frac{\partial^{i+j+k}(P/T^4)}{\partial^i(\mu_B/T)\partial^j(\mu_Q/T)\partial^k(\mu_S/T)}, \quad (3.2)$$

where, the pressure,  $P$ , is calculated accordingly to,

$$P = \frac{T}{V} \ln Z. \quad (3.3)$$

Experimentally, one computes the central moments ( $M$ ) of particle number distributions according to,

$$M_{BQS}^{ijk} = \langle (B - \langle B \rangle)^i (Q - \langle Q \rangle)^j (S - \langle S \rangle)^k \rangle. \quad (3.4)$$

Using the fact that the generating function for the cumulants are given by the logarithm of the moments. One can express one in terms of the other. Up to the second-order, the relationship between cumulant and the central moment is one-to-one, so Equation 2.21 can be expressed as,

$$\chi_{XY}^{11} = \frac{1}{VT^3} M_{XY}^{11}. \quad (3.5)$$

Using equation 3.5 all the second-order diagonal and off-diagonal susceptibilities can be estimated by measuring second-order central moments or cumulants.

$$\begin{pmatrix} \sigma_Q^2 & \sigma_{QB}^{1,1} & \sigma_{QS}^{1,1} \\ \sigma_{BQ}^{1,1} & \sigma_B^2 & \sigma_{BS}^{1,1} \\ \sigma_{SQ}^{1,1} & \sigma_{SB}^{1,1} & \sigma_S^2 \end{pmatrix}$$

Importantly note that Equation 3.5 involves the volume ( $V$ ) and the temperature ( $T$ ) of the system produced. The volume is not a well-defined quantity in heavy-ion collision. So to cancel the volume effect, the "Koch ratios" [59] can be suitably constructed. In the partonic phase, the ratios  $\chi_{BS}^{11}/\chi_S^2$  and  $\chi_{QS}^{11}/\chi_S^2$  become  $-1/3$  and  $1/3$  respectively. However, it is not possible to find such factor for the ratios like  $\chi_{QB}^{11}/\chi_B^2$ , because both light and strange quarks contribute in this case. One constructs the following ratios of off-diagonal and diagonal susceptibilities:

$$C_{BS} = -3 \frac{\chi_{BS}^{11}}{\chi_S^2} \approx -3 \frac{\sigma_{BS}^{11}}{\sigma_S^2}, \quad C_{SB} = -\frac{1}{3} \frac{\chi_{BS}^{11}}{\chi_B^2} \approx -\frac{1}{3} \frac{\sigma_{BS}^{11}}{\sigma_B^2}, \quad (3.6)$$

$$C_{QS} = 3 \frac{\chi_{QS}^{11}}{\chi_S^2} \approx 3 \frac{\sigma_{QS}^{11}}{\sigma_S^2}, \quad C_{SQ} = \frac{\chi_{QS}^{11}}{\chi_Q^2} \approx \frac{\sigma_{QS}^{11}}{\sigma_Q^2}, \quad (3.7)$$

$$C_{QB} = \frac{\chi_{QB}^{11}}{\chi_B^2} \approx \frac{\sigma_{QB}^{11}}{\sigma_B^2}, \quad C_{BQ} = \frac{\chi_{QB}^{11}}{\chi_Q^2} \approx \frac{\sigma_{QB}^{11}}{\sigma_Q^2}. \quad (3.8)$$

In the following sections, we will discuss these susceptibility ratios (in HRG) and cumulant ratios (in UrQMD) as a function of collision energy and detector acceptance in terms of transverse momentum ( $p_T$ ) and pseudo-rapidity ( $\eta$ ).

### 3.3 Collision energy dependence of cumulant ratio

Event-by-event off-diagonal to diagonal cumulant ratios,  $C_{BS}$ ,  $C_{QS}$ , and  $C_{QB}$  as a function of  $\sqrt{s_{NN}}$  for  $Au + Au$  top central (0-5% of the total cross-section) collisions are shown in Fig. 3.1. Both HRG and UrQMD model results are presented within the kinematic range  $0.2 < p_T < 2.0$  GeV/c. Both models show similar trends for the ratios, although there are quantitative differences.  $C_{BS}$  decreases from low to high collision energy and remains constant  $\sqrt{s_{NN}} \geq 27$  GeV.  $C_{QS}$  increases with energy and then remain constant after  $\sqrt{s_{NN}} = 20$  GeV, whereas the value of  $C_{QB}$  shows a decreasing trend with increasing collision energy.

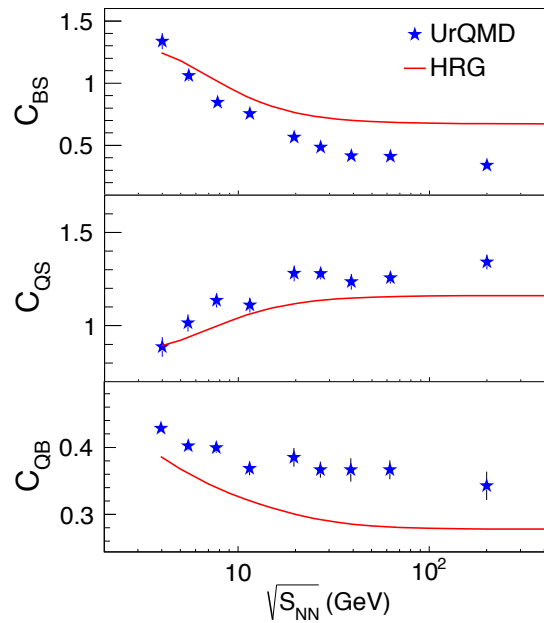


Figure 3.1: Collision energy dependence of "Koch ratios" for central (0-5%) Au+Au collisions predicted by the HRG and UrQMD models. Error bars are within the marker size in URQMD calculations.

These trend as a function of beam energy can be understood by a thermal model framework of the HRG model. For uncorrelated gas of hadrons,  $C_{BS}$  can be approximated from the mean hadron yields [59],

$$C_{BS} \approx 3 \frac{\langle \Lambda \rangle + \langle \bar{\Lambda} \rangle + \dots + 3\langle \Omega^- \rangle + 3\langle \bar{\Omega}^+ \rangle}{\langle K^+ \rangle + \langle K^0 \rangle + \dots + 9\langle \Omega^- \rangle + 9\langle \bar{\Omega}^+ \rangle}. \quad (3.9)$$

$C_{BS}$  gets a dominant contribution from  $\Lambda$  (lightest strange baryon particle) in the numerator while kaons (lightest strange meson particle) mainly dominate the denominator.  $\mu_B$  increases with a decrease in collision energy. This enhances the relative contribution from  $\Lambda$  compared to kaons resulting the decreasing trend of  $C_{BS}$  with  $\sqrt{s_{NN}}$ . For  $C_{QS}$ , it receives dominant donations from the kaons (charged kaon in numerator being the lightest charged-strange particle) both numerator and denominator. However, the contribution from the lightest strange baryons to the denominator keeps decreases with collision energy, which explain the monotonic increasing trend for  $C_{QS}$  with  $\sqrt{s_{NN}}$ . Finally, the decreasing trend of  $C_{QB}$  can also be the effect of neutral baryon production (like neutron,  $\Lambda$ , etc.) which contribute only in the denominator and decrease with collision energy.

### 3.4 Particle species dependence of cumulant

Conserved charge susceptibilities and their ratios strongly depend on hadron species. In experiments, only charged hadrons are measured directly. In an event-by-event basis analysis only pion, kaon and protons, and their antiparticles can be identified with considerable purity. Neutral hadrons, like neutron,  $K^0$  and  $\Lambda$ , which significantly contribute to baryon fluctuations, strange fluctuations, and baryon-strange correlations, are very difficult to measure on an event-by-event basis. However,  $\Lambda$  can be reconstructed from  $p\pi^-$  (branching ratios:  $63.9 \pm 0.5$ ), although in event-by-event reconstruction purity is very low. We have estimated the effects of such missing contributions by computing all the cumulant ratios for three different hadron sets,

set-i: considering all hadrons as in Fig. 3.1,

set-ii: with  $p, \bar{p}, K^\pm, \pi^\pm$  and  $\Lambda, \bar{\Lambda}$ , and

set-iii: only considering  $\pi^\pm, K^\pm, p$  and  $\bar{p}$ .

Figure 3.2 shows the  $2^{nd}$ -order diagonal and off-diagonal cumulants and their ratios as a function of collision energy for the above mention three different hadron sets using UrQMD model in central (0-5%)  $Au + Au$  collisions.

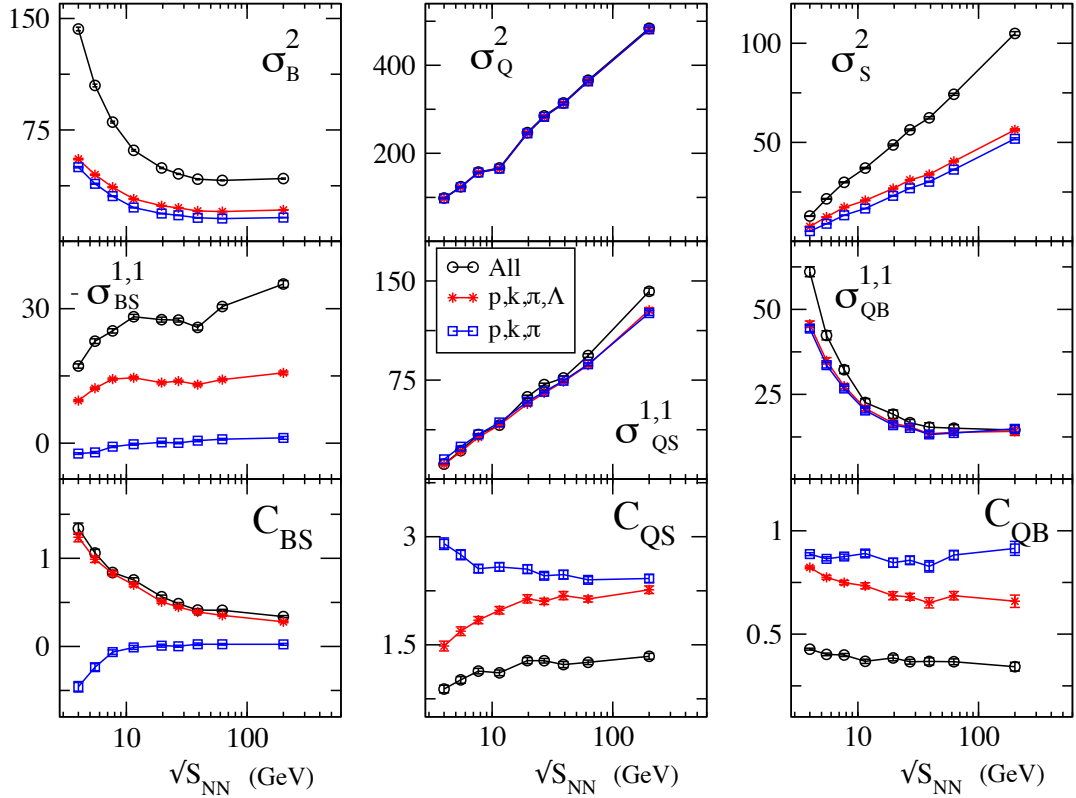


Figure 3.2: Particle species dependence diagonal and off-diagonal susceptibilities and their ratios in central (0-5%)  $Au+Au$  collisions using the UrQMD model calculations.

For  $C_{BS}$  the results for set-i and set-ii is almost similar and largely differ from set-iii, i.e., only with  $\pi^\pm, K^\pm, p$  and  $\bar{p}$ . It also proves that the dominant contribution in  $C_{BS}$  comes from  $\Lambda$ . Figure 3.2 shows that with all particles as well as using only  $\pi^\pm, K^\pm, p, \bar{p}$  and  $\Lambda, \bar{\Lambda}$   $C_{BS}$  is

almost identical. Thus the contribution of  $\Sigma_0$  is probably sub-dominant. In UrQMD, the yields of multi-strange baryons are highly underestimated [88, 89].  $C_{QB}$  shows a very weak dependence with  $\sqrt{s_{NN}}$  and the set-ii is roughly twice of the case when we include all hadrons. This is due to the uncounted neutrons in  $\sigma_B^2$  in set-ii. Similarly, the difference in  $C_{QS}$  in the three different sets can be explained by missing contributions of neutral-kaons in the denominator of set-ii and set-iii as well as missing higher mass strange particle in set-iii.

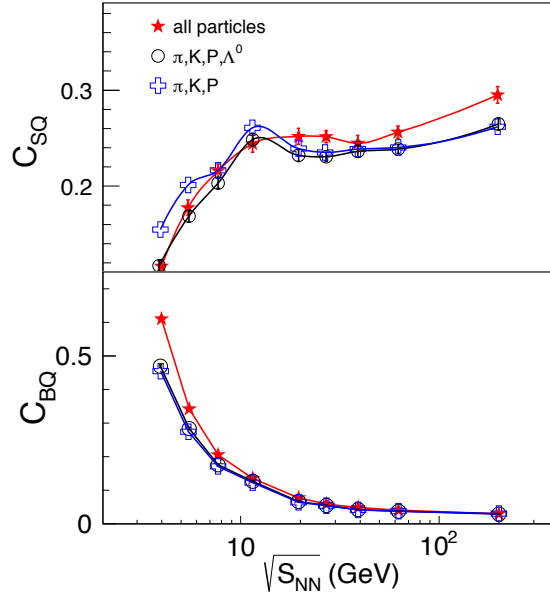


Figure 3.3: The measurements for  $C_{SQ}$  and  $C_{BQ}$  are robust under the different choices of the particle set for central (0-5%) Au+Au collisions.

We have also constructed the ratios  $C_{SQ}$  and  $C_{BQ}$  by normalizing the strange-charge and baryon-charge correlation by  $\sigma_Q^2$  as shown in Fig. 3.3. This minimizes the hadron set dependence because in both of these susceptibility ratios, the leading contribution in both numerator and denominator comes from the event-by-event identified hadron set.

### 3.5 Acceptance dependence of cumulant

Event-by-event limited particle identification, centrality determination, realistic detector efficiency correction, and finite kinematic detector acceptance in  $\eta$  and  $p_T$  – all these effects smear the signal for susceptibilities in the experiment [90]. Some of these effects have been already discussed in reference [91, 92, 93, 94, 95]. In the previous section, we discussed the effects of limited event-by-event particle identification. In this section, we will now discuss the effect of limited acceptance coverage in  $p_T$  and the pseudorapidity.

In principle, grand canonical fluctuations trivially scale with the system volume when the system is in contact with an infinite bath. But in heavy-ion collisions, this is not true due to Global charge conservation. For large enough acceptance, the system size can become comparable with the bath which resulting in non-thermal fluctuations and suppress the thermal fluctuations [96, 56]. So for such cases, the interpretation of conserved charge fluctuations regarding thermal and critical phenomenon approach is not straightforward. Also, baryon stopping is a function collision energy, resulting in completely different conserved charge distributions in  $\eta$  for different collision energies.

Figure 3.4 shows the system to total phase space volume ratios ( $\mathcal{R}$ ) of net baryon (top panel) and total baryon (bottom panel) for  $Au + Au$  collisions using the UrQMD model. Here the ratios are plotted for three different acceptances ( $\eta < 1.5, 1.0$  and  $0.5$ ). Ideally, to observed grand canonical fluctuation  $\mathcal{R} \ll 0.5$ . For higher energies  $\mathcal{R}$  is much less than 0.5 for all three acceptance because particle production is spread out. However, at lower collision energies with smaller acceptance (like  $\eta < 0.5$ ), the condition remains to hold while for even larger acceptance window  $\mathcal{R}$  become higher than 0.5 signalling the inapplicability of GCE for net baryon fluctuation.

It indicates that over an extensive range of collision energies, a fixed  $\eta$ -acceptance does not correspond to the same system to total effective volume ratio [39]. We have made a detailed study

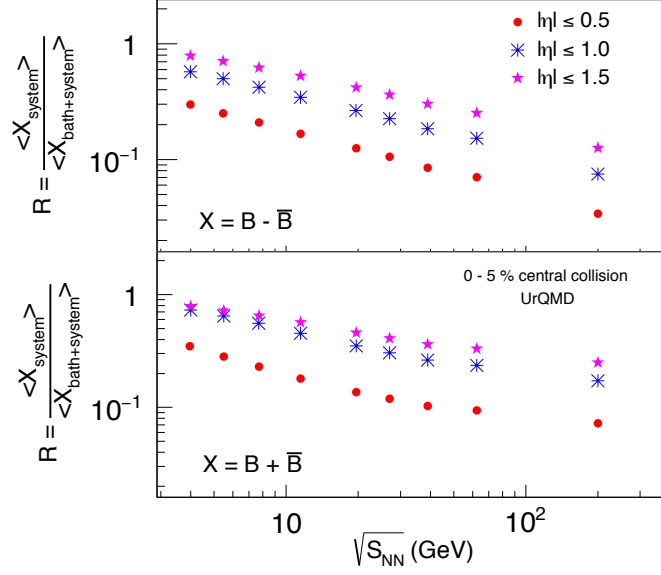


Figure 3.4: Ratios of net baryon (top panel) and total baryon (bottom panel) numbers within the analysis acceptance (system size) to the full phase space (bath + system) for 0-5% central Au+Au collisions as a function of  $\sqrt{s_{\text{NN}}}$  using the UrQMD model. The results are presented for three different  $\eta$  windows.

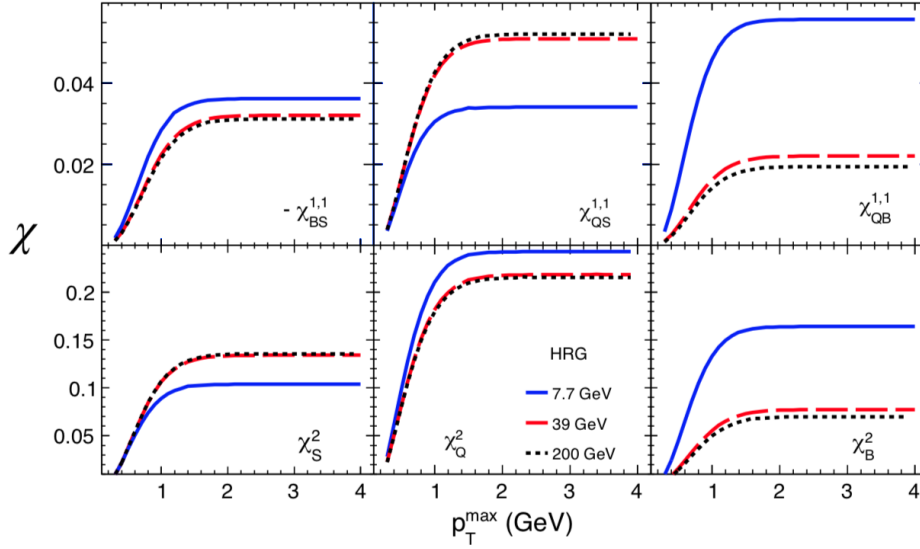


Figure 3.5: The  $p_T$ -acceptance dependence of the second-order off-diagonal and diagonal susceptibilities in the HRG model for central Au+Au collisions at  $\sqrt{s_{\text{NN}}} = 7.7, 39$  and  $200$  GeV.

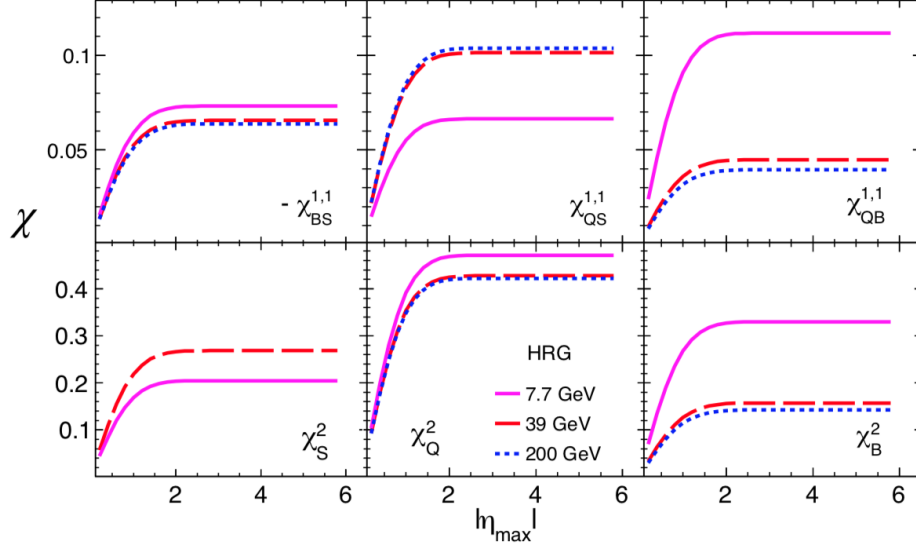


Figure 3.6: The  $\eta$ -acceptance dependence of the second-order off-diagonal and diagonal susceptibilities in the HRG model for central Au+Au collisions at  $\sqrt{s_{NN}} = 7.7, 39$  and  $200$  GeV.

of susceptibilities and cumulants on the acceptance window dependence in  $p_T$  and  $\eta$ .

### 3.5.1 Acceptance dependence susceptibilities from HRG model

First, we analyzed the  $p_T$  and  $\eta$ -acceptance dependence susceptibilities in Fig. 3.5 and 3.6 respectively. Using equation 3.1 and 3.2 one can express the susceptibilities due to  $h$ th hadron species as,

$$\chi_{hBQS}^{ijk} = \frac{g_h}{(2\pi)^2} \sum_{l=1}^{\infty} e^{l\mu_i/T} (-a)^{l+1} l^{(i+j+k)-4} B^i Q^j S^k \int_{-y_{rmax}}^{y_{rmax}} dy_r \text{Cosh}(y_r) \int_{y_{min}}^{y_{max}} dy y^2 e^{-y \text{Cosh}(y_r)}, \quad (3.10)$$

where  $y_{min} = \frac{l}{T} \sqrt{p_{Tmin}^2 + m_h^2}$  (similarly for  $y_{max}$ ) and the Boltzmann factor can be written as  $e^{-l\sqrt{p_T^2+m^2}/T \text{Cosh}(y_r)}$  in terms of rapidity and transverse momentum. For ease of understanding, we have written down the explicit cutoff dependence on the momentum rapidity  $y_r$  instead of

the pseudo-rapidity  $\eta$  which is more relevant experimentally. The  $\text{Cosh}(y_r)$  dependence ensures that thermal production of particles is more strongly suppressed in  $y_r$  as compared to  $p_T/T$ . In figure 3.5 and 3.6 we can see that the susceptibilities have strongly depended on the maximum value of transverse momentum ( $p_{T_{\max}}$ ) and pseudo-rapidity acceptance window ( $|\eta_{\max}|$ ). For a smaller value of acceptance, the susceptibilities are small and steadily grow with increasing  $\eta_{\max}$  and  $p_{T_{\max}}$  as an increase in phase space. Finally, these susceptibilities saturate to a constant value as the Boltzmann factor suppress any further contribution from the higher  $\eta$  and  $p_T$ .

### 3.5.2 Acceptance dependence cumulants from UrQMD model

Different  $2^{\text{nd}}$ -order conserved charge susceptibilities as a function of  $\eta$  and  $p_T$  acceptance are shown in Fig. 3.7 and 3.8 using the UrQMD model. These susceptibilities are plotted for three different beam energies in terms of event-by-event cumulants.

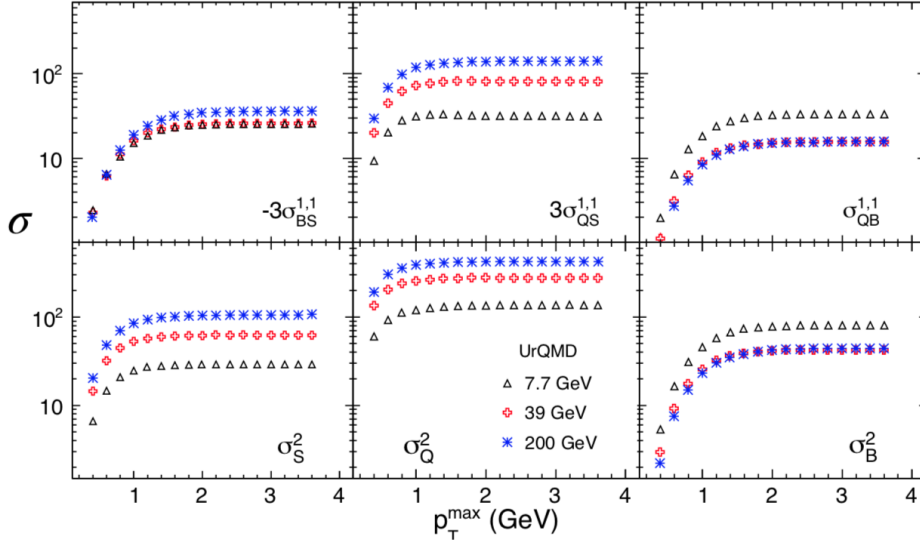


Figure 3.7: The  $p_T$ -acceptance dependence of the second-order off-diagonal and diagonal susceptibilities in the UrQMD model for 0-5% central Au+Au collisions at  $\sqrt{s_{\text{NN}}} = 7.7, 39$  and 200 GeV.

The transverse momentum dependence cumulants demonstrate a similar trend to that obtained

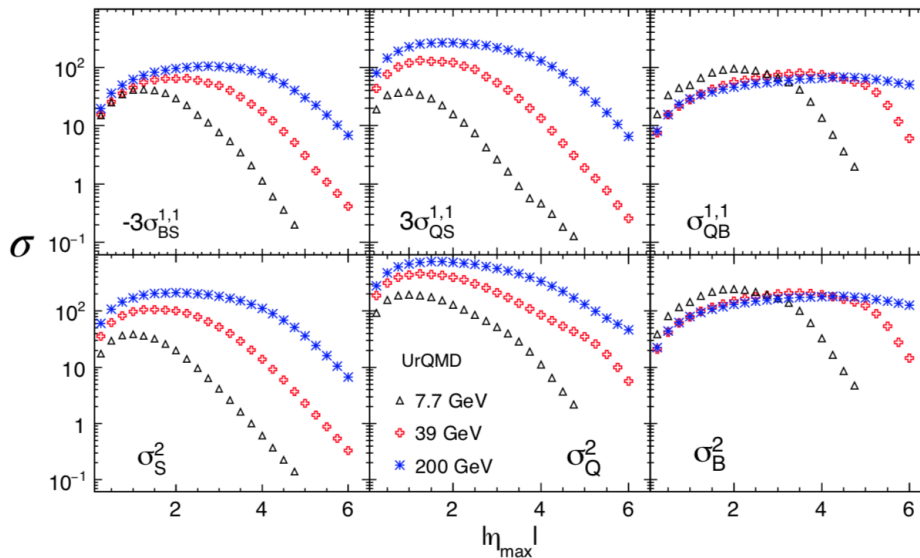


Figure 3.8: The  $\eta$ -acceptance dependence of the second-order off-diagonal and diagonal susceptibilities in the UrQMD model for 0-5% central Au+Au collisions at  $\sqrt{s_{NN}} = 7.7, 39$  and 200 GeV.

from HRG model. However, the  $\eta$ -window acceptance dependence of cumulants shows very different behaviour because of global charge conservation. There is an underlying increase for a small value of  $|\eta_{\max}|$  and attain a maximum value at intermediate rapidity window within  $|\eta_{\max}| = 1-2$  units depending upon collision energy. Finally, at large rapidity window cumulants go to zero as a result of the charge conservation effect at full phase space. This recommends that  $\Delta\eta \sim 2-3$  catch the full essence of conserved charge correlations.

### 3.5.3 Normalized cumulants and susceptibilities from UrQMD and HRG

In the earlier sections,  $\eta_{\max}$  and  $p_{T\max}$  dependence of the  $2^{\text{nd}}$ -order susceptibilities and cumulants are presented using the HRG and UrQMD model. This dependency can be compared and nicely summarized after they are suitably normalized. Additionally, The trivial volume dependence is expected to be cancelled in such normalization, and the cumulants from UrQMD can be compared with susceptibilities from HRG. Here, all susceptibilities have been normalized by their values at

$p_{T_{\max}} = 2$  GeV and  $|\eta| < 0.5$ . I denote these normalized susceptibilities and cumulants as  $\hat{\chi}$  and  $\hat{\sigma}$ , respectively. Hence by construction, for  $p_{T_{\max}} = 2$  GeV and  $\eta_{\max} = 0.5$ ,  $\hat{\chi}$  and  $\hat{\sigma}$  are equal to 1. Fig. 3.9 presents  $2^{nd}$ -order normalised susceptibilities of net- $B/Q/S$  in central  $Au + Au$  collisions at  $\sqrt{s_{NN}} = 7.7$  GeV and 200 GeV calculated with HRG and UrQMD models.

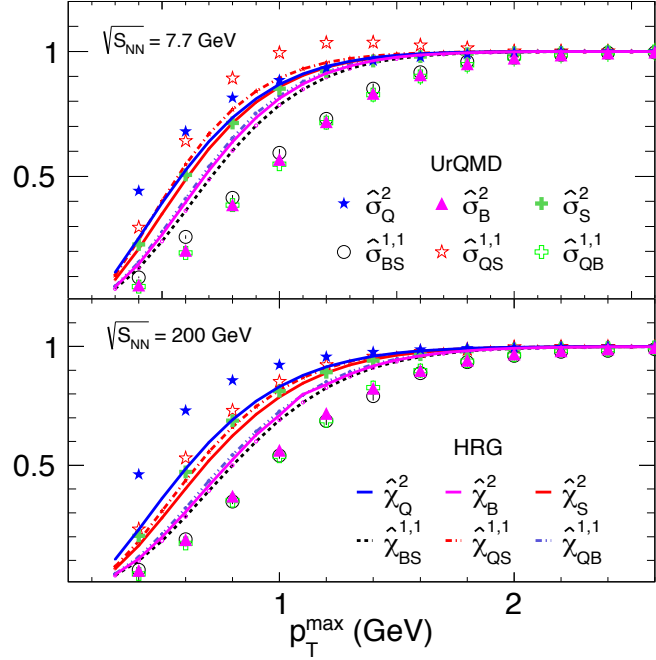


Figure 3.9: The  $p_T$ -acceptance dependence second-order diagonal and off-diagonal susceptibilities and cumulants normalized by their values at  $p_{T_{\max}} = 2$  GeV and  $|\eta_{\max}| < 0.5$  for central Au+Au collisions at  $\sqrt{s_{NN}} = 7.7$  GeV (upper panel) and 200 GeV (lower panel) for both the HRG and UrQMD model.

For smaller transverse momentum acceptance the cumulants approach zero as the system volume approaches to zero. We can observe that the fluctuations grow with  $p_T$ -acceptance and then saturate to a constant value. Interestingly, we can observe a clear ordering of conserved charge susceptibilities with the increase of  $p_T$  acceptance in both HRG and UrQMD model.  $\hat{\chi}_Q^2$  mostly dominated by net-pion and reached its saturation value fastest while  $\hat{\chi}_B^2$ , which gets maximum contribution from net-proton and neutron saturates at larger values of  $p_{T_{\max}}$ . On the otherhand

$\hat{\chi}_S^2$ , which is mainly sensitive to kaons saturates at an intermediate  $p_{T,max}$ , closer to that of  $\hat{\chi}_Q^2$ .

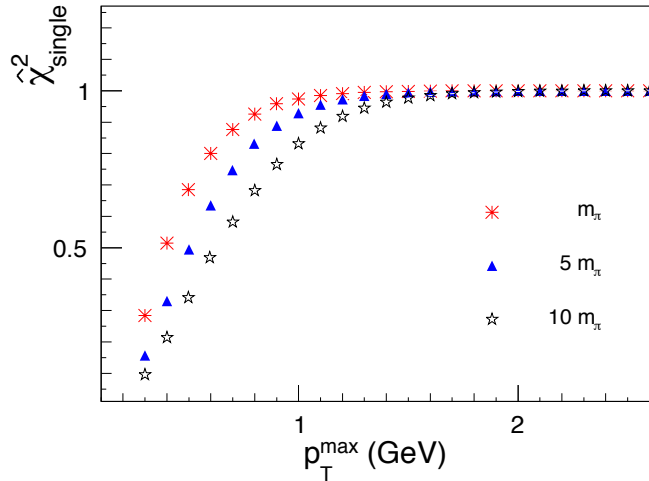


Figure 3.10: The maximum  $p_T$ -acceptance dependence of the second-order susceptibility normalized by the value for  $p_{T,max} = 2$  GeV and  $\eta_{max} = 0.5$  for a single particle system for three different masses of the particle.

In the HRG setup, it is straightforward to understand that such ordering in normalized susceptibilities comes from the mass ordering. It can be studied within the framework of a single particle ideal gas as shown in Fig. 3.10. With the increase in particle mass, the saturation in  $\hat{\chi}_{single}^2$  shifted towards a higher  $p_{T,max}$ . Comparing HRG results to those of UrQMD, we find the effect of the mass ordering gets even more pronounced as observed in Fig. 3.9.

In Fig. 3.11, we have plotted the  $\eta_{max}$  acceptance dependence of all the normalized second-order susceptibilities with  $p_{T,max} = 2$  GeV. All the susceptibilities/cumulants are normalized by their values at  $|\eta_{max}| < 0.5$  and  $p_{T,max} = 2$  GeV. For HRG, all the  $2^{nd}$ -order susceptibilities fall on top of each other. The UrQMD result also show a similar behaviour for  $|\eta_{max}| \leq 1$ . For  $|\eta_{max}| > 1$  the normalized cumulants again decrease and tend towards zero except for the baryonic cumulants, which clearly decided by the baryon stopping phenomenon.

Event-by-event fluctuation and correlation of conserved charges have been considered as im-

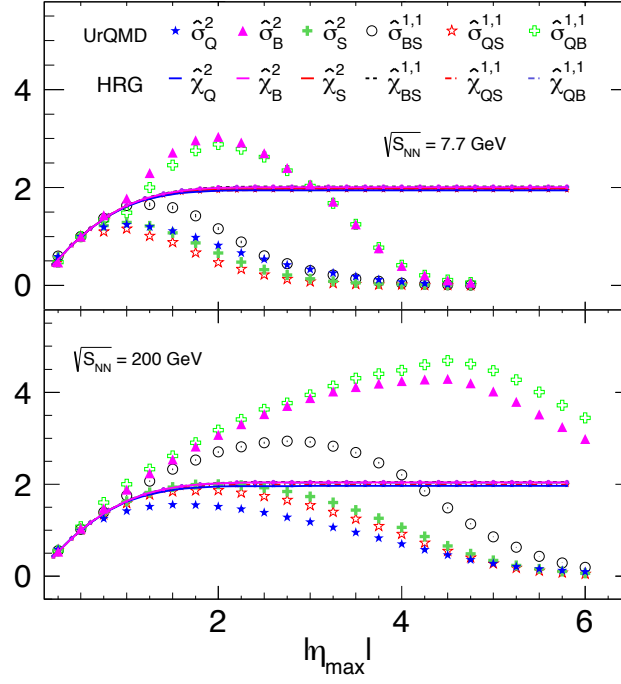


Figure 3.11: The  $\eta_{\max}$  dependence of all second-order diagonal and off-diagonal susceptibilities normalized by their values for  $p_{T_{\max}} = 2$  GeV and  $\eta_{\max} = 0.5$  in the UrQMD and HRG models.

portant observables to probe the QCD phase diagram in heavy-ion collisions. These fluctuations carry information of the thermal condition prevalent in the fireball and also supposed to bear signature expected from near QCD critical point. Although the study of these susceptibilities is very well motivated, there are several experimental issues should be comprehended to interpret the experimental data and draw any physics conclusions. Using the thermal HRG model as well as non-thermal UrQMD models I have discussed some of the issues concerning limited particle identification as well as detector acceptance for all the second-order diagonal and off-diagonal susceptibilities.

## Chapter 4

# The Experimental Details

The data sets used in this analysis were collected during the Beam Energy Scan Program (BES-I) in 2010, 2011, and 2014 using the STAR detector. The STAR (Solenoidal Tracker at RHIC) is a major experiment at the Relativistic Heavy-Ion Collider (RHIC) located at Brookhaven National Laboratory (BNL) in Upton, New York on Long Island, USA. In this chapter, I will discuss the experimental components of the RHIC complex and STAR detector used during the collection of the data presented in this thesis.

### 4.1 Relativistic Heavy-Ion Collider (RHIC)

The RHIC facility is a multi-part accelerator complex that is capable of accelerating a range of nuclei to relativistic speeds. This facility was designed to provide  $\sqrt{s_{NN}} = 200$  GeV  $Au + Au$  collisions and polarized  $p + p$  collisions. A schematic of the facility is presented in Fig. 4.1. The RHIC ring consists of two hexagonal storage rings called "Yellow Ring," where the beam moves in the anticlockwise direction and "Blue Ring," where the beam moves in the clockwise direction. There are six interaction points at the middle of the six relevant straight sections where two rings cross. The circumference of the ring is 3.8 km. Four detector setup STAR, PHENIX, PHOBOS,

BRAHMS are located in four interaction points (6, 8, 10 and 2 o'clock position respectively) shown in Fig. 4.1. PHOBOS and BRAHMS are de-commissioned since 2008. STAR is presently ongoing experiment at the RHIC collider ring.

## 4.2 The STAR detector

The STAR detector is located at the 6 o'clock position of the RHIC ring. It weights over 1200 tons and is about 10 meters tall. The main aim of STAR is to study strongly interacting matter, known as Quark-Gluon Plasma. The STAR detector provides an excellent tracking and particle identification over a large solid angle and in high multiplicity environment.

The detector consists of several subsystems, as shown in Fig. 4.2, enclosed in a solenoidal magnet that provide a uniform magnetic field (maximum value of 0.5 T) parallel to beam direction. The main tracking detector systems are a time projection chamber (TPC), two Forward TPCs (FTPC) and a silicon vertex tracker (SVT). The event multiplicity is measured by the Central Trigger Barrel (CTB). The Time of Flight (TOF) detector extend the particle identification up to a higher momentum range. The Barrel electromagnetic calorimeter plays a significant role towards the detection of photons, electrons and  $\pi^0$ . The detector subsystem also includes two zero-degree calorimeters (ZDCs) at both of the ends, that measure the spectator neutrons. The Photon Multiplicity Detector (PMD) is a pre-shower gas detector measures the photon multiplicity in the forward region. It is located outside the magnet system at a distance 550 cm from the center of the STAR detector [98]. By comparing the measured multiplicity with the produced charged particle multiplicity, the PMD detector gives information about the photon enrichment in an event or set of events. In the present analysis, tracking is done by the TPC, and particle Identification are done by both TPC and TOF detector. Below, I will give an overview of these two detector subsystems. More general interaction to the STAR detector can be found in reference [99].

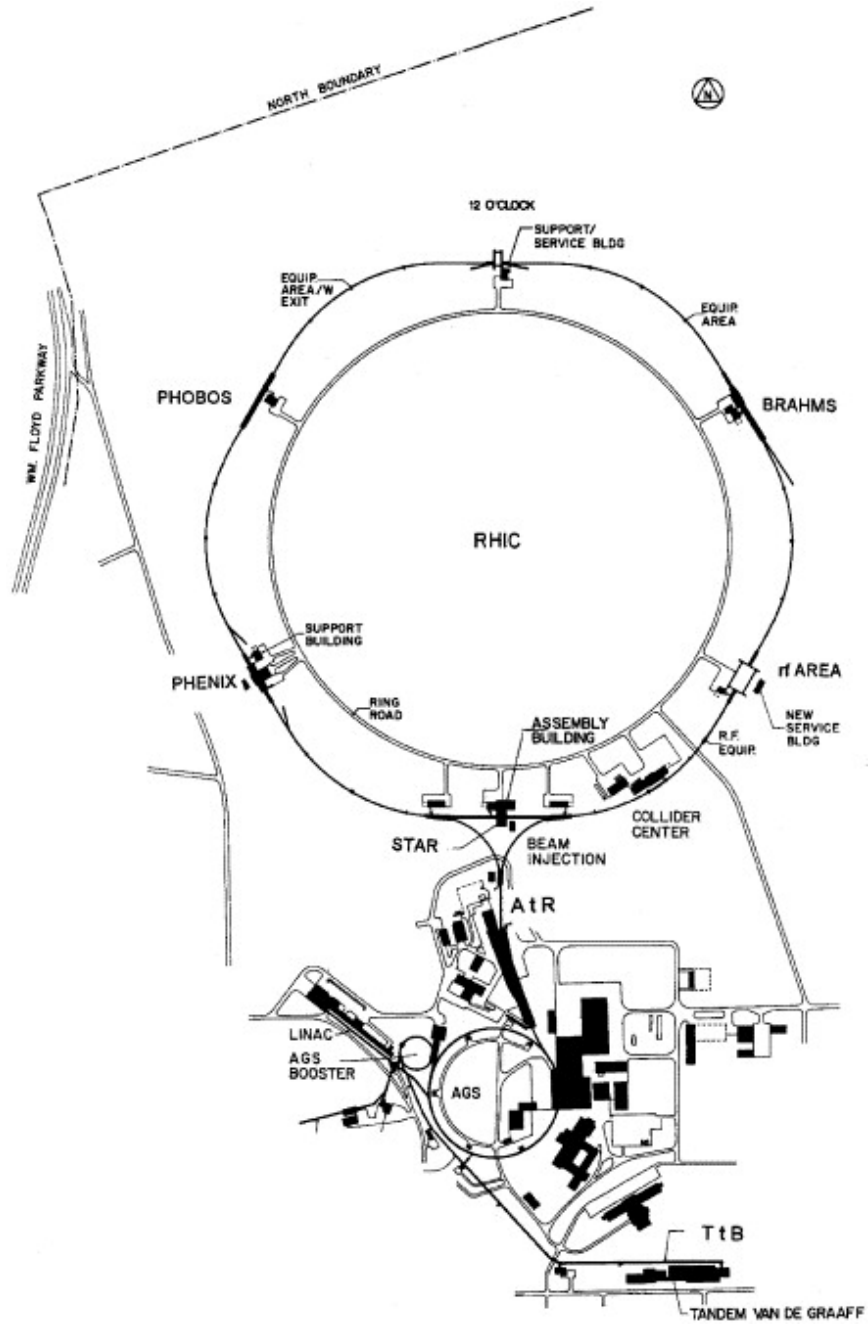


Figure 4.1: A schematic of the RHIC accelerator complex layout obtained from reference [97].

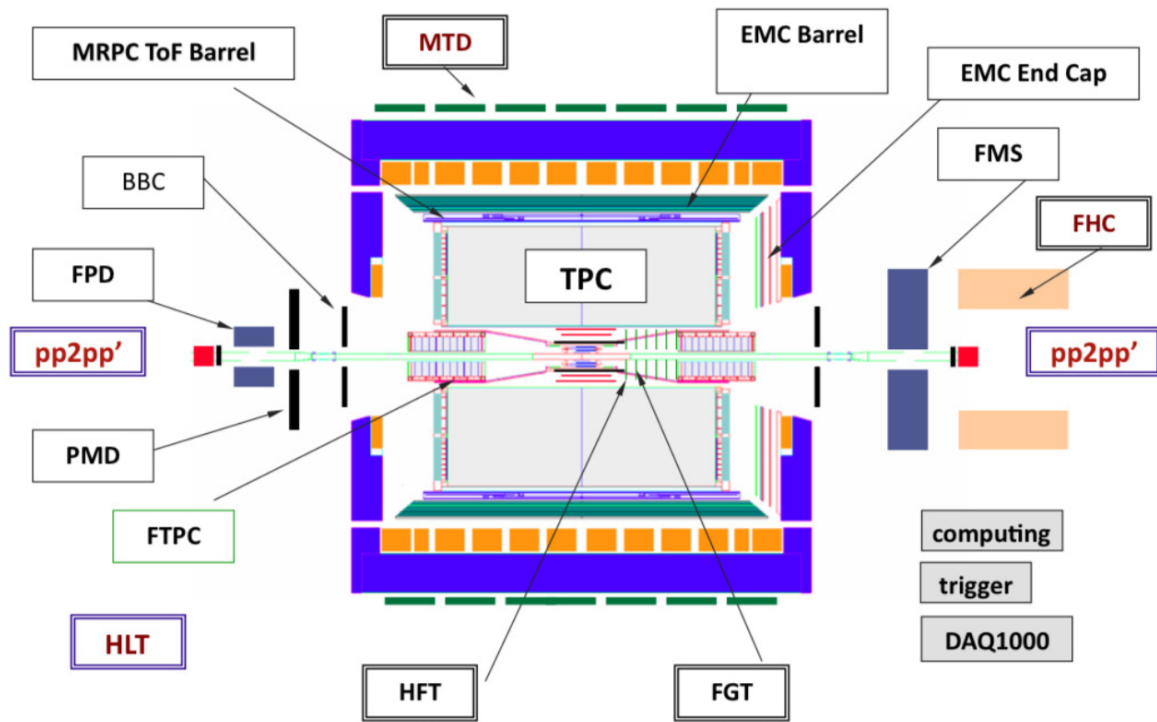


Figure 4.2: STAR detector system layout.

### 4.2.1 The Time Projection Chamber (TPC)

Time Projection Chamber (TPC) is the main subsystem of the STAR detector. It can track up to  $\sim 4\text{K}$  particles in pseudorapidity range  $|\eta| \leq 1.8$  within the full azimuthal angle ( $\Delta\phi = 2\pi$ ). It is a cylindrical volume, 420 cm in length and has 50 cm and 200 cm inner and outer radius. A schematic view of STAR TPC is presented in Fig. 4.3.

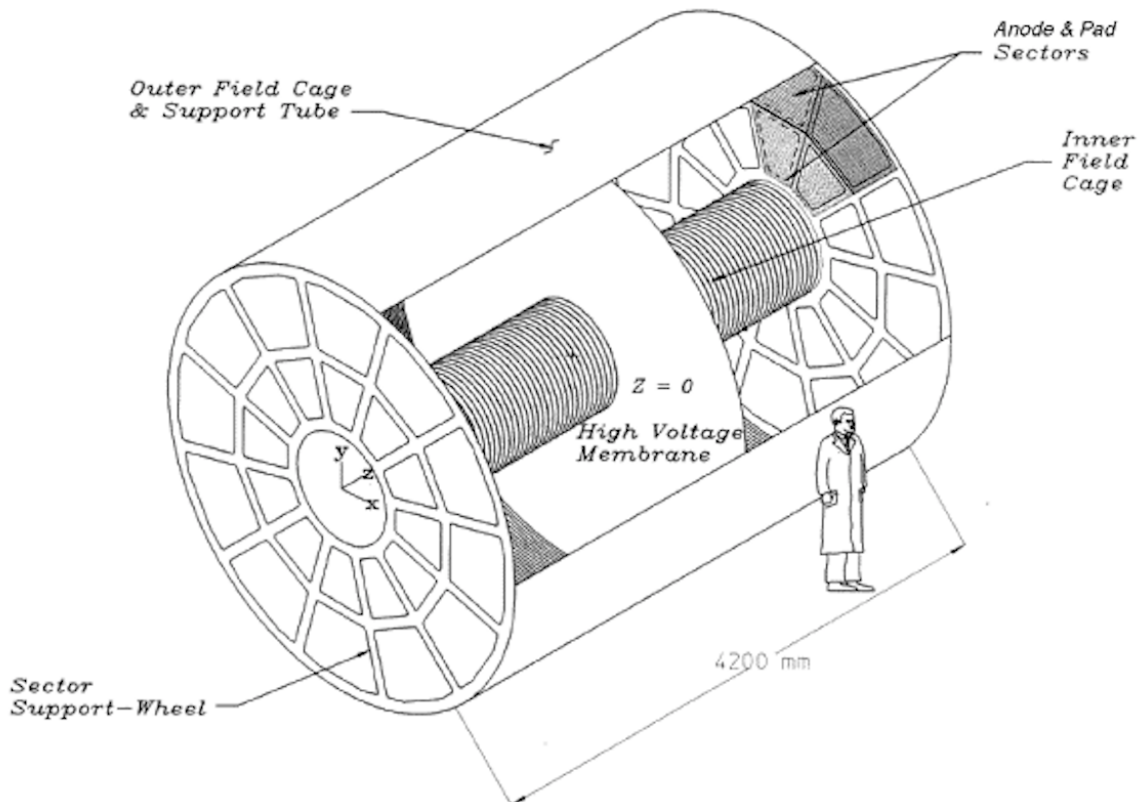


Figure 4.3: The three-dimensional schematic diagram of the STAR TPC obtained from reference [100]

The TPC volume is filled with P10 gas (90% Argon + 10% Methane). The TPC gas pressure is maintained slightly above atmospheric pressure so that oxygen and water vapor do not enter the TPC volume and oxidize its surface. The TPC gas was chosen by considering the gas purity, drift velocity, cost, and safety. Argon is a stable gas which restricts spurious ionization. It is also

relatively economical and has a very low affinity for free electrons. Methane gas works as an energy absorber. It has relatively large mass and multiple degrees of freedom (rotational, vibrational, etc.) which allow it to absorb kinetic energy from drifting electrons (giving the electron a constant drift velocity), ionized argon atom, and quench the propagation of UV photons throughout the TPC volume.

The TPC consists of an outer field cage (OFC), an inner field cage (IFC) and two end caps. The OFC and IFC provide a nearly perfect electric field in which the electrons drift to the anode plane. The readout end caps are kept at the ground potential and act as anode. A thin conducting central membrane (CM) is located in the x-y plane, which bisects the TPC cylinder in east and west section. The CM is made of 70  $\mu\text{m}$  thick carbon coated Kapton and maintained at -28kV voltage. A resulting electric field of  $\sim 135$  V/cm is maintained between the CM and readout end caps along the  $\pm z$ -direction. The electric field produced a constant drift velocity (about 5.45 cm/ $\mu\text{s}$ ) of electrons.

The readout electronics is based on Multi-Wire Proportional Chamber (MWPC). The MWPCs are located at the readout endcaps. The complete readout system is divided into 24 sectors, having 12 readout sector in each half of the TPC. A schematic of a single sector of TPC is shown in Figure 4.5. Each sector further divided into inner and outer subsectors. The inner sector has 13 pad rows while the outer sector has 32. This means that each track can have its position and energy loss recorded up to 45 times.

### **Track Reconstruction**

When a charge particle passes through the TPC volume, it ionized the Argon atoms along its path. As a result, a cluster of free electrons drifted to the end caps of the TPC and produced 'hit'. The x,y location of the readout pad is used to determine the transverse area of the hit's and the drift

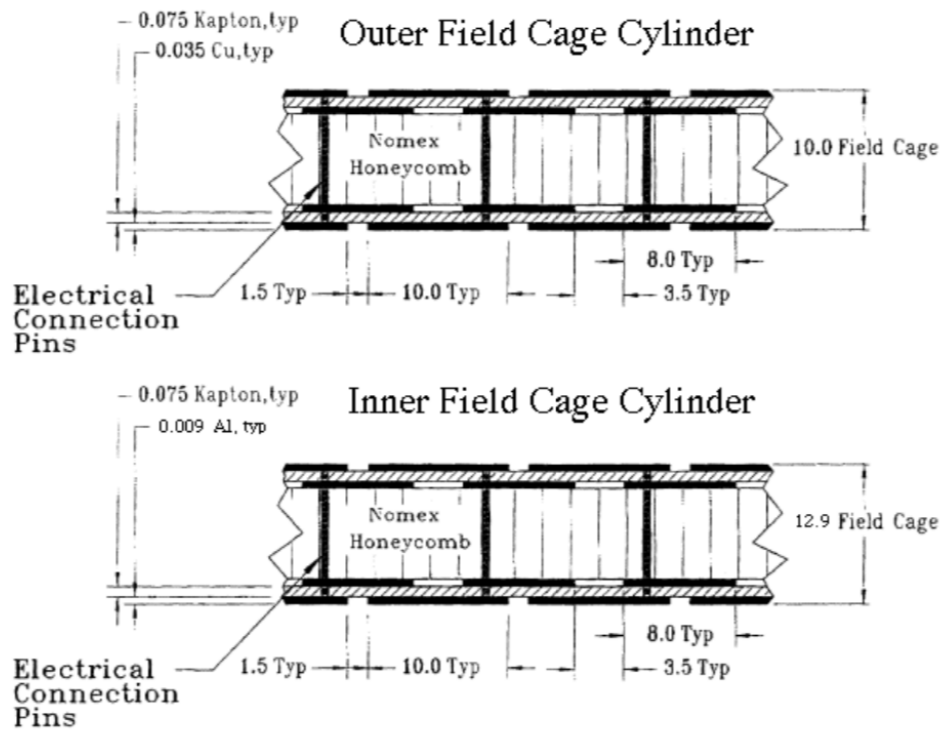


Figure 4.4: A Cutaway view of the Outer and Inner field cage (OFC and IFC, respectively). Dimensions (Typ) are in mm.

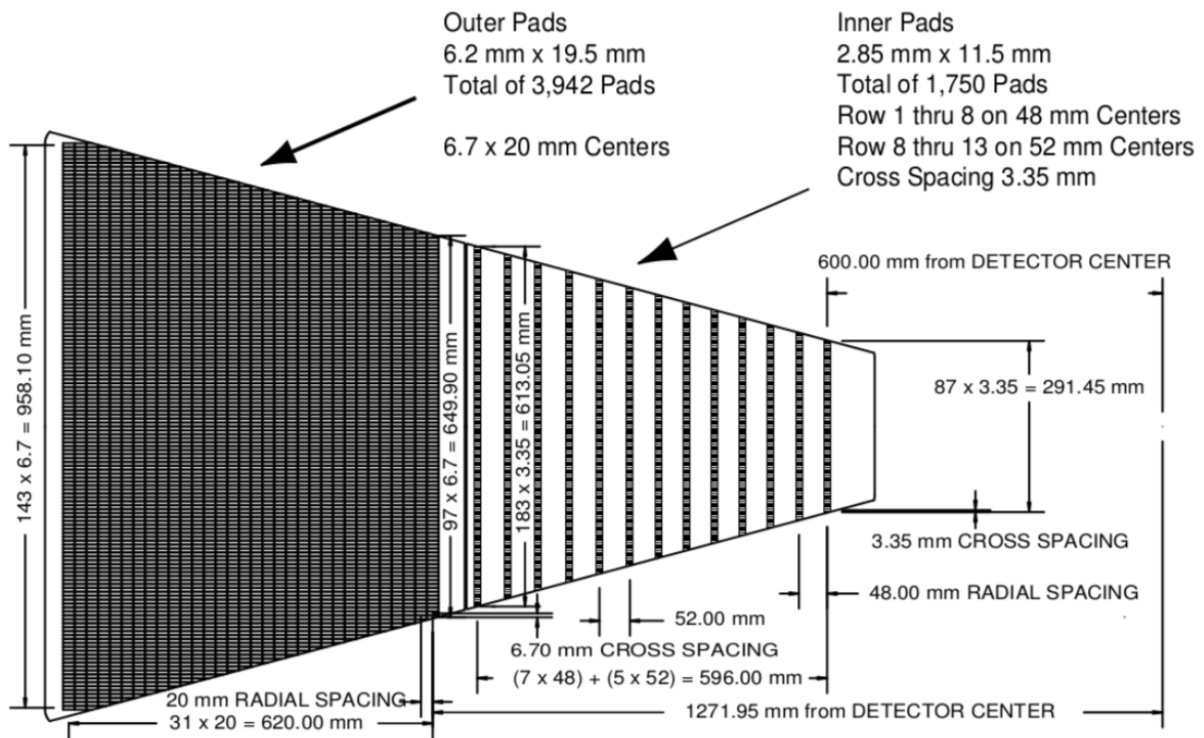


Figure 4.5: Schematic of a single anode sector of the TPC [100]. The inner portion of the sector is on the right, and the outer is on the left.

time of electron is used to determine its  $z$  location. After finding the positions of the clusters, the Time Projection Chamber Tracker (TPT) algorithm is used to reconstruct the tracks by a helical trajectory fit. Due to the presence of the strong magnetic field, the charge particle trajectories are primarily helix, but there can be a deviation from the helical shape due to energy loss in the gas and multiple Coulomb scattering. Global tracks are extracted from the TPC track information together with the inner tracking detector by the Kalman filtering process. Next step is to find the primary vertices which represents the location of an A+A collision. This is done using vertexing algorithm by extrapolating the fit helices to the  $z$ -axis. By examining the density of tracks as a function of  $z$ , a set of vertex candidates are determined. Now the global tracks are refitted with helices using the associated vertices as the first point in the helix. The reconstruction efficiency of primary tracks depends on the track quality cuts, particle type, and track multiplicity. All tracks are assumed to have unit charge, and the sign of charge is determined from handedness of the helix. The transverse momentum of the track is determined by the radius of curvature of the helix, and the longitudinal momentum is determined by turn density.

### Particle Identification

Charge particle identification is performed through the energy loss mechanism inside the TPC volume due to interaction with the TPC medium. Physics of this process is described by the Bethe-Bloch formula which predicts the energy-loss per unit length as a function of  $p/m$  ( $= \beta\gamma$ ). The energy-loss is depending on the mass of the charge particle. Different particle loses energy at a different rate according to their mass for a given value of  $\beta\gamma$ . The ionization energy loss can be described by the Bichsel curves [101] which is an extension of the Bethe-Bloch formula.

$$-\frac{dE}{dx} = Kz^2 \frac{Z}{A} \frac{1}{\beta^2} \left[ \frac{1}{2} \ln \left( \frac{2m_c c^2 \beta^2 \gamma^2 T_{max}}{I^2} \right) - \beta^2 - \frac{\delta(\beta\gamma)}{2} \right], \quad (4.1)$$

where,  $A$  = atomic Mass of the absorber (g/mol),  
 $Z$  = atomic number of the absorber,  
 $z$  = atomic number of the incident particle,  
 $\frac{K}{A} = 4\pi N_A r_e^2 m_e c^2 / A$  ( $cm^3/g$ ),  
 $r_2$  = classical electro radius (fm),  
 $m_e$  = mass of electron (MeV),  
 $N_A$  = Avogadro's constant (1/mol),  
 $T_{max} = \frac{2m_e c^2 \beta^2 \gamma^2}{1 + 2\gamma(m_e/m_0) + (m_e/m_0)^2}$   
= maximum energy transfer (MeV),  
 $m_0$  = mass of Incident particle,  
 $I$  = mean excitation energy (eV),  
 $\delta(\beta\gamma)$  = aaterial dependent density effect correction.

The energy loss of a particle moving through the TPC volume is proportional to the number of electrons collected in each hit. In the STAR TPC each track has a maximum of 45 hits. Therefore, each track has up to 45 independent  $dE/dx$  measurements. The value of  $dE/dx$  at each hit is primarily a Landau distribution. Since the Landau distribution has a long high-side tail, so a sample average of 45 measurements can give a skewed at high  $dE/dx$  values. Thus the averaging is done by calculating the truncated mean of the 70% of the measurements and removing remaining 30% of the extensive measurements.

Figure 4.6 shows the energy loss for charged tracks as a function of particle momentum. The red lines are theoretical predictions from Bichsel functions for different particles, and the band represents the measured values of  $dE/dx$ . The TPC allows for charged pions and kaons identification

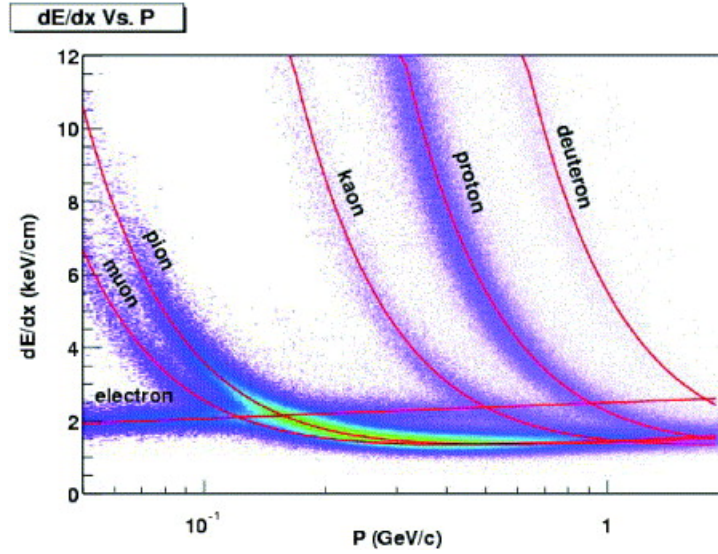


Figure 4.6: The energy loss distribution for charge particles in the STAR TPC. The magnetic field was 0.25T [100].

up to transverse momentum of 0.7 GeV/ $c$  and protons identification up to 1 GeV/ $c$ .

#### 4.2.2 Time of Flight (TOF)

The TOF system used to extend the particle identification of charge particle over a broader range of momentum. It is a system of a thin cylindrical shell that encloses the surface of the TPC and consists of two detectors, one called pVPD, the Pseudo Vertex Position Detector, (the start detector), and other is TOFp, Time-Of-Flight Patch, tray (the stop detector). A schematic diagram of the TOF location for one tray with pVPD is shown in Fig. 4.7. Two VPDs were installed 5.4 m away in each direction from the TPC center along the beam line. It covers  $\sim 19\%$  of the total solid angle in  $4.43 < |\eta| < 4.94$ . The TOF detector system is composed of 120 trays. Each unit is based on the Multigap Resistive Plate Chamber (MRPC) technology. In all, 60 for each east and west half and covers the full azimuth and have pseudorapidity range  $|\eta| < 0.9$ . Each tray contains

32 MRPC modules placed along the beam line direction around the TPC. MRPC's consists of resistive plate chambers with a series of uniform gas spacing. MRPC's works in avalanche mode. High voltage in the outer surface generates a strong electric field in the gas spaces. While passing through the chamber, the charge particles create avalanches. The sum of the avalanches from all gas gaps is the induced signal on the pads.

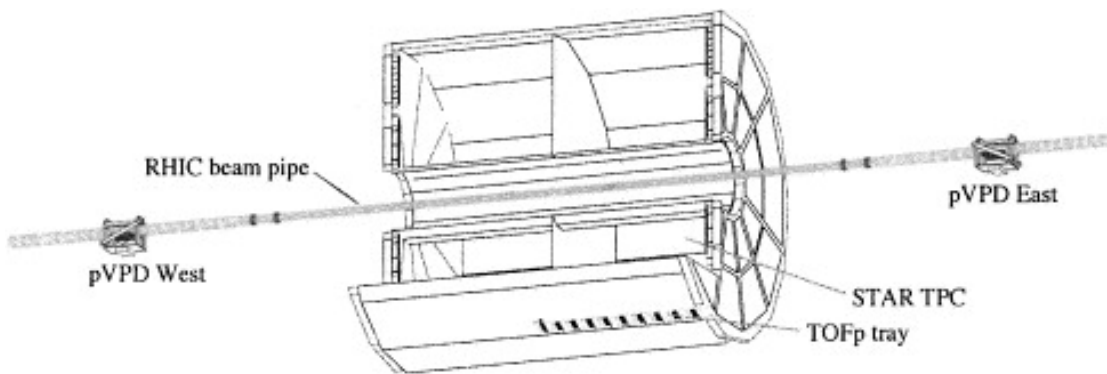


Figure 4.7: A scale drawing of the locations of pVPD and TOFp detectors [102].

### TOF hit Reconstruction to TPC track

Track measured and reconstructed in the TPC can now be matched with the hits in TOF pads by matching algorithm that extrapolates the trajectory of a TPC track to the radius of the TOF. The matching efficiency of TOF to TPC track is generally between 50-60%, and depends on particle multiplicity. We will discuss about these in the next chapter.

### PID via Time Of Flight

Particle identification using the TOF detector is achieved by measuring the velocity and mass of a track. The TOF system provides the flight time, and TPC gives the momentum and path length

information. The inverse velocity and associated mass are calculated from,

$$\frac{1}{\beta} = \frac{c\Delta t}{s} \quad (4.2)$$

$$M^2 = p^2 \left( \left( \frac{1}{\beta} \right)^2 - 1 \right) \quad (4.3)$$

where

$p$  = momentum,

$\Delta t$  = flight time,

$s$  = total path length,

$c$  = velocity of light.

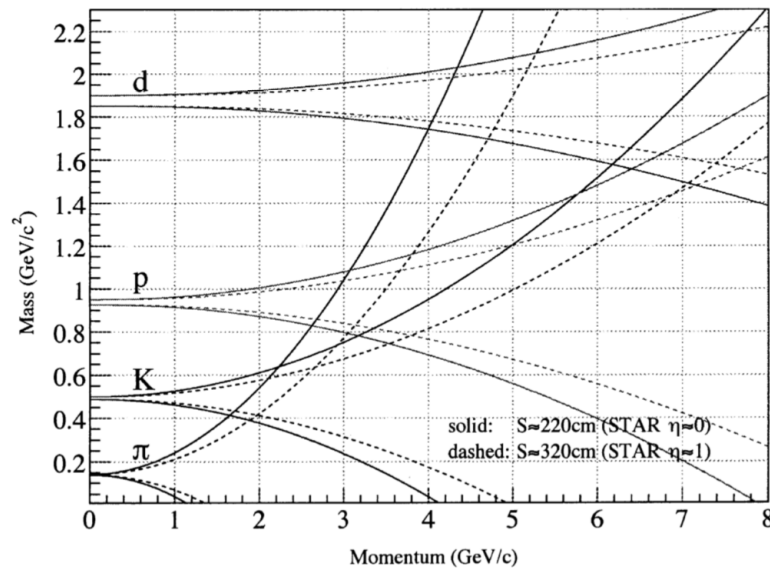


Figure 4.8: Momentum dependence of the particle identification capabilities of a TOF system with a time resolution of 100 ps [102].

The PID capabilities of the STAR detector using TOF are shown in Fig. 4.8. From the above

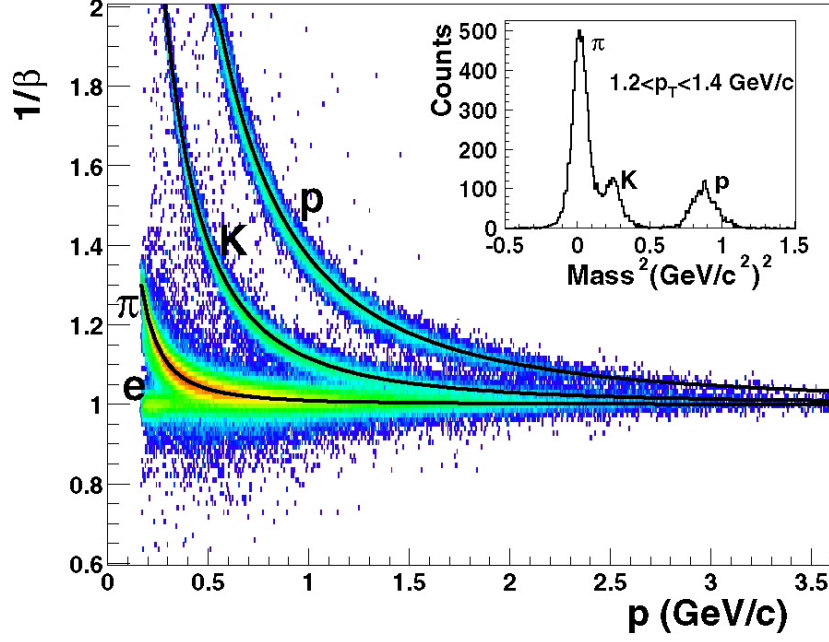


Figure 4.9: TOF  $1/\beta$  as a function of momentum from 200 GeV  $d + Au$  collisions [103].

equation, one can estimate the quantity  $\Delta M$  [102] as,

$$\Delta M/M = \frac{\Delta p}{p} \oplus \gamma^2 \left[ \frac{\Delta s}{s} \oplus \frac{\Delta t}{t} \right]. \quad (4.4)$$

Here  $\Delta t$  is TOF time resolution of 100 ps,  $\Delta p/p$  is relative momentum resolution about 1.3%, and  $\Delta s/s$  is the relative path resolution of 0.2%. In the Fig. 4.8, the upper pair lines indicate the dependence of  $M + \Delta M$  and lower pair lines represents the dependence of  $M - \Delta M$  with the momentum. The solid and dashed pair lines represent the tracks near the center ( $\eta \sim 0$ ) and near the end of the TPC ( $\eta \sim 1$ ). From the figure, it is shown that the PID capabilities of TOF detector is momentum range up to  $\sim 1.7(1.9)$  GeV/c for  $\pi \setminus K \setminus p$ , and up to  $\sim 2.6(3.1)$  GeV/c for  $(\pi + K) \setminus p$  for tracks near  $\eta \sim 0(1)$  [102].

# Chapter 5

## Analysis Details

In this chapter, I discuss the analysis technique used for the determination of the first measurement of  $2^{nd}$  order off-diagonal cumulants of net-charge, net-proton and net-kaon multiplicity distributions at  $\sqrt{s_{NN}} = 7.7, 11.5, 14.5, 19.6, 27, 39, 62.4$  and 200 GeV in Au+Au collisions at RHIC. In STAR we studied the beam energy, centrality and acceptance dependence of diagonal and off-diagonal cumulants. In the event-by-event fluctuation analysis, it is necessary to suppress/minimize the background fluctuations arises from bad runs, finite detection efficiency, centrality determination and finite bin width. These effects and corrections for cumulants studies are discussed in the following sections. An overview of the analysis procedure is described in Fig. 5.1.

### 5.1 Data sets

The analyzed  $Au + Au$  data were collected in year 2010 (at  $\sqrt{s_{NN}} = 7.7, 11.5, 39, 62.4$  GeV), 2011 (at  $\sqrt{s_{NN}} = 19.6, 27$  GeV), and 2014 (at  $\sqrt{s_{NN}} = 14.5$  GeV) in the first phase of the Beam Energy Scan (BES) program at RHIC.

## Trigger

We used the minimum bias (MB) events. The requirement for these events is the coincidence of signals from the two zero degree calorimeters (ZDCs) [104] and the vertex position detectors (VPDs) [102]. The ZDCs are a hadronic calorimeters residing within a small solid angle at  $\pm 18$  m from the center of STAR detector and close to the beam direction (at  $\theta \leq 2$  mrad). The ZDCs only measure the energy of spectator neutrons [105].

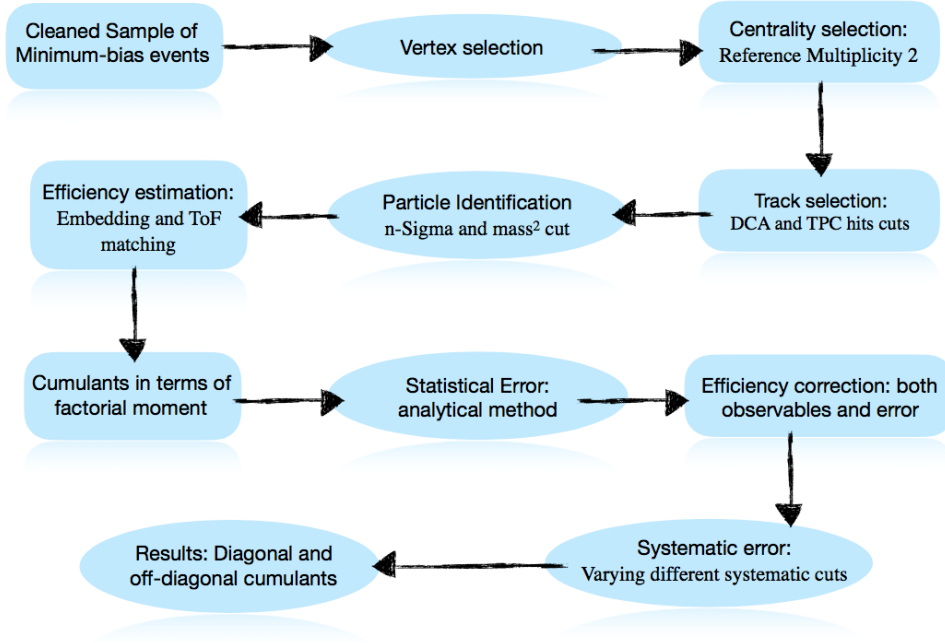


Figure 5.1: Analysis Flow-chart.

Real collisions are distinguished from the background by selecting events with ZDC coincidence from the two beam directions. This makes the ZDC suitable for event triggering and luminosity monitoring. Also, ZDCs are very useful towards the location of interaction vertices by using the time delay between the coincidences. The VPDs determine the vertex position along  $z$ -direction by measuring the time difference between the signals detected at its east and west positions 4.7. These two VPDs is around 5.7 m from the interaction point and covers the pseudorapidity range 4.24

$> |\eta| > 5.1$ . Coincidence signal in the east and west VPD detectors are used to select minimum bias events. Based on a coincidence of the signals from the ZDCs and VPDs, the following trigger id's are used in this analysis 5.1.

$\sqrt{s_{NN}}$ (GeV)	Production	Trigger Name	Trigger Id
7.7	AuAu7_Production	P10ih	290004, 290001
11.5	AuAu11_Production	P10ih	310014, 310004
14.5	production_15GeV_2014	P14ii	440005-6, 440015-16
19.6	AuAu19_Production	P11ik	340001,340011,340021
27	AuAu27_Production_2011	P11id	360001
39	AuAu39_Production	P10ik	280001
62.4	AuAu62_Production	P10id	270021,270011,270001
200	AuAu_200Production_2011	P11id	350043

Table 5.1: Trigger ID's of Beam Energy Scan phase-I

## 5.2 Event Selection

For this analysis, good event quality cuts were used for each dataset. The primary vertex was selected along the longitudinal direction of the beam pipe with  $|V_z| < 30$  cm from the center of the TPC detector. The radius of the RHIC beam pipe is 3.95 cm. At lower energies, due to large beam emittance, fake events occur in  $Au+beam$  pipe or with other material interaction at large longitudinal direction. So to reject such events uniform acceptance,  $|V_r| = \sqrt{V_x^2 + V_y^2} < 2$  cm ( $< 1$  cm for 14.5 GeV) were used. Figures 5.2 and 5.5 display the  $V_z$  and  $V_r$  distributions for eight BES energies. At higher energies, the luminosity is always high. This can lead to pile-up problem. In order to suppress such pile-up events we apply an additional cut on the absolute difference between the  $z$ -vertex positions determined by two different detectors (TPC and VPD), *i.e.*  $|V_z(\text{VPD}) - V_z(\text{TPC})| < 3$  cm on higher energies  $\sqrt{s_{NN}} = 39, 62.4$  and 200 GeV. Additional pile-up events have been removed by taking correlation between the number of TPC tracks and number of TOF matched tracks as shown in Fig. 5.3. Events cuts are listed in Table 5.2. Extensive

run quality check were performed based on different track variable average  $\langle p_T \rangle$ ,  $\langle \eta \rangle$ ,  $\langle \phi \rangle$ ,  $\langle \text{Distance of closest approach (DCA)} \rangle$  and similarly on different event variables, average reference multiplicity, average number of primary tracks. The bad run rejection was based on  $3\sigma$  cuts on run-number by run-number distributions of the above average variables as shown in Figure 5.4.

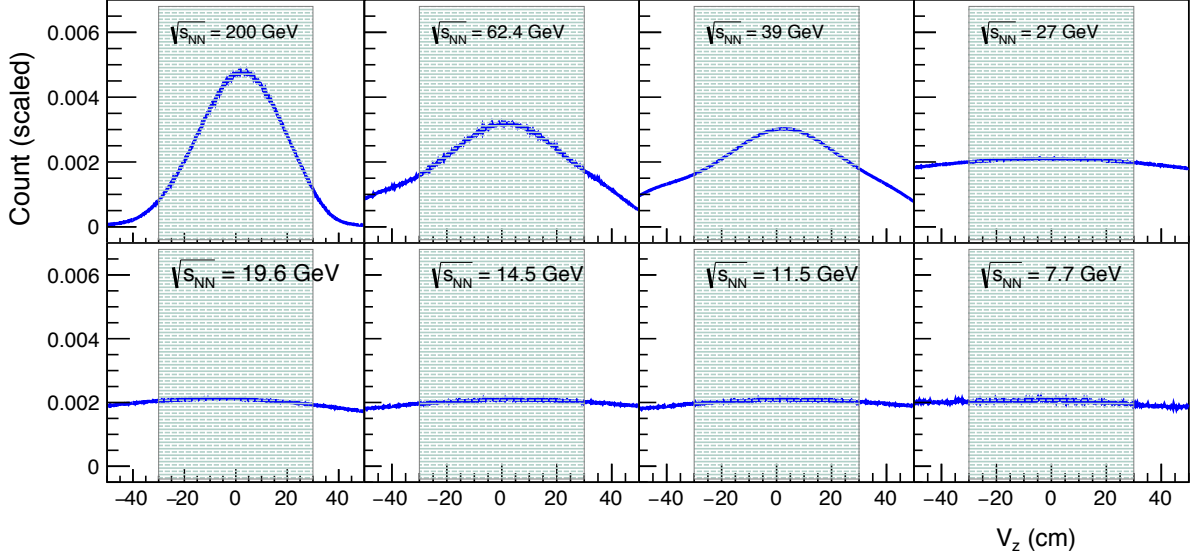


Figure 5.2: Distribution of z-component of event vertex for eight different center-of-mass energies. Shaded portion represents the acceptance cuts used in this analysis.

$\sqrt{s_{NN}}$ GeV	$ V_z $ cm	$ V_r $ cm	$ V_z(VPD) - V_z(TPC) $ cm	No of events (M)
7.7	$< 30$	$< 2$	Nan	1.5
11.5	$< 30$	$< 2$	Nan	2.5
14.5	$< 30$	$< 1$ <sup>1</sup>	Nan	12.7
19.6	$< 30$	$< 2$	Nan	15.6
27	$< 30$	$< 2$	Nan	25.2
39	$< 30$	$< 2$	$< 3$	62.3
62.4	$< 30$	$< 2$	$< 3$	31.6
200	$< 30$	$< 2$	$< 3$	74

Pile up event cut:  $0.46 * nRefMult - 10 < nTOFMatch$

Table 5.2: Event selection cuts used in BES-I energies

<sup>1</sup> Shifted vertex cut  $\sqrt{V_x^2 + (V_y + 0.89)^2}$  used in 14.5 GeV

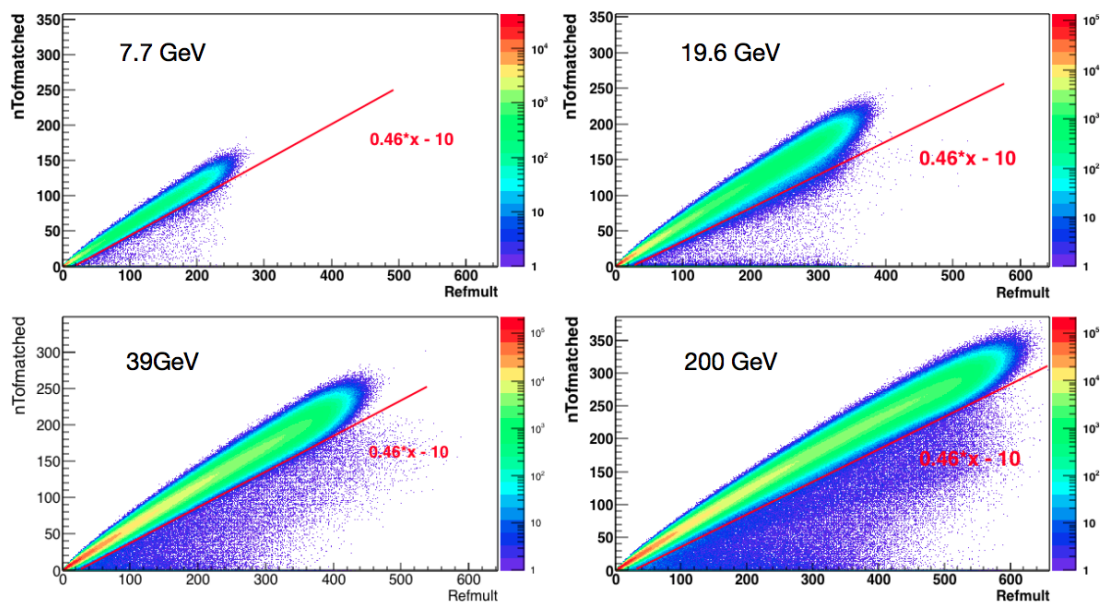


Figure 5.3: TOF match as a function of reference multiplicity. The red line corresponds to the pile-up rejection cut.

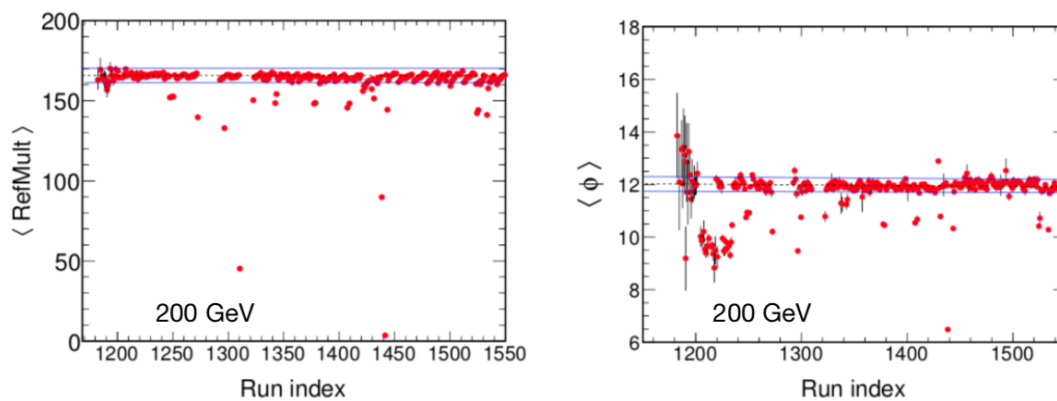


Figure 5.4: Run by Run QA for 200 GeV  $Au + Au$  collisions  $\langle \text{RefMult} \rangle$  and  $\langle \phi \rangle$ .

### 5.3 Track Quality Cuts

The charged particles are bend due to the presence of the 0.5T high magnetic field. The path of the charged particles are reconstructed using the Helix algorithm. To reduce the contamination from the secondary particles, we only selected tracks with a distance of closest approach (DCA) from the primary vertex less than 1 cm. Such a DCA cut suppresses contamination associated with weak decays from  $\Lambda^0$  hyperons. The track selection cuts for all eight BES energies are listed in Table 5.3.

Transverse momentum ( $p_T$ )	0.4 to 1.6 GeV/c
Pseudorapidity ( $\eta$ )	-0.5 to 0.5
nFitPoints	> 20
DCA	< 1 cm
Track quality cut	> 0.52
nhitsdedx	> 5

Table 5.3: Event selection cuts used in BES I energies

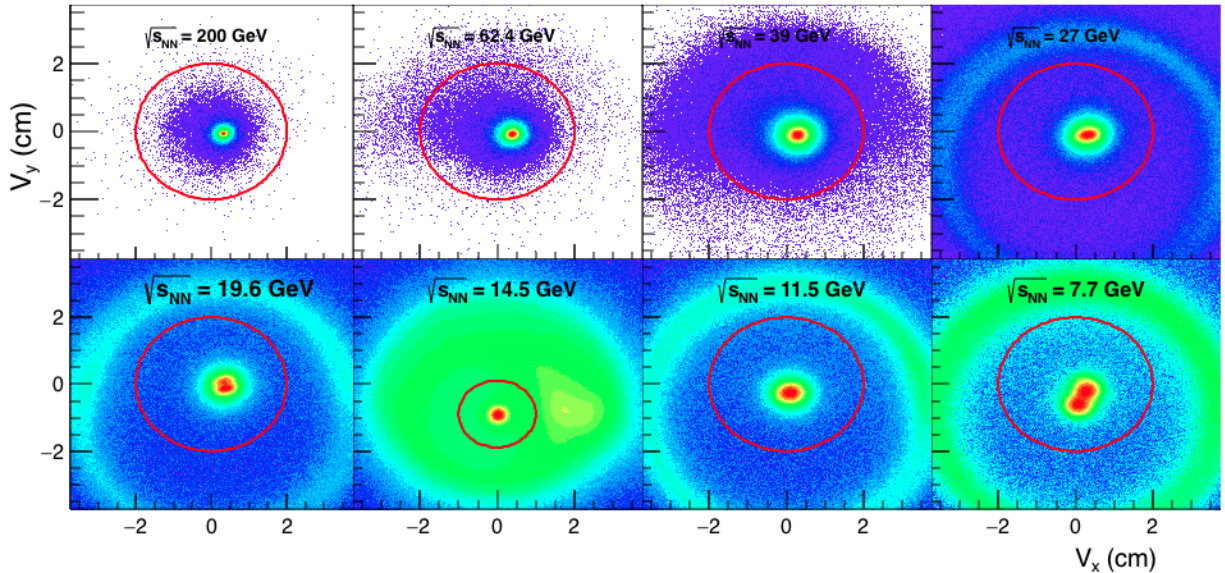


Figure 5.5: Distribution of transverse plane component of event vertex for different centre-of-mass energies.

A tracks travelling through the TPC detector can have maximum 45 hits. In this analysis, we used a minimum of 20 hits fit points for track fitting to avoid track splitting effect. To prevent multiple counting of split tracks, further requiring that the number of fit points is more than half of the number of total possible hit points for a track, i.e.  $n\text{HitsFit}/N\text{FitPoss} \geq 0.52$ . A common and uniform acceptance  $|\eta| < 0.5$ , and transverse momentum range  $0.4 < p_T < 1.6 \text{ GeV}/c$  is used to select charged particles, protons and kaons using both TPC and TOF detectors. Within this transverse momentum range, STAR has good identification capabilities for both protons and kaons.

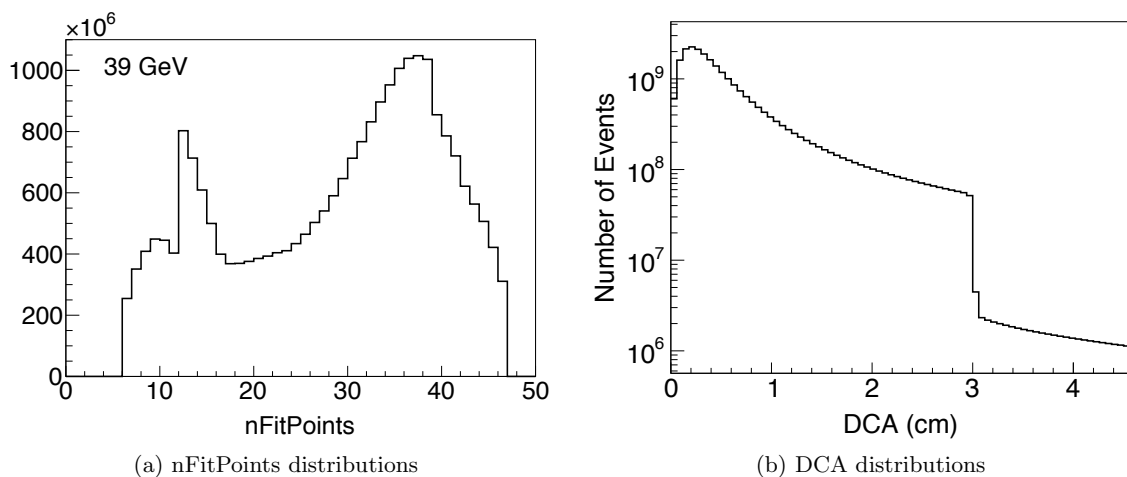


Figure 5.6: NFitsPoints and DCA distributions for Au+Au 39 GeV

## 5.4 Collision Centrality Selection

A nucleus is an extended object. According to collision geometry, several types of collisions can be defined. When the two colliding nuclei collide head-on, e.g., with a minimum impact parameter, defined as central collisions, whereas the peripheral collisions are defined when they interact glanc-

ing. The centrality of nucleus-nucleus collisions is characterized by different parameters, such as the impact parameter ( $b$ ), the number of participant nucleons ( $N_{part}$ ), and the number of binary collisions ( $N_{coll}$ ) 5.7.

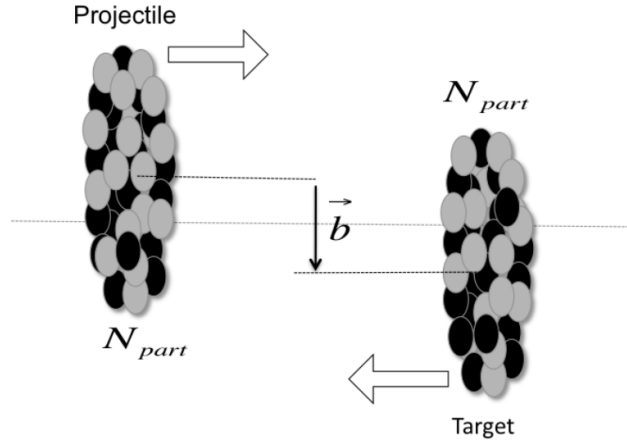


Figure 5.7: An illustration of the nucleus-nucleus collision.

One cannot measure  $N_{part}$ ,  $b$  or  $N_{coll}$  directly. However, it is possible to estimate these variables by measuring charged particle multiplicities  $N_{ch}$ . High multiplicity events correspond to central collisions, and low multiplicity events represent peripheral collisions. Schematically a charged particle multiplicity distribution for a set of minimum bias events is shown in Fig. 5.9, where top 5% high  $N_{ch}$  correspond to 0-5% centrality and so on. But these experimental observables, such as particle multiplicity, not only reflect the geometry of the collision, but also depend on physics processes. This indicates that the measured observables and impact parameter are not one-to-one correspond. With a fixed impact parameter,  $N_{ch}$  can fluctuate. So fixed  $N_{ch}$  does not correspond to a fixed geometry, but on average they are proportional to the collision geometry.

In STAR, the centrality selection is carried out by measuring the reference multiplicity in a given rapidity window, like  $|\eta| < 0.5$ ,  $0.5 < |\eta| < 1.0$ , etc. Due to the small number of charged particle track, vertex reconstruction becomes inefficient towards most peripheral events. To correct

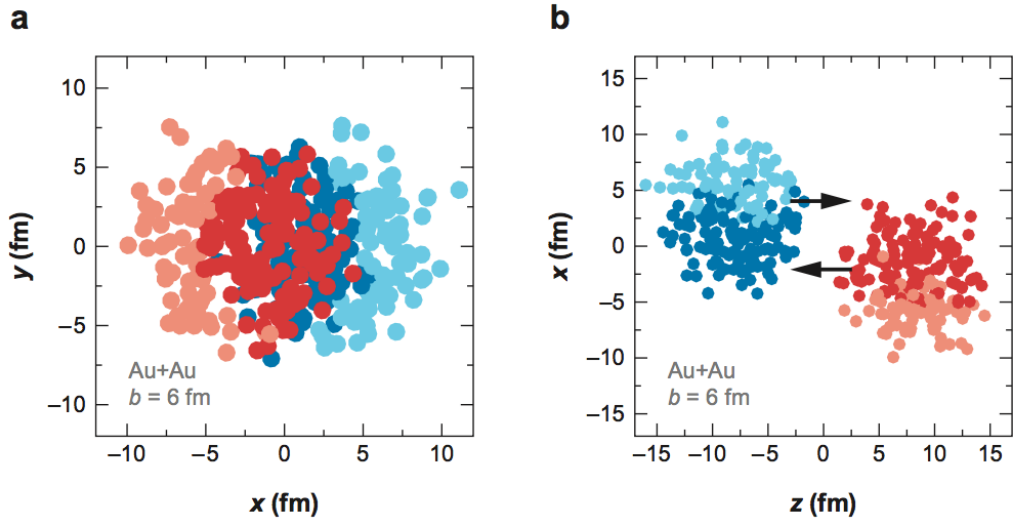


Figure 5.8: An illustration of a Glauber MC event for  $Au + Au$  collisions at  $\sqrt{s_{NN}} = 200$  GeV with impact parameter  $b = 6$  fm viewed (a) in the transverse plane and (b) along the beam axis. The nucleons are drawn with a radius  $\sqrt{\sigma_{NN}/\pi}/2$ . Participating nucleons ( $N_{part}$ ) are represented by darker disks and the lighter circle represents spectator. The figures are taken from [24].

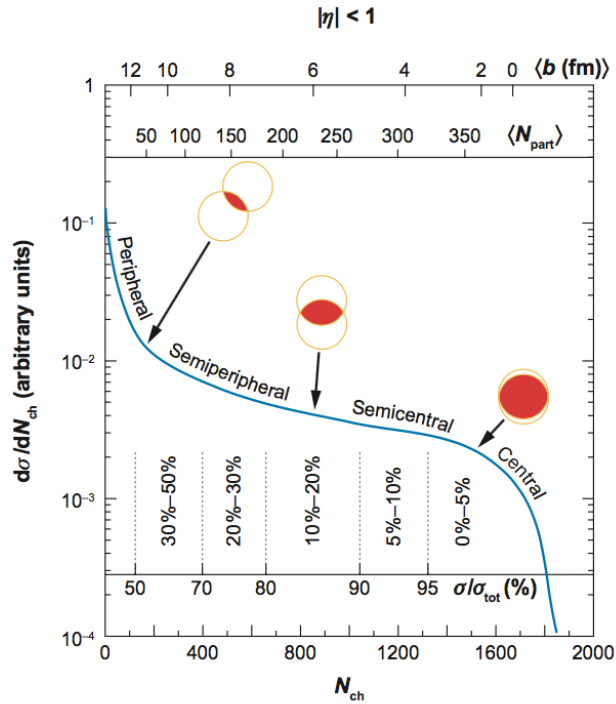


Figure 5.9: An illustrated example of the correlation of the final state observable total charged particle multiplicity  $N_{ch}$  with Glauber-calculated quantities ( $b$ ,  $N_{part}$ ). The figure is taken from [24].

this measured  $N_{ch}$  is compared with the simulated multiplicity density, which is calculated using the two-component model [106] and is given by:

$$\frac{dN_{ch}}{d\eta} = n_{pp} \left[ (1-x) \frac{N_{part}}{2} + x N_{coll} \right], \quad (5.1)$$

where  $n_{pp}$  is the average charged particle multiplicity in  $p+p$  collision per unit of pseudorapidity and  $x$  is the fraction of the produced charged particles from the hard component.  $N_{part}$  and  $N_{coll}$  are the number of participant nucleons and binary collisions, respectively, used in the Glauber Monte-Carlo simulations. In this model, a nucleus-nucleus collision is treated as a sequence of independent binary nucleon-nucleon collisions. An illustration of a Glauber Monte Carlo event for a single Au+Au collision is shown in Fig. 5.8 using impact parameter  $b = 6$  fm. Average quantities are then determined by simulating many A+B collisions as illustrated in Fig. 5.9. Experimentally, the centrality class is defined from the efficiency-uncorrected charged particle multiplicity coupled with Glauber model simulation as follows,

$$\frac{\int_{\infty}^{n_{c_1-c_2}} \frac{dN^{MC}}{dN_{ch}} dN_{ch}}{\int_{\infty}^0 \frac{dN^{MC}}{dN_{ch}} dN_{ch}} = \frac{N_{bin}}{N_{total}}, \quad (5.2)$$

where  $c_1, c_2$  represents the maximum and minimum cut of charge multiplicity ( $c_1 - c_2$  represents number of bins) at which the required percentage of total integral occurred.  $N_{bin}$  and  $N_{total}$  represent multiplicity in that particular bin and the entire multiplicity of the distribution. In this analysis, a similar method has been used. To determine centrality, we exclude the acceptance region to select charged particle multiplicity to suppress rid of the auto-correlation effect [107].

The auto-correlation effect is a background effect in the fluctuation analysis due to centrality selection. Traditionally, centrality selection in STAR experiment is done by the uncorrected charge particle multiplicity within  $|\eta| < 0.5$ . In this analysis, we select the particles within  $|\eta| < 0.5$  for PID [108]. Because same charged particles are used in both the analysis and the centrality selection, the particle distribution (or the cumulants value) will be affected by auto-correlation. To reduce this effect, we used different particles for centrality selection or select charged particles from another  $\eta$  region. In this analysis, a different  $\eta$  region  $0.5 < |\eta| < 1.0$  is used. The  $\eta$  vs  $p_T$  acceptance is shown in Fig. 5.10. We have selected particles within  $|\eta| < 0.5$  for analysis using both TPC and TOF detector and used charged particle multiplicities in TPC detector within  $0.5 < |\eta| < 1.0$  for centrality selection. This centrality definition is called Reference Multiplicity-2 or shortly "RefMult2". In STAR, run-by-run  $V_z$  correction are done for the RefMult2 [109].

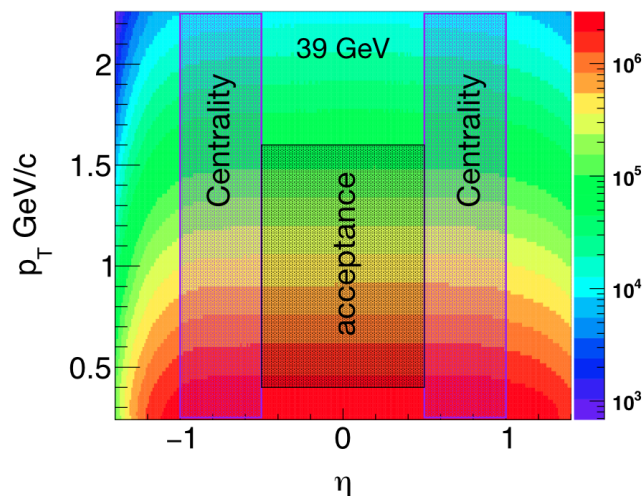


Figure 5.10:  $\eta$  vs  $p_T$  distributions for Au+Au 39 GeV

The RefMult2 distributions for  $Au + Au$  collisions at all eight BES energies are shown in Figure 5.11. The different colour bins correspond to different centrality classes with 10% or 5% centrality window. The centrality cut boundaries using RefMult2 definition are listed in Table 5.4.

For example, to select 0-5% centrality for 200 GeV, we use  $\text{Refmult2} > 453$  events. Similarly,  $181 < \text{Refmult2} \leq 268$  for 20-30% centrality.

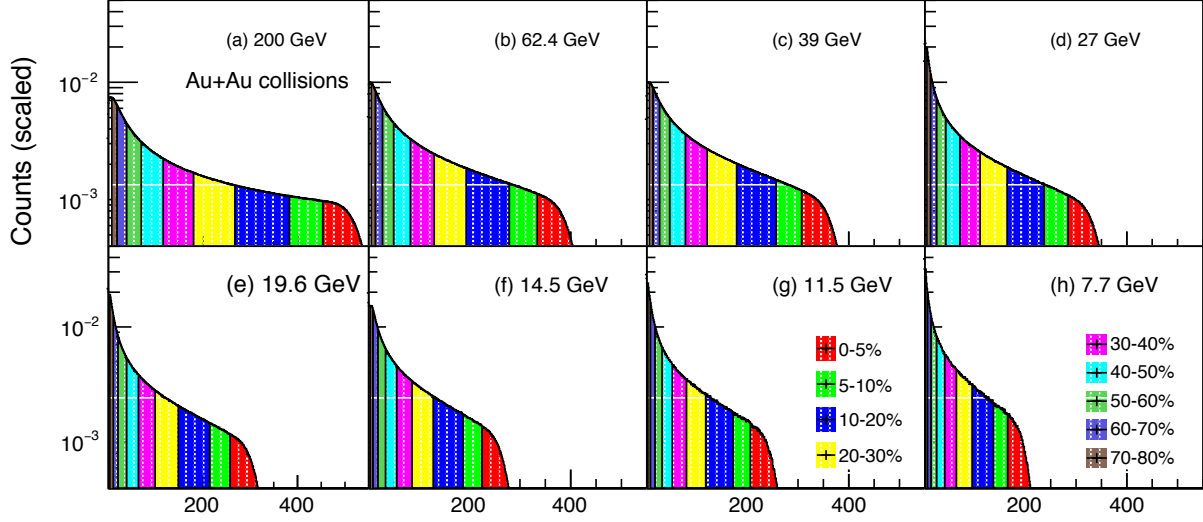


Figure 5.11: Efficiency uncorrected reference multiplicity ( $\text{Refmult2}$ ) distributions for  $Au + Au$  collisions at eight different BES energies.

$\sqrt{s_{NN}}$ (GeV)	0-5%	5-10%	10-20%	20-30%	30-40%	40-50%	50-60%	60-70%	70-80%
200	453	383	268	181	117	71	40	20	9
62.4	334	279	194	131	84	51	29	15	7
39	307	257	179	121	78	47	27	14	7
27	284	237	164	111	71	43	25	13	6
19.6	258	215	149	100	65	40	22	12	5
14.5	225	188	129	87	57	35	20	10	5
11.5	206	172	118	80	52	32	18	9	4
7.7	165	137	95	64	41	25	14	7	3

Table 5.4:  $\text{Refmult2}$  cuts for centrality selection used in BES-I energies

## 5.5 Particle Identification

Long-lived particles, such as protons (mean lifetime  $\sim 10^{31} - 10^{33}$  years), pions (mean lifetime  $\sim 2.6 \times 10^{-8} s$ ) and kaons ( $\sim 1.2 \times 10^{-8} s$ ), are identified by their mass and the way they interact.

Each type of particle has its signature in the detector. For example, if a particle is only detected in the electromagnetic calorimeter, it is most probable that the detected particle is a photon.

Figure 5.12 shows illustration of traditional particle physics experiment component layout.

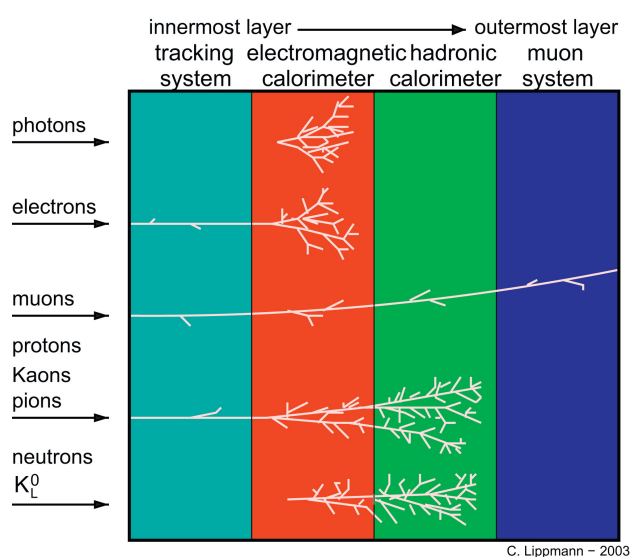


Figure 5.12: Illustration of traditional particle physics experiment components [110].

The STAR detector is capable of excellent particle identification over a large uniform acceptance at mid-pseudorapidity and with full azimuthal coverage. For proton, kaon, and pion identification; energy loss ( $dE/dx$ ) mechanism of the Time Projection Chamber (TPC) and mass-square cut from Time of Flight (TOF) detector are used. TPC measures ionization energy loss of the charged particle while travelling through the gas volume. TPC operates on a constant magnetic field, so the charge particle momentum is estimated from their track curvature. From this particle species momentum vs energy loss curve, we can identify particles by comparing with the Bichsel curves, which is an extension of the Bethe-Bloch formula. The performance of different particle

identification methods is explained in Reference [111]. Figure 5.13 shows the ionization energy loss ( $dE/dx$ ) for beam energies  $\sqrt{s_{NN}} = 7.7, 11.5, 14.5, 19.6, 27, 39, 62.4$  and  $200$  GeV in  $Au + Au$  collisions. The  $dE/dx$  curve provide a good particle identification up to  $p_T \leq 0.4$  GeV/c for proton/pion and  $p_T \leq 0.8$  GeV/c for protons, respectively. The Bichsel functions, as described in section 4.2.1, are used to determine the  $n\sigma$  values for each particle species. The quantity  $n\sigma$  is defined as,

$$n\sigma = \frac{1}{R} \times \frac{dE/dx_{measured}}{dE/dx_{theory}}, \quad (5.3)$$

where  $dE/dx$  is the specific ionization energy loss per unit path length, and  $R$  is the energy loss resolution. In this cumulant analysis, a cut of  $|n\sigma_{particle}| < 2.0$  was used for identification of charged protons and kaons. The TOF system is mainly used to enrich the particle identification of charged particles over a broader range of momentum. Particle identification using the TOF detector is made by measuring the velocity and mass of a track. The TOF system gives the flight time, and the TPC gives the momentum and path length. The inverse velocity and associated mass are calculated from,

$$\frac{1}{\beta} = \frac{c\Delta t}{s}, \quad (5.4)$$

and,

$$m^2 = p^2 \left( \left( \frac{1}{\beta} \right)^2 - 1 \right), \quad (5.5)$$

where,

p = momentum,

$\Delta t$  = flight time,

$s$  = total path length,

$c$  = velocity of light.

The combined information of the TPC and TOF detectors provides a good particle identification in the momentum range 0.2 to 1.6 GeV/c for kaons and pions, and in the range 0.4 to 2.0 GeV/c for protons [102]. So, for this correlation analysis, we used the common transverse momentum acceptance range  $0.4 < p_T < 1.6$  GeV/c for particle identification. The cuts for protons, kaons, and charge particles identification are listed in Table 5.5. Within this kinematic range, the purities of  $K^\pm$  and  $p(\bar{p})$  are found to be 98% and 99%, respectively [50, 53]. We also include the contamination effect in systematic uncertainties by varying different  $n\sigma$  cuts. In section 5.8.2, this will be discussed.

Particles	TPC	TPC + TOF
$p(\bar{p})$	$0.4 < p_T < 0.8$ (GeV/c) $ n\sigma_p  < 2$	$0.8 < p_T < 1.6$ (GeV/c) $0.6 < m^2 < 1.2$
$k^+(k^-)$	$ n\sigma_K  < 2,  n\sigma_\pi  > 2$	$0.4 < p_T < 1.6$ (GeV/c) $0.15 < m^2 < 0.4$
$Q^+(Q^-)$	$0.4 < p_T < 1.6$ (GeV/c)	

Table 5.5: Particle identification cuts used in this analysis.

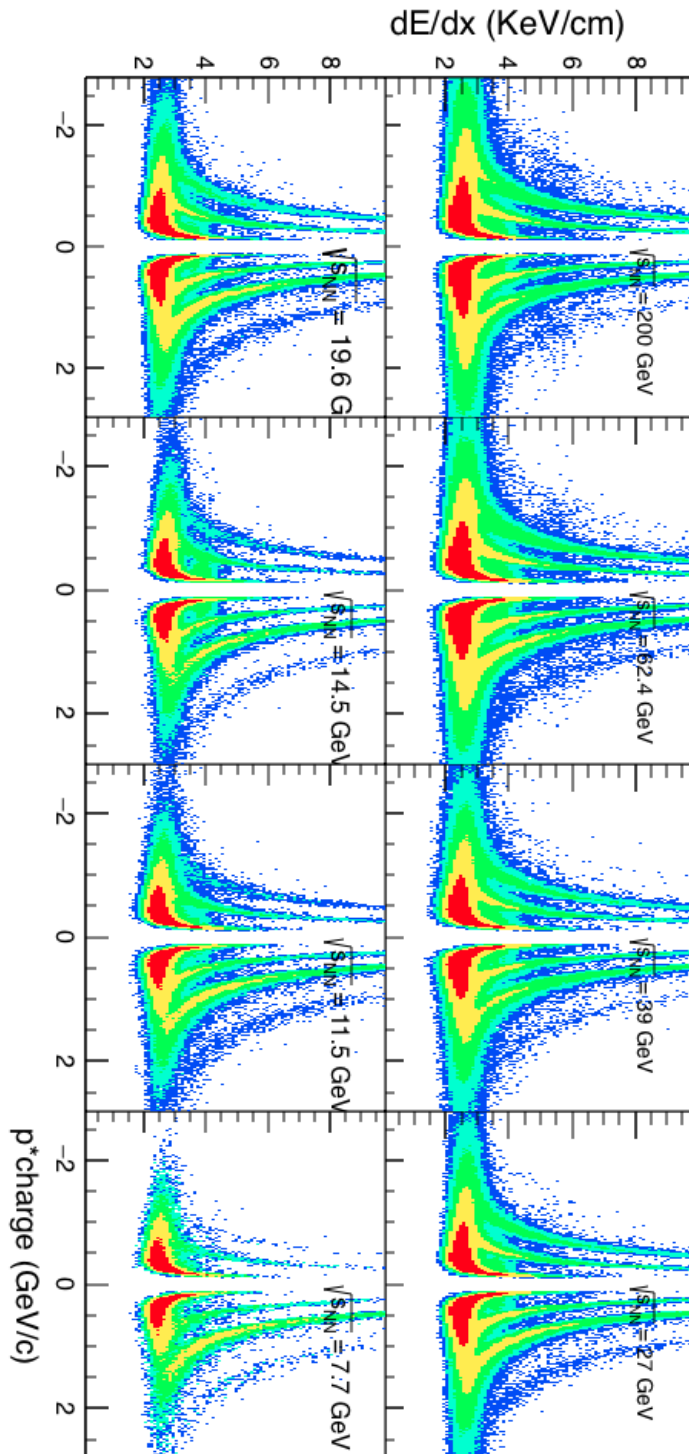


Figure 5.13: Track  $dE/dx$  vs momentum distribution for different centre-of-mass energies.

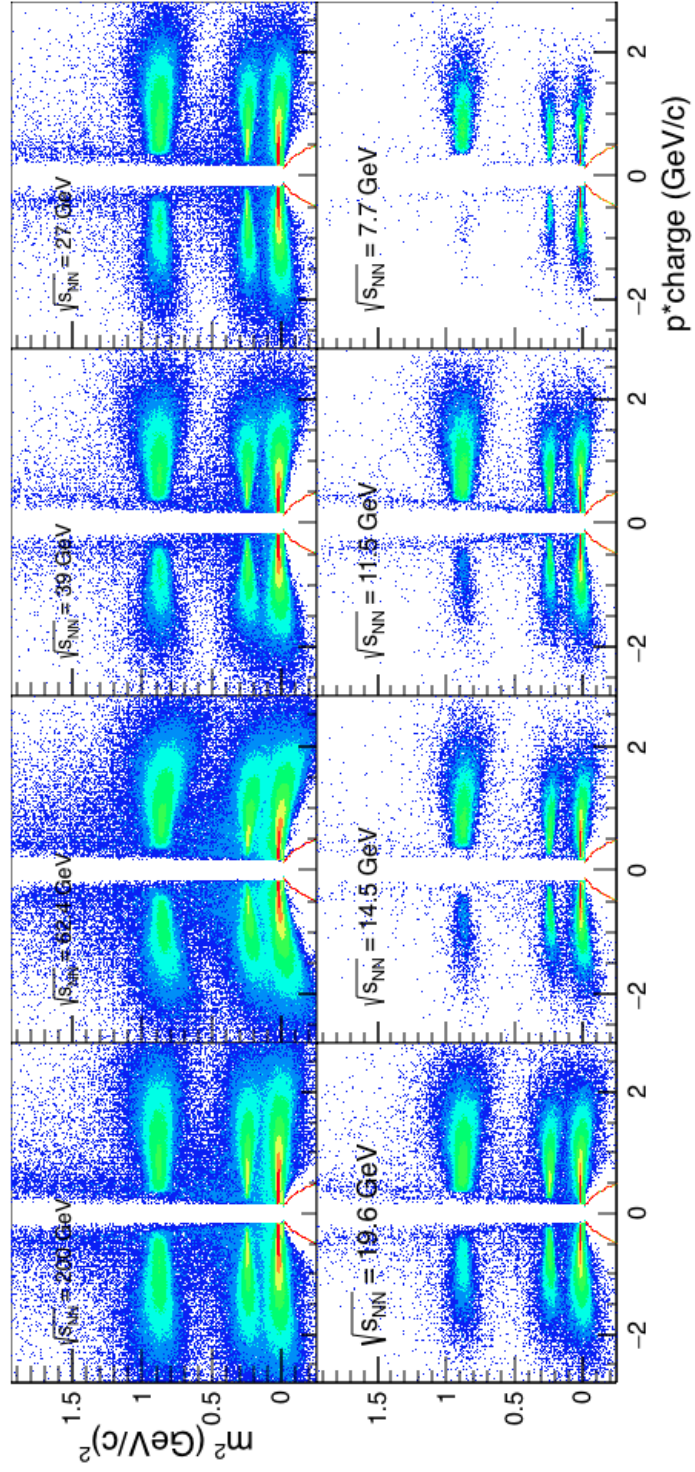


Figure 5.14: TOF Mass square vs momentum distribution for different center-of-mass energies.

## 5.6 Centrality Bin width Correction

In fluctuation analyses, we present the results for wider centrality bins, like 0-5% or 0-10% bins for better statistical accuracy. Such wide centrality bins cause additional background fluctuation due to significant variation in event-by-event initial collision geometry. Centrality Bin Width Correction (CBWC) is done to suppress the artificial fluctuation due to wide centrality bins. The finite centrality effect can be reduced by taking smaller centrality bins. For better centrality determination and better statistical accuracy, we used wider centrality bins. But this wider centrality bin can introduce the so-called Centrality Bin Width Effect (CBWE) [107], an artificial centrality width dependence on cumulants. This effect is more towards lower energies and higher order cumulant. For lower order cumulants this effect is small/negligible as shown in Fig. 5.15. Here, blue dotted points represent the covariance in each RefMult2 bin, whereas the red circle and black diamond represent the covariance values with and without CBWC for 9 different centralities (0-5%,5-10%,10-20%,.....,70-80%). For higher order, the difference between with and without CBW correction is clearly visible and the bin width corrected results are closer to those obtained with smaller bin results [54].

To suppress the centrality bin width effect in a wide centrality bin, we calculate the cumulants for each finer bins in a given centrality class then weighted to get the final cumulants, according to:

$$X = \frac{\sum_{i=N_1}^{N_2} n_i X_i}{\sum_{i=N_1}^{N_2} n_i}, \quad (5.6)$$

where  $X_i$  represents the cumulants or cumulants ratios of  $i^{th}$  multiplicity bin,  $\sum_i n_i$  is the total

number of events in the given centrality bin. Figure 5.16 show that with bin-width correction, observables are independent of the chosen centrality bin width and lie on top of each other. This correction has been implemented throughout this analysis.

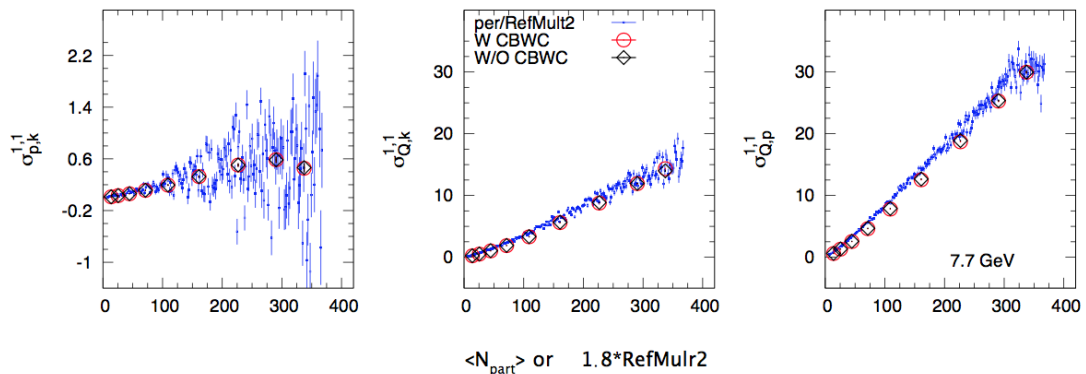


Figure 5.15: Diagonal and off-diagonal cumulants for 5% (0-5%,.....75-80%) and 10% (0-10%,.....70-80%) centrality bins with CBWC correction for Au+Au collisions at  $\sqrt{s_{NN}} = 7.7$  GeV.

## 5.7 Efficiency correction

Every detector has finite efficiency. In the STAR experiment also, all detectors have finite efficiencies for tracking particles and event identification. To obtain proper results efficiency correction needs to be done on the observables. There are several factors contributes to a finite detector efficiency, for example, tracking inefficiency, uncertainties due to acceptance, uncertainties in measuring momentum, vertex resolution inefficiency, etc. In an event-by-event analysis, to measure all these uncertainties separately and correct for each source, is a difficult task. Besides, efficiencies due to different sources, are not additive. He we estimate the detector efficiencies and correct the observables for its effect to the best extent possible.

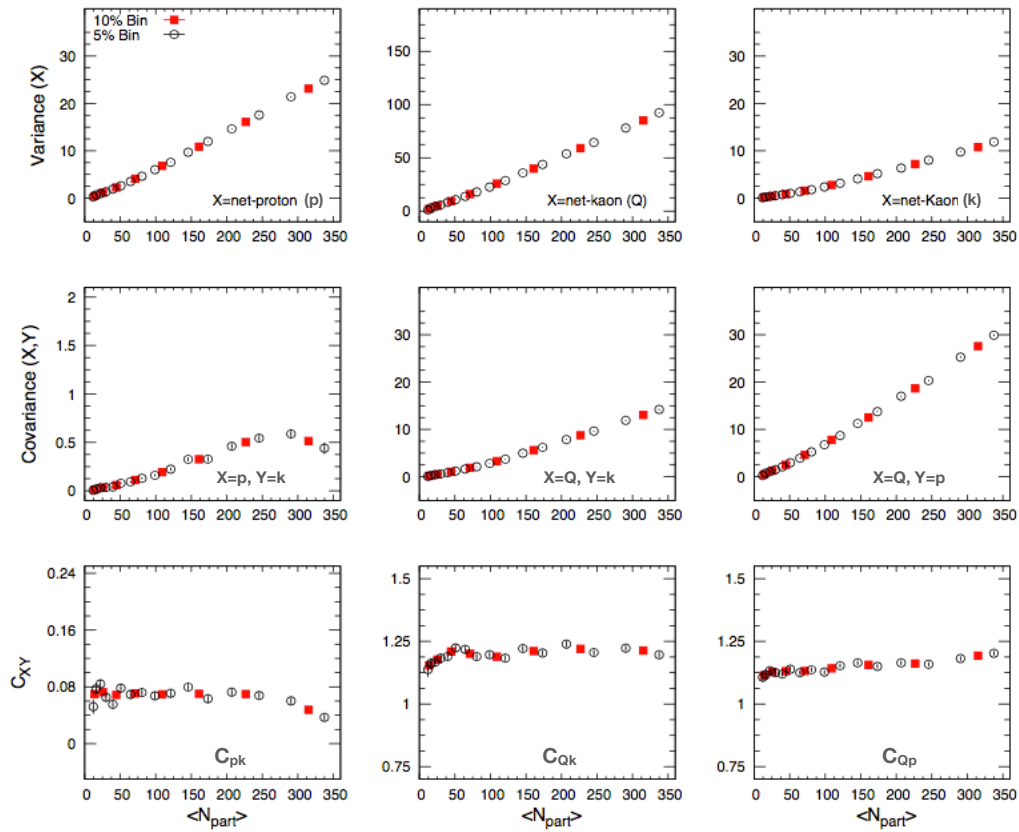


Figure 5.16: Diagonal and off-diagonal cumulants for 5% (0-5%,.....75-80%) and 10% (0-10%,.....70-80%) centrality bins with CBWC correction for Au+Au collisions at  $\sqrt{s_{NN}} = 7.7$  GeV.

### 5.7.1 Efficiency Correction for moments/cumulants

We perform efficiency correction in two steps: first, we determine the numerical values of the efficiency using detector simulation and then we use the numerical algebra based on binomial detector response [90] to correct the measurements of individual cumulants. Let us consider  $P(N)$  is the e-by-e true distribution of a particle. Now the distribution of detected particles ( $p(n)$ ) after passing through a detector with efficiency  $\varepsilon$  is given by equation 5.7. This is similar to toss many coins together.

$$p(n) = \sum_{N=n}^{\infty} \frac{N!}{n!(N-n)!} (\varepsilon)^n (1-\varepsilon)^{N-n} P(N) = \sum_{N=n}^{\infty} B(n|N, \varepsilon) P(N), \quad (5.7)$$

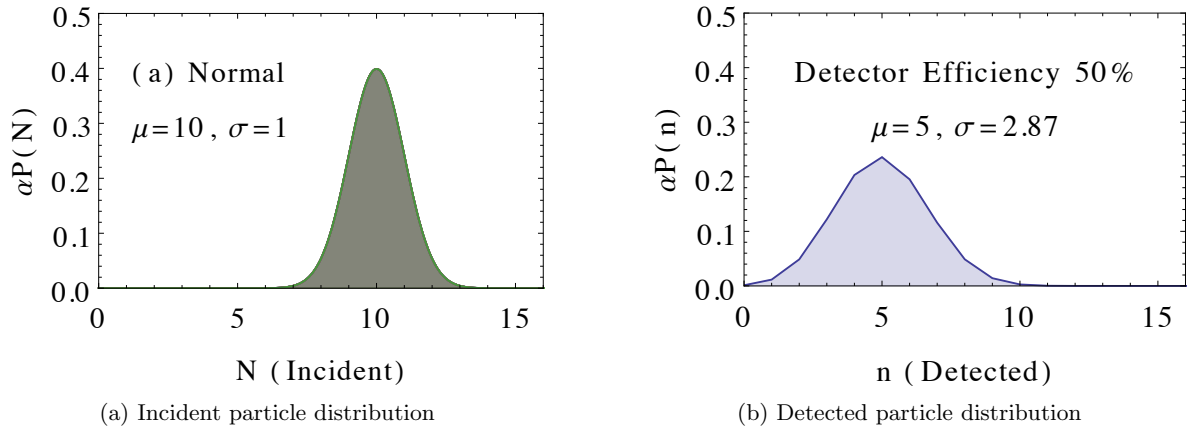


Figure 5.17: An illustrated example of incident and detected particle distribution with 50% detection efficiency. The incident particles are distributed according normal distribution.

An illustration is shown in Fig. 5.17, where the particle is generated ( $N$ ) according to normal distribution with mean ( $\mu$ ) and width ( $2\sigma$ ) 10 and 2 respectively as shown in Fig. 5.17a. Then the detected particle ( $n$ ) distribution with 50% detection efficiency looks like Fig. 5.17b, where the mean is shifted to 5 and width become 5.74. From equation 5.7, we can get the following relation

between detected ( $\mu_i^{obs}$ ) particle moments and incident or true ( $\mu_i^{inc}$ ) particles moment:

$$\begin{aligned}
\mu_1^{obs} &= \varepsilon \mu_1^{inc}, \\
\mu_2^{obs} &= \varepsilon^2 \mu_2^{inc} + \varepsilon(1 - \varepsilon) \mu_1^{inc}, \\
\mu_3^{obs} &= \varepsilon^3 \mu_3^{inc} + 3\varepsilon^2(1 - \varepsilon) \mu_2^{inc} + \varepsilon(1 - 2\varepsilon) \mu_1^{inc}.
\end{aligned} \tag{5.8}$$

Now in terms of moment, there is no easy and clear pattern to couple the detected and incident particle distributions. But expressing the distributions in terms of the factorial moment we can easily obtain useful relation between detected ( $f_i^{obs}$ ) and true ( $f_i^{inc}$ ) factorial moment as follows:

$$\begin{aligned}
f_1^{obs} &= \varepsilon f_1^{inc}, \\
f_2^{obs} &= \varepsilon^2 f_2^{inc}, \\
f_3^{obs} &= \varepsilon^3 f_3^{inc}, \\
f_n^{obs} &= \varepsilon^n f_n^{inc}.
\end{aligned} \tag{5.9}$$

Here,  $f_n^{obs}$  is  $n$ -th order efficiency uncorrected factorial moment and  $f_n^{inc}$  is  $n$ -th order efficiency corrected factorial moment. We denote all observed (or efficiency uncorrected) quantities in a small alphabet (like  $f_n^{obs}$  as  $f_n$ ) and all incident or efficiency corrected observables in capital alphabet (like  $f_n^{inc}$  as  $F_n$ ).

For net cumulant analysis,  $n$  is the difference between positive and negative particle — for example, net-proton  $n = n_p - n_{\bar{p}}$ . Here the distribution is a joint probability distribution of the number of protons ( $n_p$ ) and anti-protons ( $n_{\bar{p}}$ ). The relation between measured and actual joint

probability distribution of net-proton ( $p(n_p, n_{\bar{p}})$ ) is,

$$p(n_p, n_{\bar{p}}) = \sum_{N_p=n_p}^{\infty} \sum_{N_{\bar{p}}=n_{\bar{p}}}^{\infty} B(n_p|N_p, \varepsilon_p) B(n_{\bar{p}}|N_{\bar{p}}, \varepsilon_{\bar{p}}) P(N_p, N_{\bar{p}}). \quad (5.10)$$

Similarly, for the mixed cumulant case, the equation become,

$$p(n_p, n_{\bar{p}}, n_{k_+}, n_{k_-}) = \sum_{N_p=n_p}^{\infty} \sum_{N_{\bar{p}}=n_{\bar{p}}}^{\infty} \sum_{N_{k_+}=n_{k_+}}^{\infty} \sum_{N_{k_-}=n_{k_-}}^{\infty} B(n_p|N_p, \varepsilon_p) B(n_{\bar{p}}|N_{\bar{p}}, \varepsilon_{\bar{p}}) B(n_{k_+}|N_{k_+}, \varepsilon_{k_+}) B(n_{k_-}|N_{k_-}, \varepsilon_{k_-}) P(N_p, N_{\bar{p}}, N_{k_+}, N_{k_-}), \quad (5.11)$$

where  $\varepsilon_p, \varepsilon_{\bar{p}}, \varepsilon_{k_+}, \varepsilon_{k_-}$  are the efficiency of proton, anti-proton, kaon+ and kaon-, respectively.

In terms of factorial moment,

$$F_{N_p, N_{\bar{p}}, N_{k_+}, N_{k_-}}^{s,t,u,v} = \frac{f_{n_p, n_{\bar{p}}, n_{k_+}, n_{k_-}}^{s,t,u,v}}{\varepsilon_p^s \varepsilon_{\bar{p}}^t \varepsilon_{k_+}^u \varepsilon_{k_-}^v}. \quad (5.12)$$

In this analysis, two  $p_T$  bin efficiency were used. Then Equation 5.12 can be written in a more deferential way for mixed factorial moments as follows:

$$F_{N_{(p,1)}, N_{(p,2)}, N_{(\bar{p},1)}, N_{(\bar{p},2)}, N_{(k_+,1)}, N_{(k_+,2)}, N_{(k_-,1)}, N_{(k_-,2)}}^{s,t,u,v,w,x,y,z} = \frac{f_{n_{(p,1)}, n_{(p,2)}, n_{(\bar{p},1)}, n_{(\bar{p},2)}, n_{(k_+,1)}, n_{(k_+,2)}, n_{(k_-,1)}, n_{(k_-,2)}}^{s,t,u,v,w,x,y,z}}{\varepsilon_{(p,1)}^s, \varepsilon_{(p,2)}^t, \varepsilon_{(\bar{p},1)}^u, \varepsilon_{(\bar{p},2)}^v, \varepsilon_{(k_+,1)}^w, \varepsilon_{(k_+,2)}^x, \varepsilon_{(k_-,1)}^y, \varepsilon_{(k_-,2)}^z}, \quad (5.13)$$

where suffix  $p, 1$  and  $p, 2$  represents identified protons in bin-1 and bin-2 respectively. Now the

efficiency corrected expression regarding the factorial moment of  $2^{nd}$ -order diagonal cumulant with two  $p_T$  bin positive/negative separate efficiency is [112],

$$\begin{aligned}
C_2 = & ((f_{1000}/e_1 + f_{0100}/e_2) + (f_{2000}/e_1^2 + f_{1100}/e_1e_2 + f_{1100}/e_1e_2 \\
& + f_{0200}/e_2^2) - (f_{1000}/e_1 + f_{0100}/e_2)^2) - 2((f_{1010}/e_1e_3 + f_{1001}/e_1e_4) \\
& + f_{0110}/e_2e_3 + f_{0101}/e_2e_4) - (f_{1000}/e_1 + f_{0100}/e_2)(f_{0010}/e_3 + f_{0001}/e_4) \\
& + ((f_{0010}/e_3 + f_{0001}/e_4) + (f_{0020}/e_3^2 + f_{0011}/e_3e_4 + f_{0011}/e_3e_4 \\
& + f_{0002}/e_4^2) - (f_{0010}/e_3 + f_{0001}/e_4)^2), \tag{5.14}
\end{aligned}$$

where  $[s, t, u, v]$  in  $f_{stuv}$  represents the order of the factorial moment and  $e_i$  represent the efficiency of  $i$ -th species. Similarly, the  $2^{nd}$  order off-diagonal cumulants ( $C_{1,1}$ ) can be expressed in terms of eight variable factorial moment  $f_{stuvwxyz}$  (or  $f_{n_{(p,1)}^{s,t,u,v,w,x,y,z}, n_{(p,2)}^{s,t,u,v,w,x,y,z}, n_{(\bar{p},1)}^{s,t,u,v,w,x,y,z}, n_{(\bar{p},2)}^{s,t,u,v,w,x,y,z}, n_{(k^+,1)}^{s,t,u,v,w,x,y,z}, n_{(k^+,2)}^{s,t,u,v,w,x,y,z}, n_{(k^-,1)}^{s,t,u,v,w,x,y,z}, n_{(k^-,2)}^{s,t,u,v,w,x,y,z}}$ ).

### 5.7.2 Efficiency estimation for protons and kaons

In the STAR experiment, the TPC tracking efficiency is estimated by embedding Monte Carlo (MC) tracks the real events. It can then calculated as  $\varepsilon = N_{reconstructed}/N_{primary}$ . The embedding  $p_T$  dependence efficiency for identified charge particle is shown in Figure. 5.19. The Flowchart of TPC and TOF matching efficiency estimation procedure as follows:

- **A:** MC tracks of charge particles ( $\pi^\pm, k^\pm, p, \bar{p}$ ) from the primary vertex,
- **B:** reconstructed tracks coming from the primary vertex and having associated MC track,
- **C:** B + matched with TOF hit,
- TPC tracking efficiency = B/A [Figure 5.18],

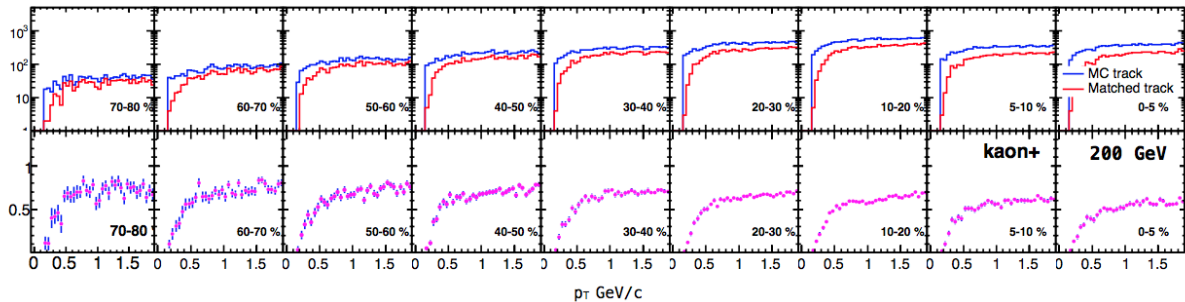


Figure 5.18: Top: Number of MC tracks and matched pairs for positive kaons in 0-5% central  $Au + Au$  collisions at  $\sqrt{s_{NN}} = 200$  GeV; Bottom: estimated pair efficiency vs  $p_T$ .

- TOF matching efficiency =  $C/B$  [Figure 5.20],
- TPC track reconstruction + TOF matching efficiency =  $C/A$  [Figure 5.21],

In our final calculation of the cumulants, we used  $p_T$  averaged efficiencies [5.25]. These are calculated based on:

$$\langle \varepsilon \rangle = \frac{\int_a^b \varepsilon'(p_T) f(p_T) p_T dp_T}{\int_a^b f(p_T) p_T dp_T}, \quad (5.15)$$

where  $\varepsilon'(p_T)$  is the  $p_T$  dependence efficiency with the same track cuts as used in the data analysis and  $f(p_T)$  is the efficiency corrected transverse momentum spectra for  $p, \bar{p}, k^+, k^-, \pi^+, \text{ and } \pi^-$  [113, 114]. (a,b) is the transverse momentum range listed in table 5.5. For proton, at lower  $p_T$  range  $0.4 < p_T < 0.8$  GeV/c TPC is used, and at higher transverse momentum range  $0.8 < p_T < 1.6$  GeV/c, both TPC and TOF used. Similarly, for kaons only one  $p_T$  bin efficiency is used (TPC+TOF) at higher transverse momentum range ( $0.4 < p_T < 1.6$  GeV/c).

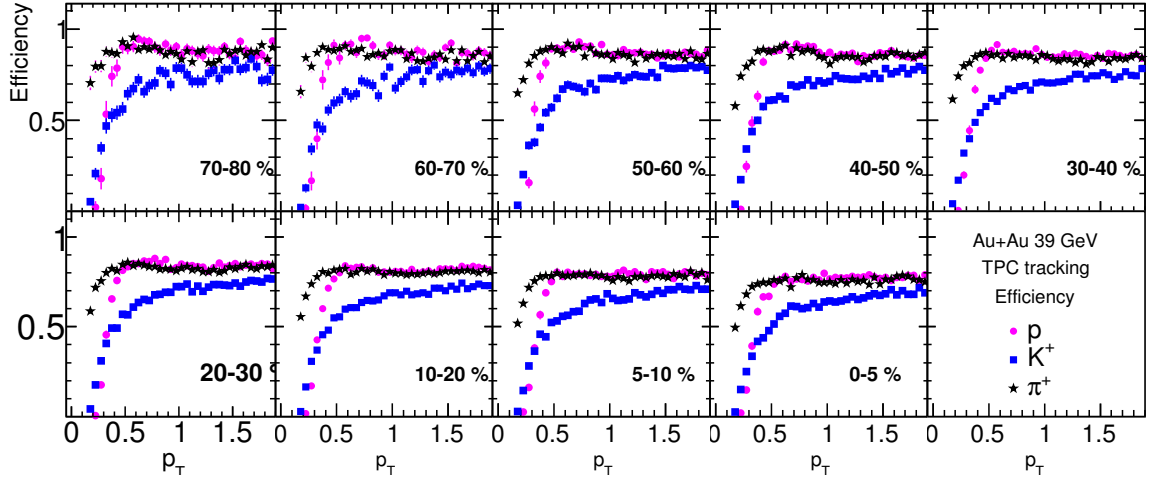


Figure 5.19:  $p_T$  dependence TPC tracking efficiencies for  $\pi^+$ ,  $k^+$ ,  $p$  at  $Au + Au$  39 GeV.

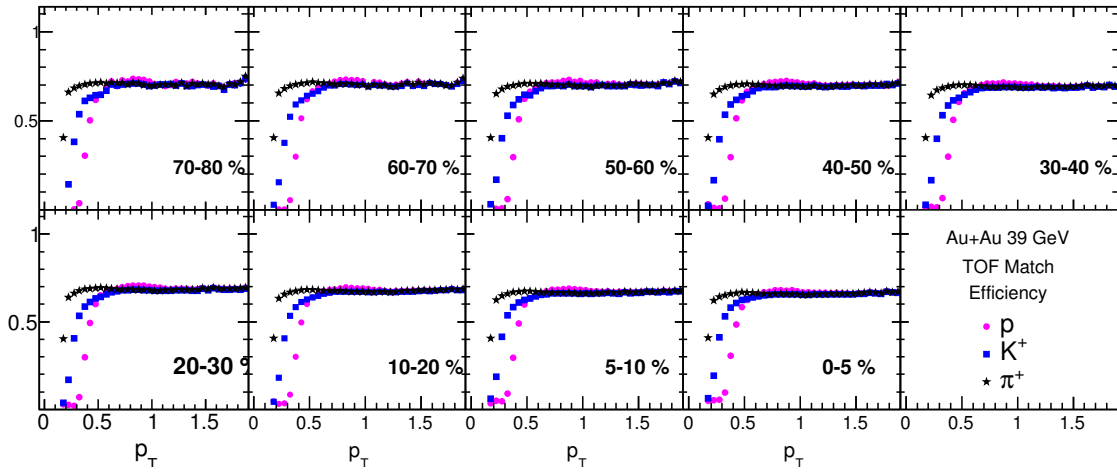


Figure 5.20:  $p_T$  dependence TOF matching efficiencies for  $\pi^+$ ,  $k^+$ ,  $p$  at  $Au + Au$  39 GeV.

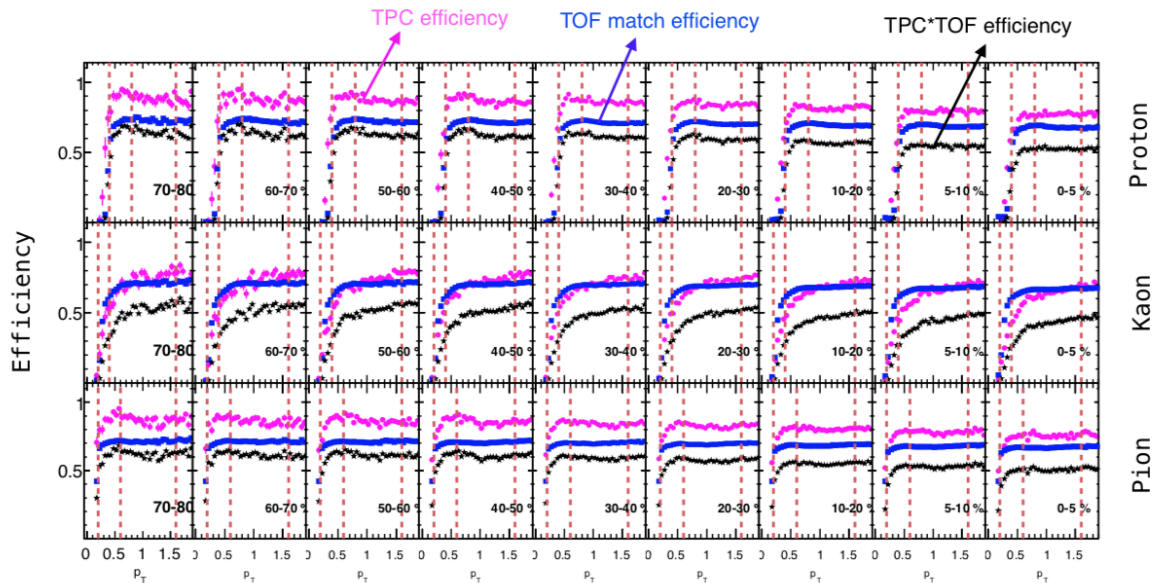


Figure 5.21:  $p_T$  dependence TPC tracking, TOF matching and combined efficiencies for  $\pi^+$ ,  $k^+$ ,  $p$  at Au+Au 39 GeV.

### 5.7.3 Efficiency estimation for $Q^+$ and $Q^-$

For charge particle selection, we have only used the TPC detector. So, for charge particle efficiency estimation we have used only embedding Monte Carlo tracks in real events. It is assumed that the total positive charge particles are a collection of  $\pi^+$ ,  $k^+$  and  $p$  and the total negative charge particle is a collection of their antiparticles. So the weighing for total charge particle is done as follows

$$w_p + w_{k^+} + w_{\pi^+} = 1, \quad (5.16)$$

where  $w_p$  is the weighted of proton in total positive charge (assuming that  $p + k^+ + \pi^+ = Q^+$ ).

The differential and average charge particle efficiency can be estimated based on the following expressions

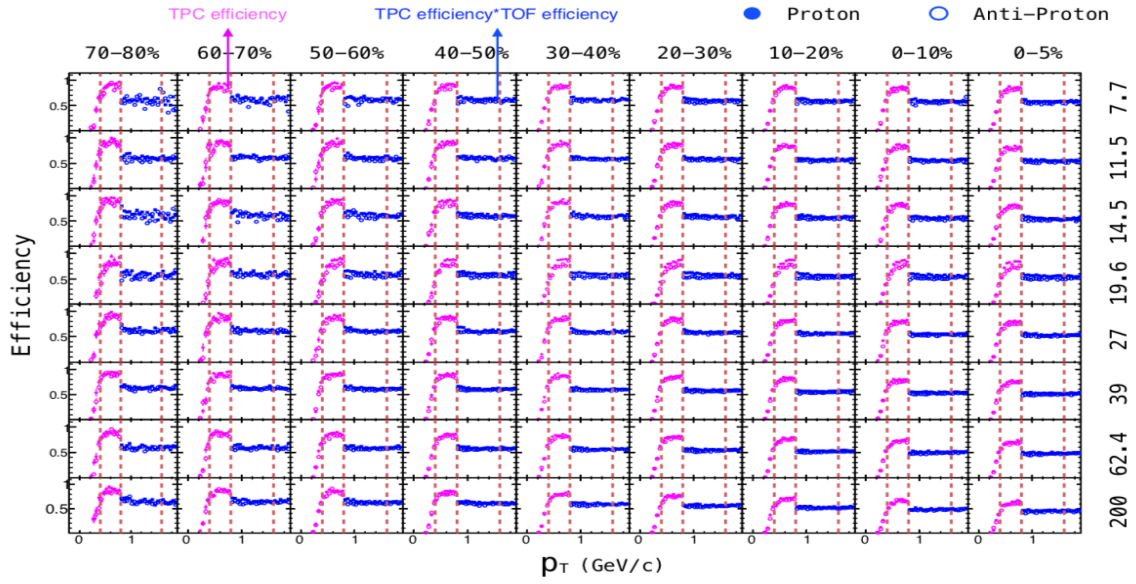


Figure 5.22:  $p_T$  dependence  $p$  and  $\bar{p}$  efficiencies

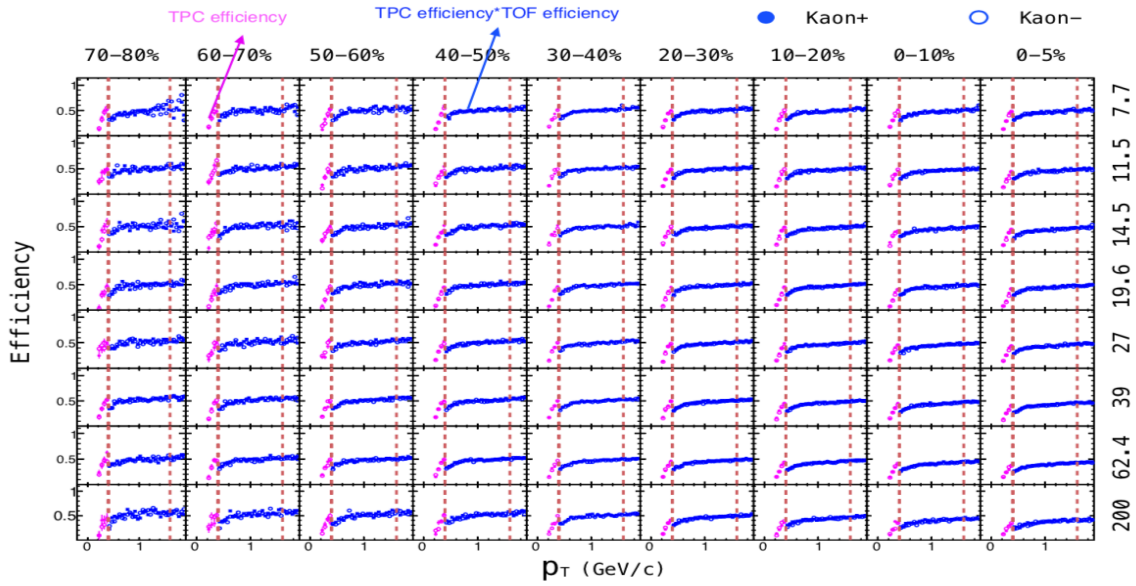


Figure 5.23:  $p_T$  dependence  $k^+$  and  $k^-$  efficiencies.

$$\varepsilon_{ch}^i = \frac{p^i}{p^i + k^i + \pi^i} \varepsilon_p^i + \frac{k^i}{p^i + k^i + \pi^i} \varepsilon_k^i + \frac{\pi^i}{p^i + k^i + \pi^i} \varepsilon_\pi^i, \quad (5.17)$$

where,  $\varepsilon_{ch}^i$  is the differential charge particle efficiency for  $i^{th}$   $p_T$  bin.  $\varepsilon_p^i$ ,  $\varepsilon_k^i$  and  $\varepsilon_\pi^i$  are the differential proton, kaon and pion TPC efficiencies, already discussed in previous section.

The average charge efficiency over a range  $a$  to  $b$  is calculated from,

$$\langle \varepsilon_{\pm} \rangle = \frac{\int_a^b \left[ \varepsilon_{p^\pm}(p_T) f_{p^\pm}(p_T) + \varepsilon_{k^\pm}(p_T) f_{k^\pm}(p_T) + \varepsilon_{\pi^\pm}(p_T) f_{\pi^\pm}(p_T) \right] p_T dp_T}{\int_a^b \left[ f_{p^\pm}(p_T) + f_{k^\pm}(p_T) + f_{\pi^\pm}(p_T) \right] p_T dp_T}, \quad (5.18)$$

where  $f_x(p_T)$  [ $x = p, \bar{p}, k^+, k^-, \pi^+$  and  $\pi^-$ ] are the efficiency corrected transverse momentum spectral function for  $p, \bar{p}, k^+, k^-, \pi^+$ , and  $\pi^-$ , respectively [113, 114].

5.7. EFFICIENCY CORRECTION

cent(%)	$\langle \varepsilon_{p,1} \rangle$	$\langle \varepsilon_{p,2} \rangle$	$\langle \varepsilon_{\bar{p},1} \rangle$	$\langle \varepsilon_{\bar{p},2} \rangle$	$\langle \varepsilon_{k^+,1} \rangle$	$\langle \varepsilon_{k^+,2} \rangle$	$\langle \varepsilon_{k^-,1} \rangle$	$\langle \varepsilon_{k^-,2} \rangle$	$\langle \varepsilon_{Q^+} \rangle$	$\langle \varepsilon_{Q^-} \rangle$
7.7 GeV										
0→5	0.829	0.588	0.787	0.548	0.342	0.413	0.334	0.414	0.803	0.812
5→10	0.844	0.601	0.794	0.554	0.345	0.420	0.358	0.414	0.815	0.830
10→20	0.854	0.615	0.812	0.564	0.339	0.428	0.354	0.432	0.826	0.833
20→30	0.862	0.621	0.828	0.564	0.364	0.439	0.358	0.434	0.835	0.846
30→40	0.870	0.633	0.844	0.589	0.363	0.446	0.349	0.443	0.844	0.852
40→50	0.873	0.641	0.849	0.584	0.373	0.452	0.348	0.461	0.852	0.856
50→60	0.896	0.639	0.857	0.586	0.351	0.450	0.355	0.443	0.851	0.861
60→70	0.889	0.631	0.831	0.597	0.371	0.446	0.410	0.454	0.852	0.878
70→80	0.890	0.607	0.836	0.590	0.380	0.423	0.379	0.412	0.860	0.870
11.5 GeV										
0→5	0.795	0.564	0.770	0.528	0.319	0.398	0.288	0.396	0.777	0.785
5→10	0.827	0.575	0.784	0.542	0.324	0.406	0.354	0.398	0.793	0.799
10→20	0.831	0.585	0.818	0.549	0.331	0.414	0.345	0.419	0.801	0.811
20→30	0.865	0.603	0.821	0.569	0.351	0.424	0.345	0.432	0.816	0.833
30→40	0.877	0.613	0.840	0.579	0.329	0.453	0.375	0.436	0.834	0.834
40→50	0.893	0.614	0.861	0.596	0.386	0.449	0.347	0.441	0.844	0.838
50→60	0.900	0.633	0.858	0.583	0.392	0.450	0.347	0.442	0.844	0.834
60→70	0.886	0.631	0.844	0.602	0.420	0.462	0.439	0.457	0.849	0.862
70→80	0.898	0.630	0.887	0.571	0.397	0.448	0.370	0.447	0.852	0.866
14.5 GeV										
0→5	0.777	0.568	0.680	0.502	0.342	0.395	0.342	0.395	0.766	0.776
5→10	0.784	0.581	0.700	0.507	0.346	0.407	0.346	0.407	0.783	0.787
10→20	0.804	0.587	0.713	0.518	0.365	0.418	0.365	0.418	0.796	0.794
20→30	0.794	0.606	0.698	0.532	0.386	0.424	0.386	0.424	0.799	0.805

30→40	0.809	0.613	0.720	0.539	0.379	0.435	0.379	0.435	0.812	0.820
40→50	0.810	0.617	0.740	0.555	0.374	0.444	0.374	0.444	0.815	0.825
50→60	0.811	0.629	0.730	0.553	0.370	0.441	0.370	0.441	0.820	0.837
60→70	0.832	0.620	0.768	0.574	0.380	0.455	0.380	0.455	0.826	0.833
70→80	0.817	0.610	0.725	0.535	0.355	0.433	0.355	0.433	0.825	0.814
19.6 GeV										
0→5	0.782	0.567	0.747	0.523	0.319	0.389	0.306	0.380	0.756	0.759
05→10	0.815	0.576	0.767	0.536	0.331	0.402	0.311	0.397	0.776	0.786
10→20	0.824	0.595	0.791	0.548	0.356	0.418	0.333	0.406	0.792	0.792
20→30	0.847	0.616	0.798	0.567	0.337	0.439	0.345	0.422	0.807	0.811
30→40	0.868	0.628	0.828	0.580	0.372	0.440	0.324	0.437	0.823	0.817
40→50	0.882	0.638	0.806	0.585	0.345	0.447	0.316	0.442	0.828	0.836
50→60	0.891	0.656	0.825	0.598	0.366	0.449	0.372	0.440	0.834	0.834
60→70	0.884	0.660	0.857	0.614	0.372	0.455	0.410	0.446	0.827	0.841
70→80	0.906	0.671	0.864	0.582	0.421	0.460	0.335	0.468	0.850	0.841
27 GeV										
0→5	0.779	0.546	0.726	0.517	0.312	0.387	0.304	0.386	0.738	0.739
5→10	0.789	0.559	0.744	0.529	0.338	0.404	0.326	0.389	0.751	0.750
10→20	0.809	0.577	0.774	0.548	0.332	0.420	0.314	0.418	0.774	0.783
20→30	0.839	0.599	0.792	0.569	0.352	0.438	0.341	0.429	0.794	0.794
30→40	0.855	0.616	0.810	0.576	0.364	0.449	0.353	0.438	0.806	0.801
40→50	0.882	0.634	0.824	0.593	0.373	0.448	0.358	0.453	0.823	0.829
50→60	0.871	0.636	0.812	0.606	0.361	0.465	0.409	0.450	0.827	0.831
60→70	0.860	0.645	0.852	0.603	0.364	0.467	0.377	0.461	0.833	0.818
70→80	0.893	0.646	0.853	0.610	0.416	0.465	0.420	0.475	0.837	0.848
39 GeV										
0→5	0.738	0.527	0.705	0.490	0.295	0.376	0.284	0.365	0.722	0.730

5.7. EFFICIENCY CORRECTION

05→10	0.777	0.546	0.737	0.513	0.320	0.387	0.310	0.383	0.748	0.756
10→20	0.805	0.566	0.770	0.535	0.332	0.408	0.316	0.401	0.772	0.773
20→30	0.841	0.594	0.813	0.558	0.354	0.430	0.352	0.418	0.799	0.801
30→40	0.864	0.617	0.830	0.576	0.354	0.442	0.362	0.438	0.818	0.823
40→50	0.886	0.625	0.845	0.590	0.373	0.455	0.371	0.449	0.838	0.836
50→60	0.891	0.634	0.863	0.601	0.359	0.459	0.387	0.457	0.843	0.843
60→70	0.898	0.636	0.845	0.614	0.360	0.460	0.365	0.463	0.841	0.853
70→80	0.902	0.645	0.890	0.616	0.398	0.471	0.379	0.474	0.854	0.860
62.4 GeV										
0→5	0.686	0.488	0.662	0.459	0.266	0.354	0.279	0.348	0.696	0.698
5→10	0.713	0.505	0.690	0.478	0.287	0.368	0.290	0.360	0.721	0.717
10→20	0.751	0.528	0.734	0.503	0.307	0.386	0.302	0.383	0.750	0.747
20→30	0.795	0.556	0.766	0.523	0.317	0.405	0.315	0.400	0.777	0.775
30→40	0.820	0.577	0.779	0.541	0.316	0.418	0.325	0.413	0.799	0.797
40→50	0.830	0.594	0.788	0.555	0.350	0.435	0.351	0.429	0.815	0.803
50→60	0.850	0.599	0.805	0.563	0.363	0.435	0.338	0.435	0.828	0.821
60→70	0.877	0.610	0.843	0.570	0.357	0.440	0.348	0.430	0.827	0.832
70→80	0.881	0.609	0.851	0.575	0.426	0.446	0.376	0.436	0.837	0.834
200 GeV										
0→5	0.617	0.464	0.581	0.357	0.242	0.350	0.253	0.342	0.602	0.607
5→10	0.644	0.490	0.630	0.395	0.276	0.375	0.235	0.360	0.637	0.645
10→20	0.693	0.533	0.667	0.430	0.255	0.403	0.282	0.392	0.685	0.682
20→30	0.757	0.574	0.730	0.468	0.279	0.426	0.293	0.428	0.731	0.727
30→40	0.796	0.610	0.762	0.496	0.310	0.456	0.308	0.446	0.761	0.762
40→50	0.830	0.630	0.791	0.524	0.351	0.470	0.327	0.458	0.784	0.789
50→60	0.848	0.649	0.817	0.531	0.335	0.468	0.340	0.457	0.803	0.786
60→70	0.863	0.664	0.836	0.546	0.336	0.484	0.436	0.455	0.813	0.811

70→80	0.867	0.662	0.823	0.570	0.348	0.494	0.371	0.465	0.823	0.834
-------	-------	-------	-------	-------	-------	-------	-------	-------	-------	-------

Table 5.6: Average efficiency ( $\langle \varepsilon \rangle$ ) values for  $p$ ,  $\bar{p}$ ,  $k^+$ ,  $k^-$ ,  $Q^+$ , and  $Q^-$  for two different  $p_T$  bin and  $Q^-$  at  $\sqrt{s_{NN}} = 7.7, 11.5, 14.5, 19.6, 27, 39, 62.4,$  and  $200$  GeV in different centralities.

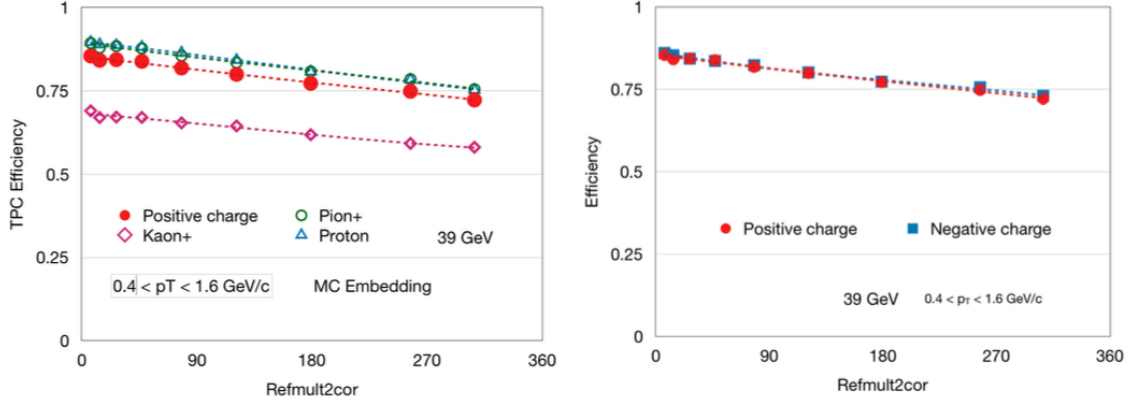


Figure 5.24: Average charge particle efficiencies for 39 GeV.

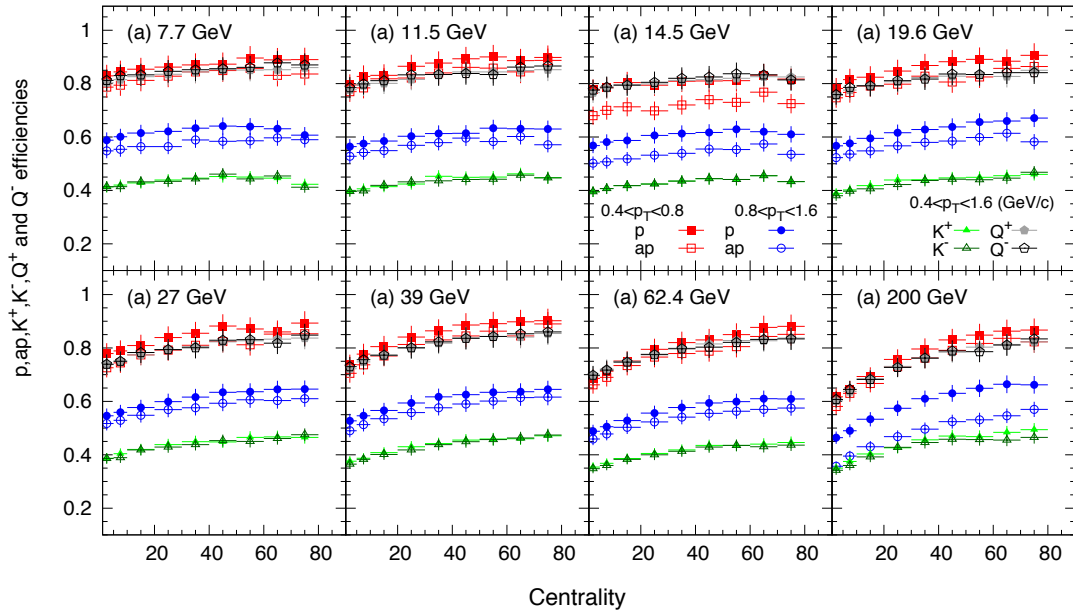


Figure 5.25:  $p_T$  average protons, kaons, and charge particle efficiencies as a function of centrality in Au+Au collisions. For charge and proton in lower  $p_T$  range ( $0.4 < p_T < 0.8$  GeV/c) only TPC is used. For kaons ( $0.4 < p_T < 1.6$  GeV/c) and proton in higher  $p_T$  range ( $0.8 < p_T < 1.6$  GeV/c) both TPC and TOF are used. Solid points for positive particle and open points for negative particle.

## 5.8 Uncertainty estimation

The uncertainty estimation is one of the important aspects of any experimental measurement. Uncertainty is a range in which repeated measurements will fall. Uncertainties are mainly classified into two types, (a) statistical uncertainties – represent the precision limit of the experiment and (b) systematic uncertainties – represent the accuracy limit of the measurement. Precision is the repeatability of the measurement, whereas accuracy is the degree to which the measurement agrees with the actual value. It is necessary to consider the accuracy and precision simultaneously for any experiment. A high precision data cannot be accepted if it is highly inaccurate. Also, data value cannot be considered as extremely accurate if the precision is low. For this analysis, we estimated both statistical and systematic uncertainty to report the precision and accuracy of our measurement, are discussed in section 5.8.1 and 5.8.2, respectively.

### 5.8.1 Statistical uncertainty

The statistical uncertainty represents the random fluctuation in observables each time the experiment is repeated. Statistical uncertainty arise due to a limited number of measurements, and it can be reduced by making more and more measurements. In e-by-e case, these can be done by increasing number of events sample. The statistical uncertainty estimation is based on numerical error propagation method of multivariate cumulants [66].

The statistical error of a quantity  $\phi(= \phi(X_i))$  is defined as  $\sqrt{V(\phi)}$ , where  $V(\phi)$  is its sampling variance,

$$V(\phi) = \sum_{i=1, j=1}^m \frac{\partial \phi}{\partial X_i} \frac{\partial \phi}{\partial X_j} Cov(X_i, X_j). \quad (5.19)$$

The sampling variance of the  $2^{nd}$  order cumulant ratio is defined as,

$$\begin{aligned}
V(\phi = \mu_{1,1}/\mu_{0,2}) &= \left(\frac{\partial\phi}{\partial\mu_{1,1}}\right)^2 V(\mu_{1,1}) + \left(\frac{\partial\phi}{\partial\mu_{0,2}}\right)^2 V(\mu_{0,2}) \\
&+ 2 \frac{\partial\phi}{\partial\mu_{1,1}} \frac{\partial\phi}{\partial\mu_{0,2}} Cov(\mu_{1,1}, \mu_{0,2}).
\end{aligned} \tag{5.20}$$

The sampling variance ( $V(\mu_{r,s})$ ) and covariance ( $Cov(\mu_{r,s}, c_{u,v})$ ) are expressed as follows [66],

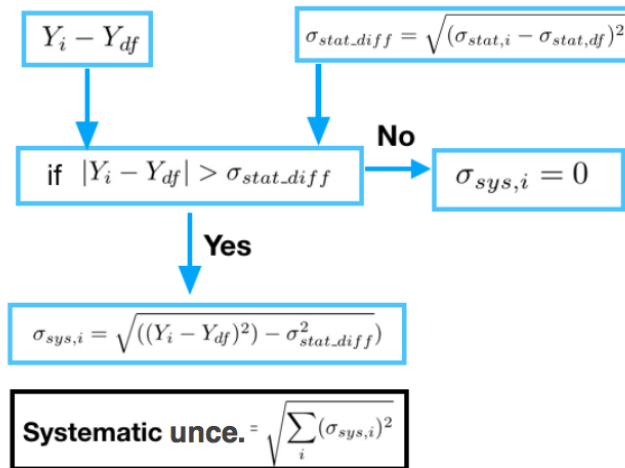
$$\begin{aligned}
V(\mu_{r,s}) &= \frac{1}{n} (\mu_{2r,2s} - \mu_{r,s}^2 + r^2 \mu_{2,0} \mu_{r-1,s}^2 + s^2 \mu_{0,2} \mu_{r,s-1}^2 + \\
&2rs\mu_{1,1}\mu_{r-1,s}\mu_{r,s-1} - 2r\mu_{r+1,s}\mu_{r-1,s} - 2s\mu_{r,s+1}\mu_{r,s-1}),
\end{aligned} \tag{5.21}$$

$$\begin{aligned}
Cov(\mu_{r,s}, \mu_{u,v}) &= \frac{1}{n} (\mu_{r+s,u+v} - \mu_{r,s}\mu_{u,v} + ru\mu_{2,0}\mu_{r-1,s}\mu_{u-1,v} + su\mu_{0,2}\mu_{r,s-1} \\
&\mu_{u,v-1} + rv\mu_{1,1}\mu_{r-1,s}\mu_{u,v-1} + sv\mu_{1,1}\mu_{r,s-1}\mu_{u-1,v} \\
&- u\mu_{r+1,s}\mu_{u-1,v} - v\mu_{r,s+1}\mu_{u,v-1} - r\mu_{r-1,s}\mu_{u+1,v} \\
&- s\mu_{r,s+1}\mu_{u,v-1}).
\end{aligned} \tag{5.22}$$

Here,  $n$  is the number of events in the sample.  $\mu_{r,s}$  represents a  $r + s$ -th order bivariate central moment (and  $\mu_{1,0} = \mu_{0,1} = 0$ ). To report proper precision of the observables, first efficiency correction is necessary for  $V(\mu_{r,s})$  and  $Cov(\mu_{r,s}, c_{u,v})$  as discussed in section 5.7. The efficiency corrected expression in terms of factorial moment for these uncertainty terms are very lengthy. This is done by SMoment framework, which include a number of algorithms based on moment generating functions [112].

## 5.8.2 Systematic uncertainties

Systematic uncertainties arise due to experimental limitation. The uncertainty in accuracy has been studied by varying different experimental cuts used to select the data sample. Our systematic uncertainty estimation is done based on the following flowchart 5.26. We vary different systematic cuts and pick those cuts whose mean of particle yield falls within 5% of its default value, as shown in Fig. 5.27. To remove/minimize the statistical fluctuation from systematic uncertainties the statistical contribution has been subtracted as described in the above method. In our analysis, for  $2^{nd}$  order cumulants, the statistical uncertainties is significantly small compared to systematic uncertainties. Different systematic cuts are listed below:



$Y_i$  : value of  $i^{\text{th}}$  case of systematic

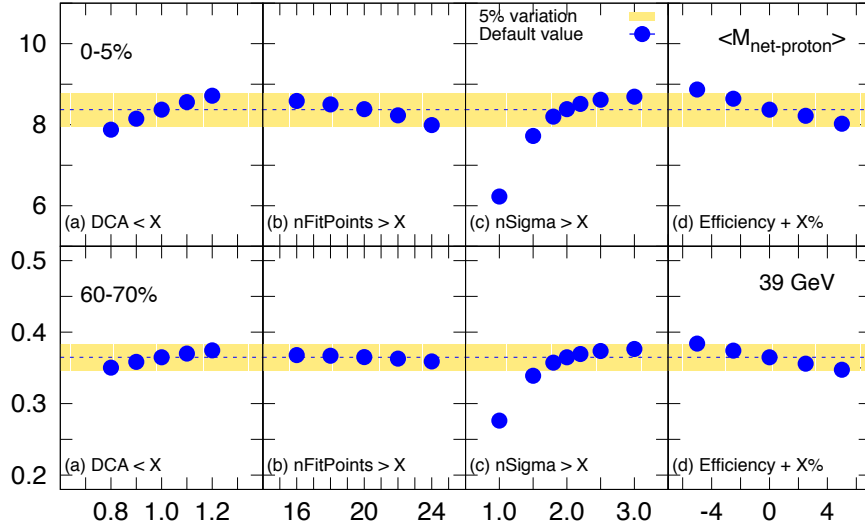
$Y_{df}$  : default case

$\sigma_{stat,i}$  : **Systematic uncertainty of  $i^{\text{th}}$  case**

$\sigma_{stat}$  : **Systematic uncertainty**

Figure 5.26: Systematic uncertainty estimation flowchart

- DCA < 0.8, 0.9, 1.0 (de), 1.1, 1.2,

Figure 5.27:  $\langle \text{net-proton} \rangle$  as a function of different systematic cuts

- nFitPoints  $> 16, 18, 20$  (de),  $22, 24$ ,
- nSigma  $> 1.5, 1.8, 2.0$  (de),  $2.2, 2.5$ ,
- Efficiencies: varying  $+5\%$  and  $-5\%$ .

The efficiency, estimated from the embedding sample, is not precise. It is observed that there is 5% variation in efficiency due to TPC GEANT simulations. This variation are included in systematic error in cumulant analysis. In this case, the efficiency for each centrality is varied  $\pm 5\%$  of the default values. The efficiency corrected (using default efficiencies) cumulants ratios at different DCA, nFitpoints,  $n\sigma$  cut and using  $\pm 5\%$  efficiency variation for Au+Au collisions at  $\sqrt{s_{NN}} = 7.7, 39, \text{ and } 200$  GeV are shown in Fig. 5.28. The systematic uncertainties for the cumulant ratios are found to vary within 8-15% for different beam energies.

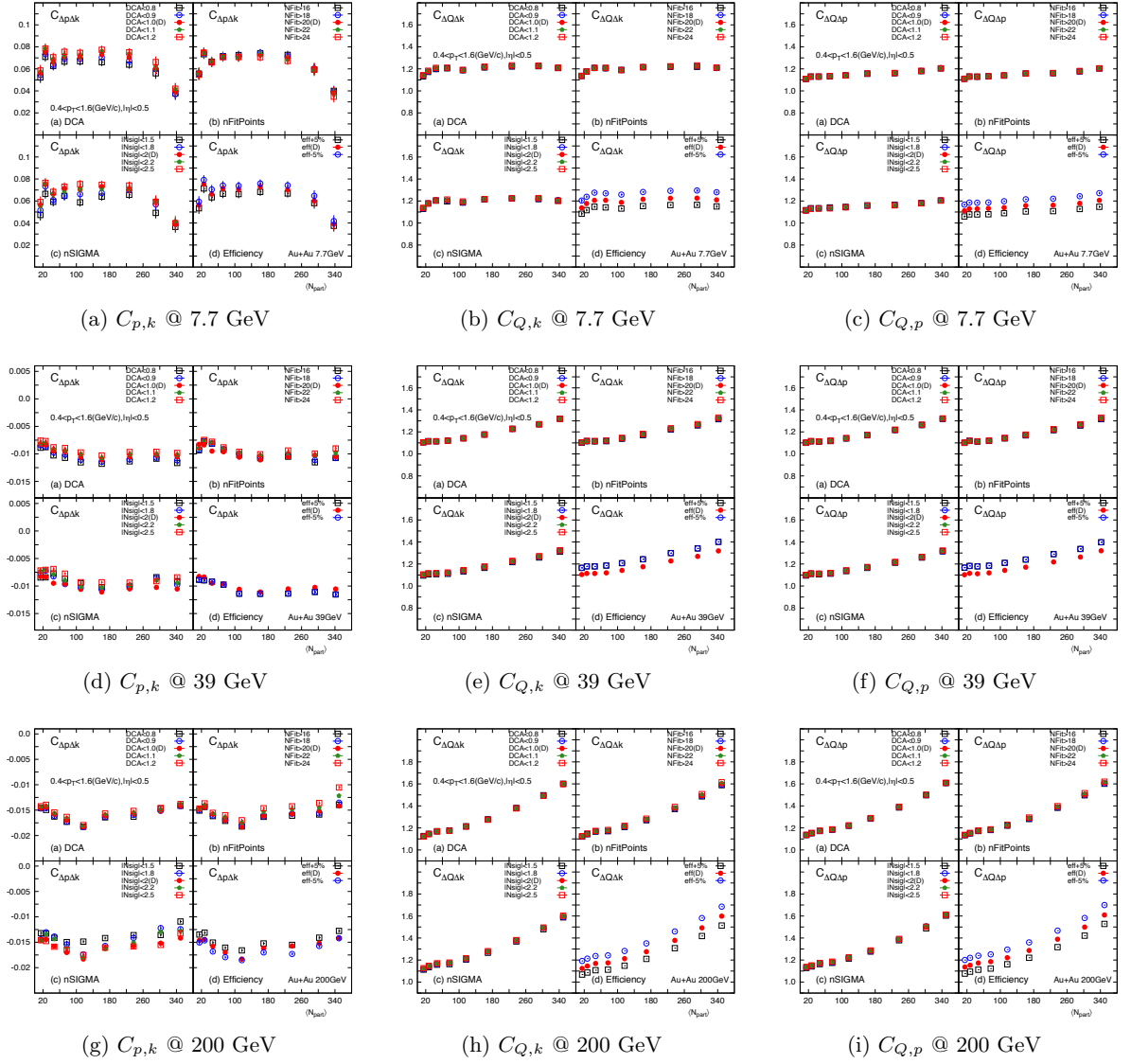


Figure 5.28: Systematic variation of  $C_{p,k}$ ,  $C_{Q,k}$  and  $C_{Q,p}$  for different cuts at Au+Au 7.7 (top row), 39 (middle row), and 200 (bottom row) GeV.



# Chapter 6

## Results from STAR data

In this chapter, we discuss the results of the measurement of all  $2^{nd}$  order cumulant elements at STAR BES energies using the analysis method described in the previous chapter. Measured values of the observables are compared with different models and their respective Poissonian baselines. First, we discuss the event-by-event net-identified particles and net-charge raw distributions for  $Au + Au$  collisions for different beam energies. Then I will talk about the efficiency corrected acceptance ( $|\eta|$ ) and centrality dependence of these cumulants for eight beam energies. Finally, we will discuss the volume independent  $2^{nd}$  order off-diagonal to diagonal cumulants ratios and compare them with different models and baselines.

### 6.1 Net-particles multiplicity distributions and correlations

Event-by-event raw (efficiency uncorrected) multiplicity distributions for net-proton, net-kaon and net-pion for  $Au + Au$  collisions at  $\sqrt{s_{NN}} = 7.7$  to 200 GeV within  $|\eta| < 0.5$  and  $0.4 < p_T < 1.6$  GeV/c are shown in Figures 6.1, 6.2 and 6.3, respectively. Distributions are presented for three different centralities: top-central (0-5%), mid-central (30-40%) and peripheral (60-70%) collisions. Going from peripheral to central collisions, the distributions become wider. Mean values of Net-

proton ( $\Delta p = p - \bar{p}$ ) increase with decreasing in energy due to the stopping of baryons at lower energies. At the initial stage, before the collision, systems do not have any pions and kaons. Event-by-event net-kaon ( $\Delta k = k^+ - k^-$ ) become wider with increasing center of mass energy. It is also observed that the net-kaon mean values shift towards zero from positive value as the beam energy increases. This is because the pair production of kaons ( $k^+/k^-$ ) dominate at higher energies, while the production of  $k^+$  dominates due to associate production via reaction channel  $NN \rightarrow N\Lambda k^+$  [115] at lower energy. The mean of the net-pion ( $\Delta\pi = \pi^+ - \pi^-$ ) multiplicity distributions are close to zero, and the width of the distributions increases with collision energy. Within our transverse momentum acceptance cut ( $p_T > 0.4$ ) a majority part of pions has been excluded. Figure 6.4 shows the net-charge ( $\Delta Q = Q^+ - Q^-$ ) multiplicity distributions for all eight BES energies within  $|\eta| < 0.5$  and  $0.4 < p_T < 1.6$  GeV/c for three different collision centralities. We observed that the mean values of net-charge distributions shift towards zero from the positive value with increasing beam energy. The distributions become wider with the increase in beam energy. It explains by individual net- $p, k, \pi$  distributions because the cumulants are additive. So, the mean and width of net-charge distribution will be proportional to the sum of mean and the width of individual net-proton, net-kaon, and net-pion distributions. It is observed that with the increase in colliding beam-energy the distributions become more symmetric about their mean. This is because at higher energies more and more particles are produced, which leads to a normal distribution as expected from Central Limit Theorem (CLT).

Event-by-event efficiency uncorrected net-proton vs net-kaon, net-charge vs net-kaon and net-charge vs net-proton multiplicity distributions for various  $Au + Au$  collision energies from  $\sqrt{s_{NN}} = 7.7$  to 200 GeV within  $|\eta| < 0.5$  and  $0.4 < p_T < 1.6$  GeV/c are shown in Fig. 6.5, 6.6 and 6.7 respectively. In Fig. 6.5 we observe that the correlation between net-proton and net-kaon is close to zero at higher energies and the correlation is positive in lower energies. Strong correlations are

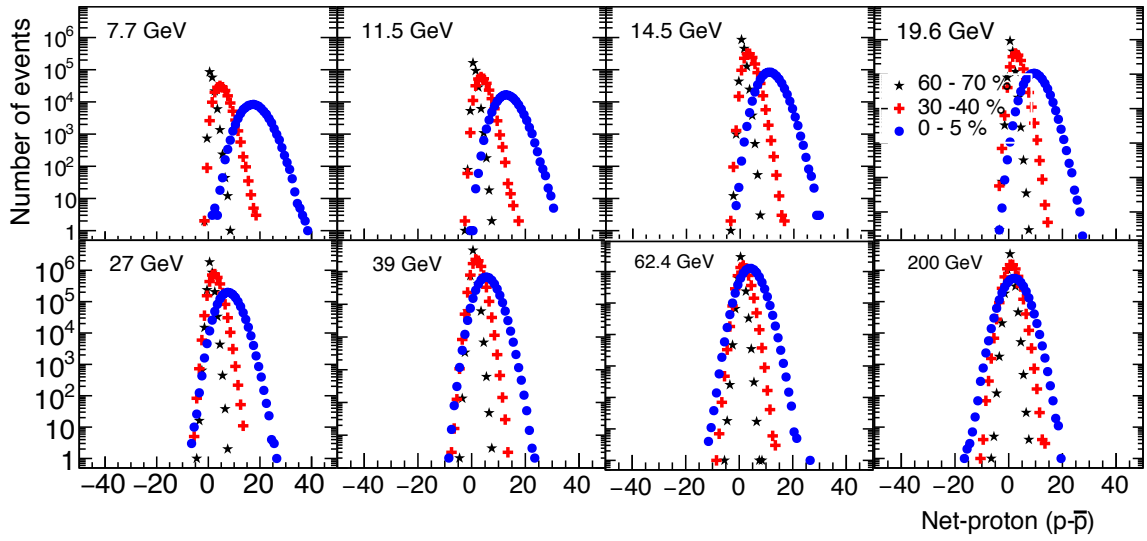


Figure 6.1: Efficiency uncorrected net-proton ( $\Delta p = p - \bar{p}$ ) multiplicity distributions in  $Au + Au$  collisions at  $\sqrt{s_{NN}} = 7.7, 11.5, 14.5, 19.6, 27, 39, 62.4$  and  $200$  GeV measured within kinematic range  $|\eta| < 0.5$  and  $0.4 < p_T < 1.6$  GeV/c in three different centralities (0-5%, 30-40%, and 60-70%).

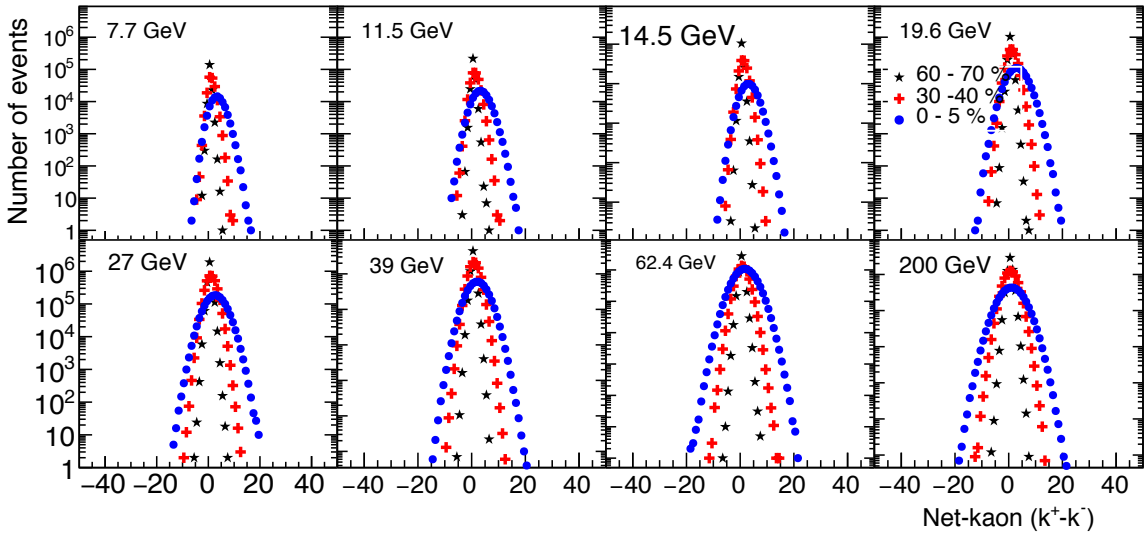


Figure 6.2: Efficiency uncorrected net-kaon ( $\Delta k = k^+ - k^-$ ) multiplicity distributions in  $Au + Au$  collisions at  $\sqrt{s_{NN}} = 7.7, 11.5, 14.5, 19.6, 27, 39, 62.4$  and  $200$  GeV measured within kinematic range  $|\eta| < 0.5$  and  $0.4 < p_T < 1.6$  GeV/c in three different centralities (0-5%, 30-40%, and 60-70%).

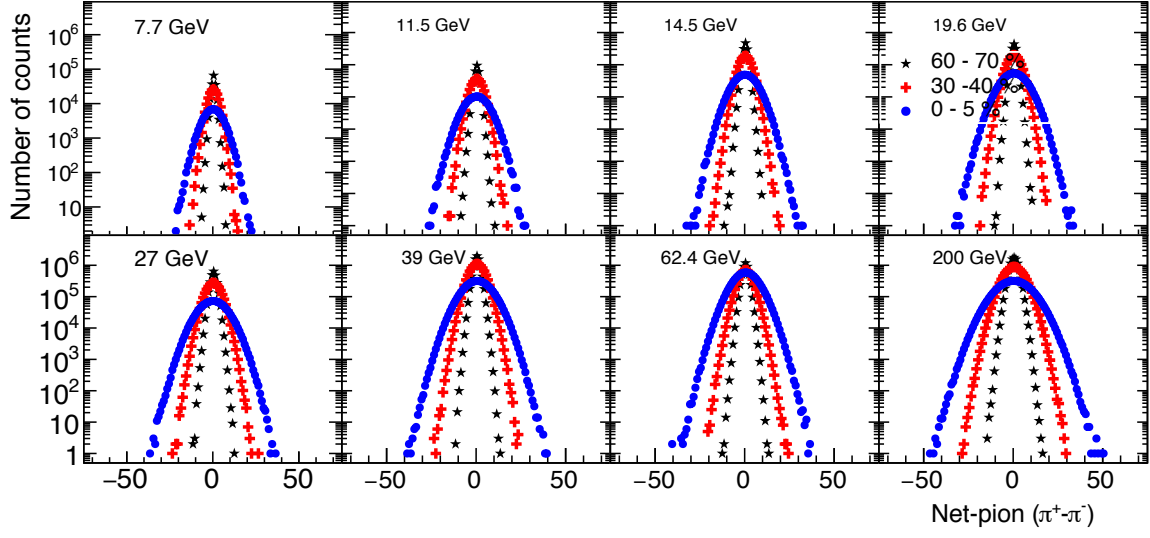


Figure 6.3: Efficiency uncorrected net-pion ( $\Delta\pi = \pi^+ - \pi^-$ ) multiplicity distributions in  $Au + Au$  collisions at  $\sqrt{s_{NN}} = 7.7, 11.5, 14.5, 19.6, 27, 39, 62.4$  and  $200$  GeV measured within kinematic range  $|\eta| < 0.5$  and  $0.4 < p_T < 1.6$  GeV/c in three different centralities (0-5%, 30-40%, and 60-70%).

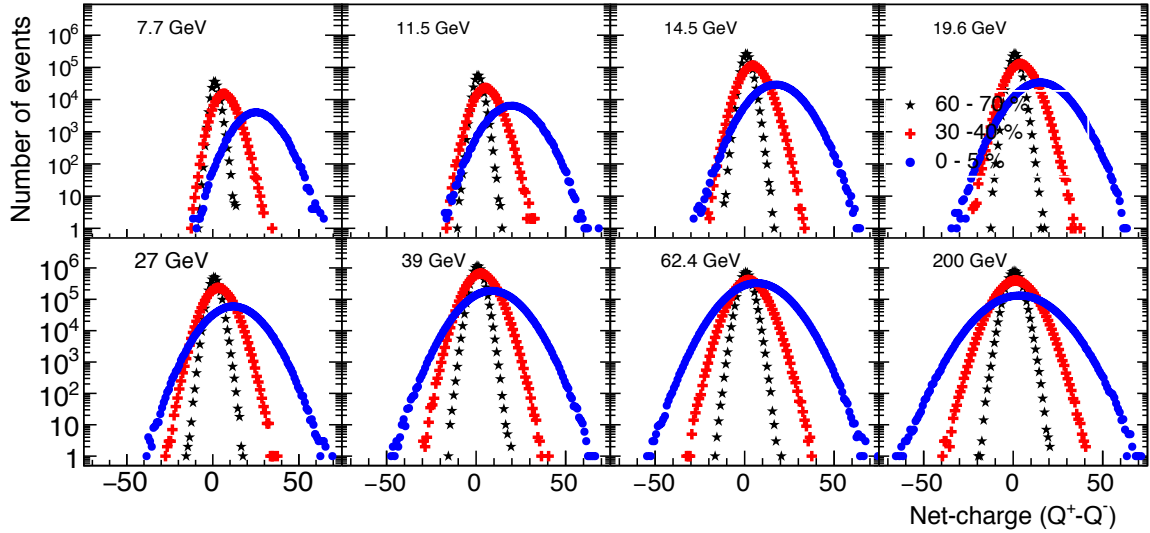


Figure 6.4: Efficiency uncorrected net-charge ( $\Delta Q = Q^+ - Q^-$ ) multiplicity distributions in  $Au + Au$  collisions at  $\sqrt{s_{NN}} = 7.7, 11.5, 14.5, 19.6, 27, 39, 62.4$  and  $200$  GeV measured within kinematic range  $|\eta| < 0.5$  and  $0.4 < p_T < 1.6$  GeV/c in three different centralities (0-5%, 30-40%, and 60-70%).

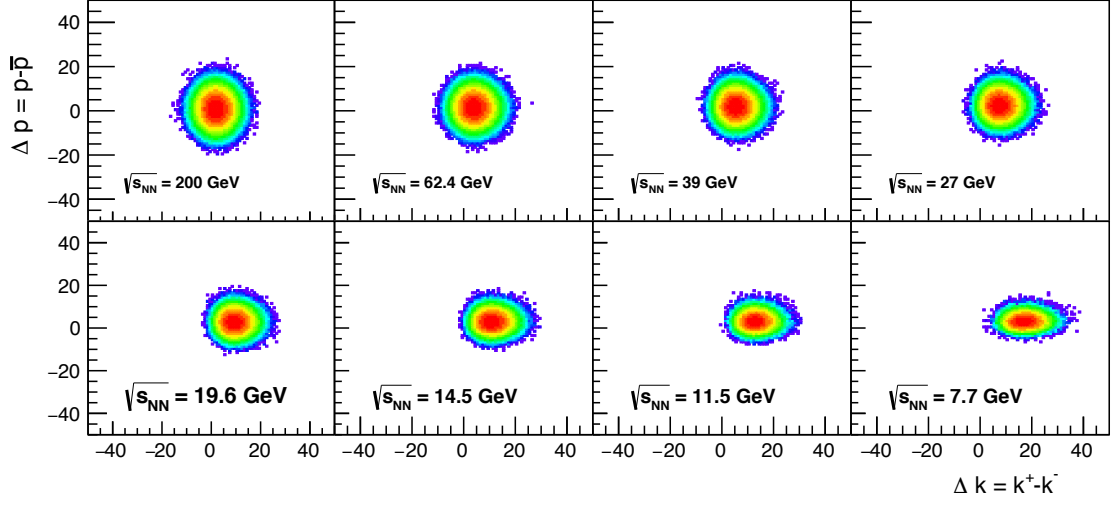


Figure 6.5: Efficiency uncorrected net-proton ( $\Delta p$ ) vs net-kaon ( $\Delta k$ ) multiplicity distributions in  $Au + Au$  collisions at  $\sqrt{s_{NN}} = 7.7, 11.5, 14.5, 19.6, 27, 39, 62.4$  and  $200$  GeV measured within kinematic range  $|\eta| < 0.5$  and  $0.4 < p_T < 1.6$  GeV/c in 0-5% central collisions.

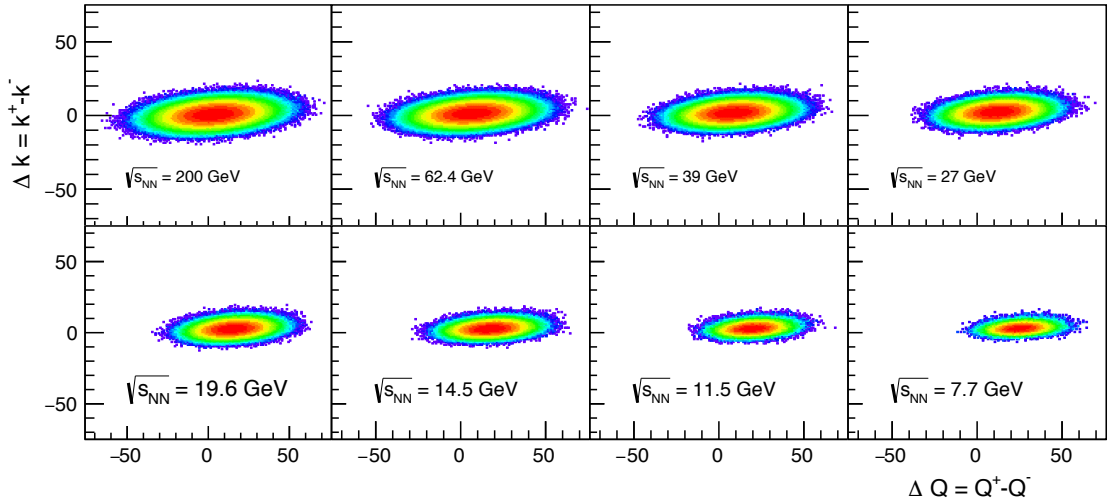


Figure 6.6: Efficiency uncorrected net-kaon ( $\Delta k$ ) vs net-charge ( $\Delta Q$ ) multiplicity distributions in  $Au + Au$  collisions at  $\sqrt{s_{NN}} = 7.7, 11.5, 14.5, 19.6, 27, 39, 62.4$  and  $200$  GeV measured within kinematic range  $|\eta| < 0.5$  and  $0.4 < p_T < 1.6$  GeV/c in 0-5% central collisions.

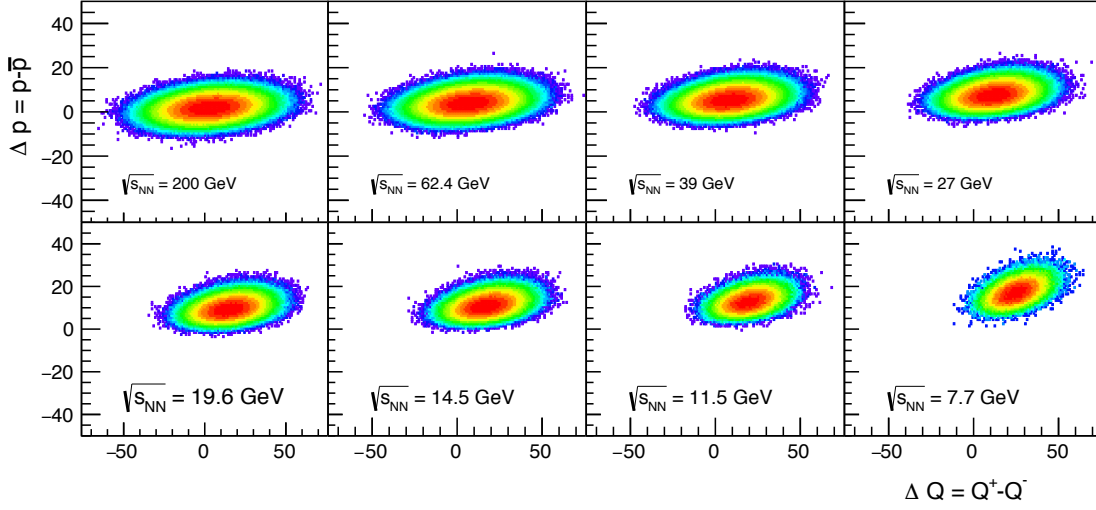


Figure 6.7: Efficiency uncorrected net-proton ( $\Delta p$ ) vs net-charge ( $\Delta Q$ ) multiplicity distributions in  $Au + Au$  collisions at  $\sqrt{s_{NN}} = 7.7, 11.5, 14.5, 19.6, 27, 39, 62.4$  and  $200$  GeV measured within kinematic range  $|\eta| < 0.5$  and  $0.4 < p_T < 1.6$  GeV/c in 0-5% central collisions.

observed between net-charge and net-kaon as well as net-charge and net-proton. The centrality dependence of various diagonal moments can be well described by the red dashed lines expected from CLT which also supports the independent identical emission sources assumption.

## 6.2 Centrality dependence of diagonal and off-diagonal cumulants

The centrality dependence of  $2^{nd}$  order diagonal cumulants ( $\sigma^2$ ) of net-proton (top-row), net-kaon (middle-row) and net-charge (bottom-row) for  $Au + Au$  collisions at  $\sqrt{s_{NN}} = 7.7, 11.5, 14.5, 19.6, 27, 39, 62.4$  and  $200$  GeV are shown in Fig. 6.8 as a function  $\langle N_{part} \rangle$ . The results are efficiency corrected using two- $p_T$  bin particle/antiparticle separate efficiencies as described in the previous chapter. Statistical error bars are within the marker size and boxes represents systematic errors.  $c_2$  of net-proton, net-kaon and net-charge increasing smoothly as a function of centrality for all energies. We find a linear increasing trend as expected from a scaling predicted by the central limit theorem (CLT:  $\sigma^2 \propto \langle N_{part} \rangle$ ).

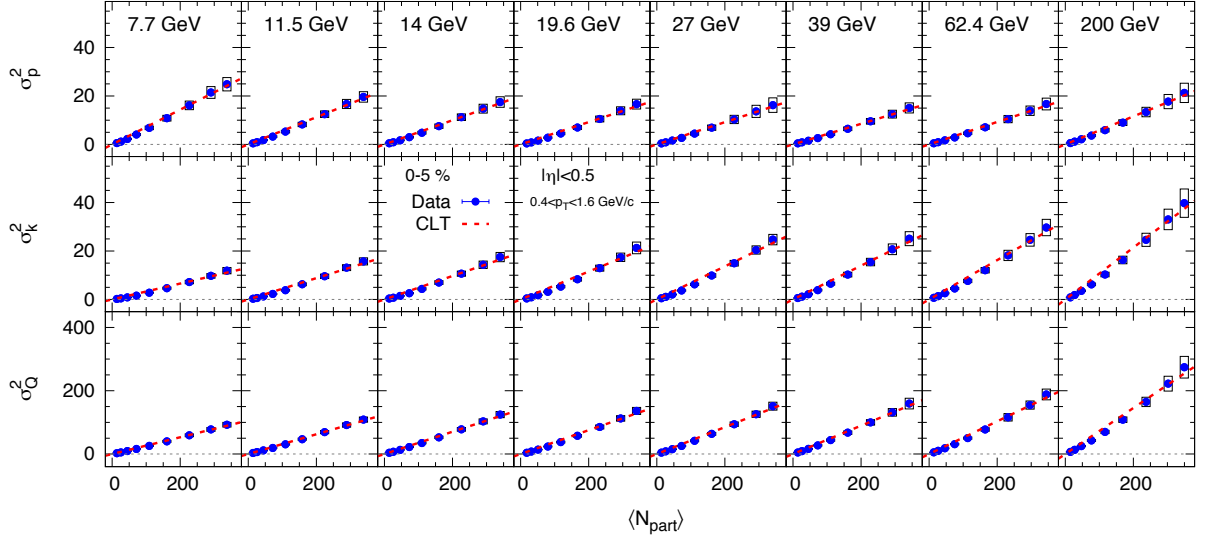


Figure 6.8: Centrality dependence of 2nd order diagonal cumulants (variances) of net-proton, net-kaon and net-charge (top to bottom) for Au+Au collisions at  $\sqrt{s_{NN}} = 7.7, 11.5, 14.5, 19.6, 27, 39, 62.4$  and  $200$  GeV (left to right). Error bars are statistical and box are systematic errors. The red dashed lines represent scaling predicted by central limit theorem.

Figure 6.9 shows the centrality dependence of  $2^{nd}$  order mixed cumulants between net-proton and net-kaon ( $\sigma_{p,k}^{1,1}$ ) (top row), net-charge and net-proton ( $\sigma_{Q,p}^{1,1}$ ) (middle row), and between net-charge and net-kaon ( $\sigma_{Q,k}^{1,1}$ ) (bottom row) within  $|\eta| < 0.5$  and  $0.4 < p_T < 1.6$  GeV/c for Au + Au collisions at  $\sqrt{s_{NN}} = 7.7$  to  $200$  GeV. The results are corrected for efficiency and finite centrality bin width effect.  $\sigma_{p,k}^{1,1}$  is positive at lower energy and negative at  $\geq 19.6$  GeV.  $\sigma_{Q,k}^{1,1}$  and  $\sigma_{Q,p}^{1,1}$  show linearly increasing trend as a function of  $\langle N_{part} \rangle$  and the correlations between net-charge and net-proton and between net-charge and net-kaon increase with the collision energy. The red dashed line shows that the values of these mixed cumulants show a similar trend of the CLT variation like the diagonal cumulants for all energies.

In Fig. 6.10 ratios between covariance to variance  $C_{p,k}$  ( $= \sigma_{p,k}^{1,1} / \sigma_k^2$ ),  $C_{Q,p}$  ( $= \sigma_{Q,p}^{1,1} / \sigma_p^2$ ) and  $C_{Q,k}$  ( $= \sigma_{Q,k}^{1,1} / \sigma_k^2$ ) are shown as a function of  $\langle N_{part} \rangle$ . The trivial volume dependence of the cumulants is expected to be cancelled in such ratios. The mixed cumulants between Q-k and Q-p are increases

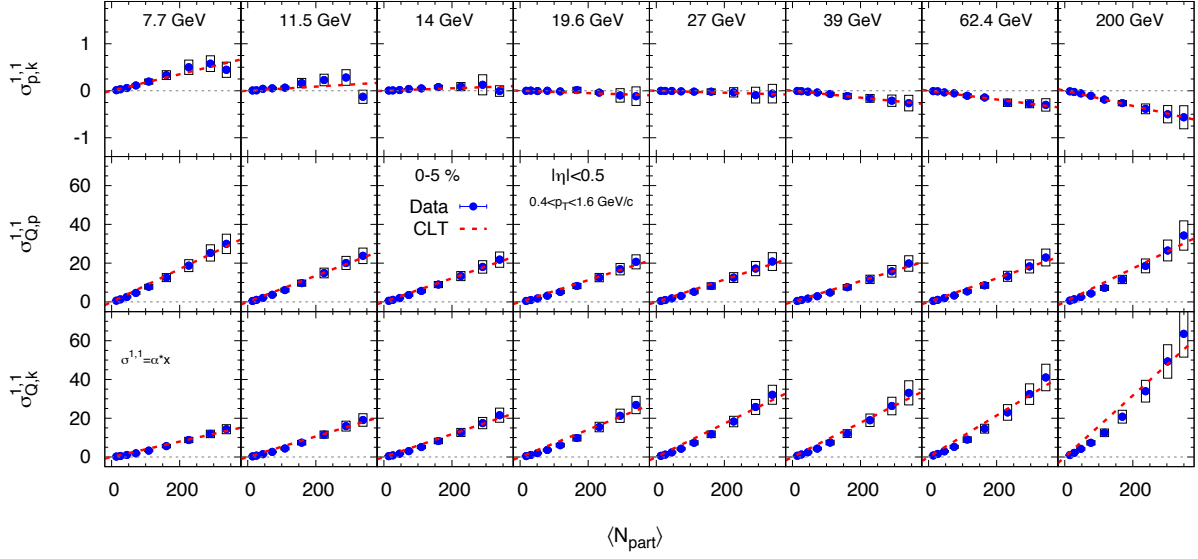


Figure 6.9: Centrality dependence of second-order off-diagonal cumulants of net-proton, net-charge and net-kaon for Au+Au collisions at  $\sqrt{s_{NN}} = 7.7, 11.5, 14.5, 19.6, 27, 39, 62.4$  and  $200$  GeV (left to right). Error bars are statistical and box are systematic errors. The red dashed lines represent scaling predicted by central limit theorem.

monotonically as a  $\langle N_{part} \rangle$ .

### 6.3 Pesudorapidity window dependence of cumulants

Within full phase spaces, net-charges are always conserved. It means that for a perfectly central  $Au + Au$  collision, the net-charge would be 158 in each event before and after collisions. But within a finite acceptance, there are fluctuations in conserved quantities in event-by-event basis. So for a finite and appropriate acceptance the event-by-event fluctuation study is possible. We varied the pseudorapidity acceptance and measured the cumulants in different ranges. To understand the evolution of various cumulants with phase space acceptance, we varied eta window, -0.1 to 0.1, -0.2 to 0.2, -0.3 to 0.3, -0.4 to 0.4 and -0.5 to 0.5 for a given  $p_T$  region 0.4 to 1.6 GeV/c. In Fig. 6.11, different  $2^{nd}$  order cumulants ( $\sigma^2$ ) of net-charge, net-proton and net-kaon, and cor-

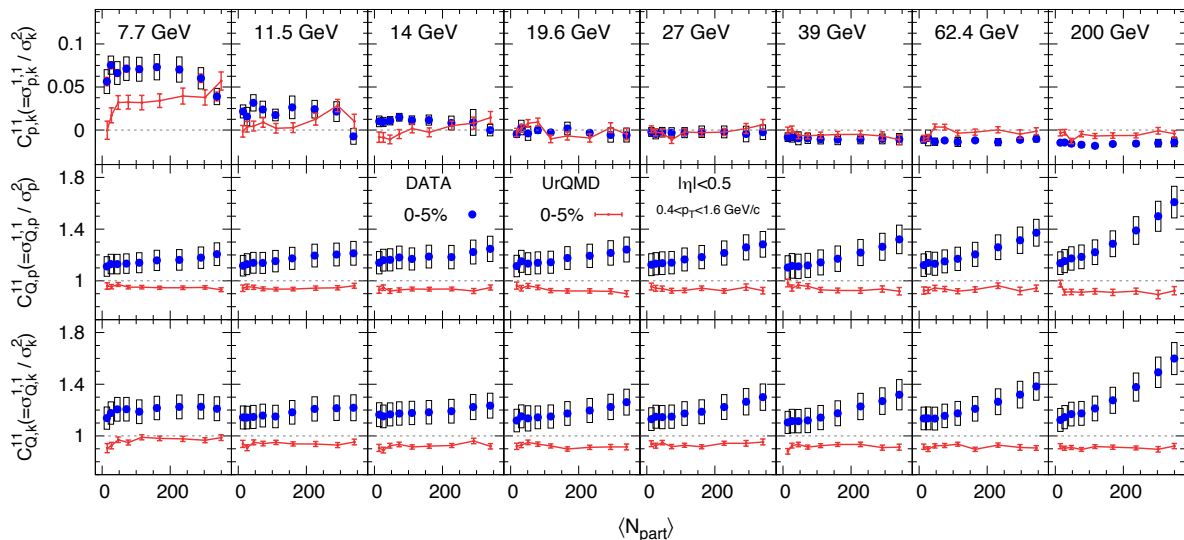


Figure 6.10: Centrality dependence of 2nd order off-diagonal to diagonal cumulants ratios of net-proton, net-charge and net-kaon for Au+Au  $\sqrt{s_{NN}} = 7.7, 11.5, 14.5, 19.6, 27, 39, 62.4$  and 200 GeV (left to right) within kinematic range  $|\eta| < 0.5$  and  $0.4 < p_T < 1.6$  GeV/c. Error bars are statistical and box are systematic errors. The red dashed lines represent UrQMD points.

relations ( $\sigma^{1,1}$ ) between them, are plotted for different  $\eta$ -ranges. The data are presented for two different centralities, most central 0-5% and peripheral 70-80%. One observes that by opening large acceptance window, the  $Q$ - $k$  and  $Q$ - $p$  correlations increase linearly. By increasing  $\eta$ -window a situation occurred where the cumulants saturate and then further increase in  $\eta$ -window, the fluctuations decrease and tend to zero with full phase space due to the global charge conservation. A detailed simulation study of these effect can be found in Reference [64]. Due to our current experimental limitation, we cannot access such a large phase space in the STAR experiment. In the future BES-II program with the iTPC upgrade, it shall be possible to extend the range considered in this work. Also, for the BES-II program, the centrality determination can be done by an independent Event Plane Detector (EPD) [116] over an acceptance window of  $2.1 < \eta < 5.1$ . Therefore, it will be possible to measure acceptance dependence of the cumulants using iTPC over a extensive  $\eta$ -window ( $\sim 1.7$ ) and search for deviations from a linear trend as predicted in [59? ?

].

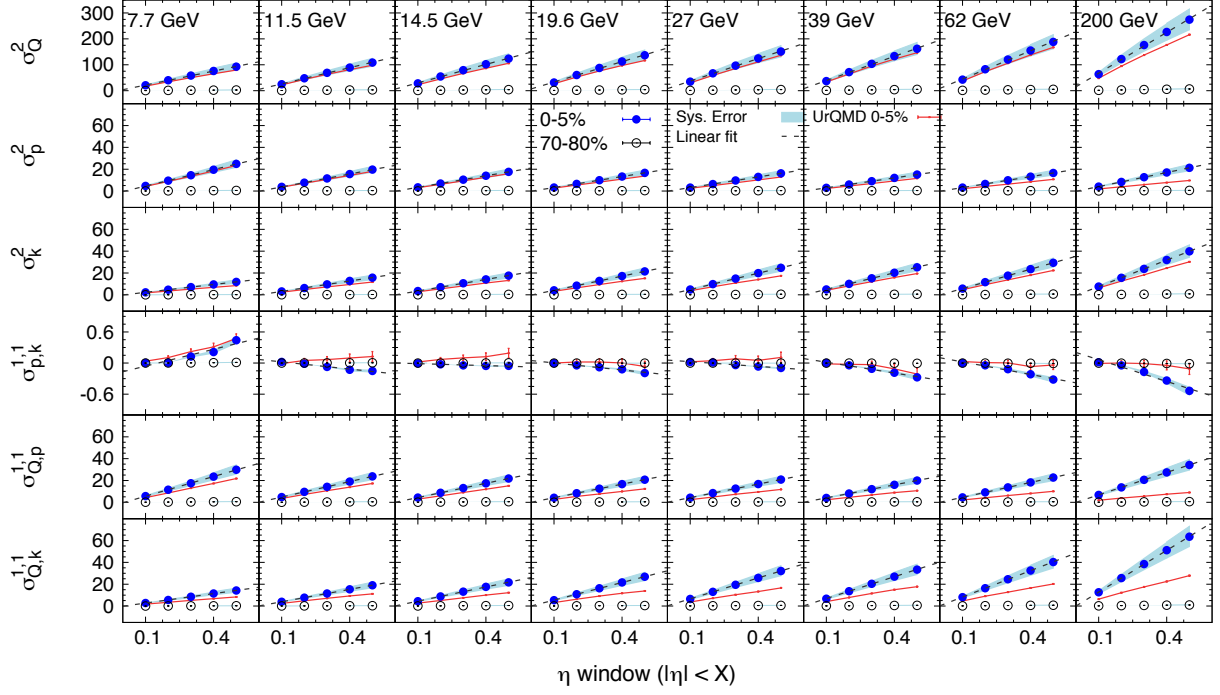


Figure 6.11:  $|\eta|$  acceptance dependence of  $2^{nd}$  order diagonal ( $\sigma_Q^2, \sigma_p^2, \sigma_k^2$ ) and off-diagonal ( $\sigma_{p,k}^{1,1}, \sigma_{Q,p}^{1,1}, \sigma_{Q,k}^{1,1}$ ) cumulants of net-proton ( $p$ ), net-charge ( $Q$ ) and net-kaon ( $k$ ) for Au+Au collisions at  $\sqrt{s_{NN}} = 7.7, 11.5, 14.5, 19.6, 27, 39, 62.4$  and  $200$  GeV (left to right). The vertical bars represent statistical uncertainties. Red lines represent UrQMD 0-5% points.

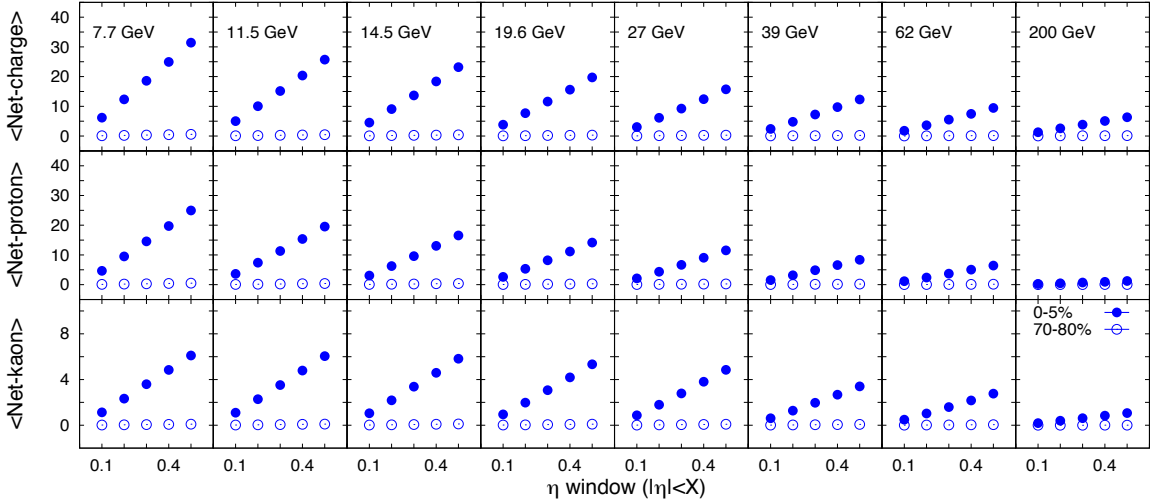


Figure 6.12:  $|\eta|$  acceptance dependence mean of net-proton, net-charge and net-kaon for Au+Au collisions at  $\sqrt{s_{NN}} = 7.7, 11.5, 14.5, 19.6, 27, 39, 62.4$  and  $200$  GeV (left to right). Error bars are statistical error.

## 6.4 Beam energy dependence cumulant ratios

The aim of RHIC Beam Energy Scan program is to explore the QCD phase diagram. By varying the centre of mass energy of the colliding beam, it is possible to vary the baryon chemical potential at central rapidity [78]. The RHIC BES results shows that in BES program the QCD phase diagram can be covered from 25 to 420 MeV for 0-5% central collision data from 200 below to 7.7 GeV Au+Au collisions. The energy dependence of cumulant ratios ( $\sigma_{p,k}^{11}/\sigma_k^2$ ,  $\sigma_{Q,p}^{11}/\sigma_p^2$  and  $\sigma_{Q,k}^{11}/\sigma_k^2$ ) for two different centrality bins (0-5% and 70-80%) are presented in Figure 6.13.

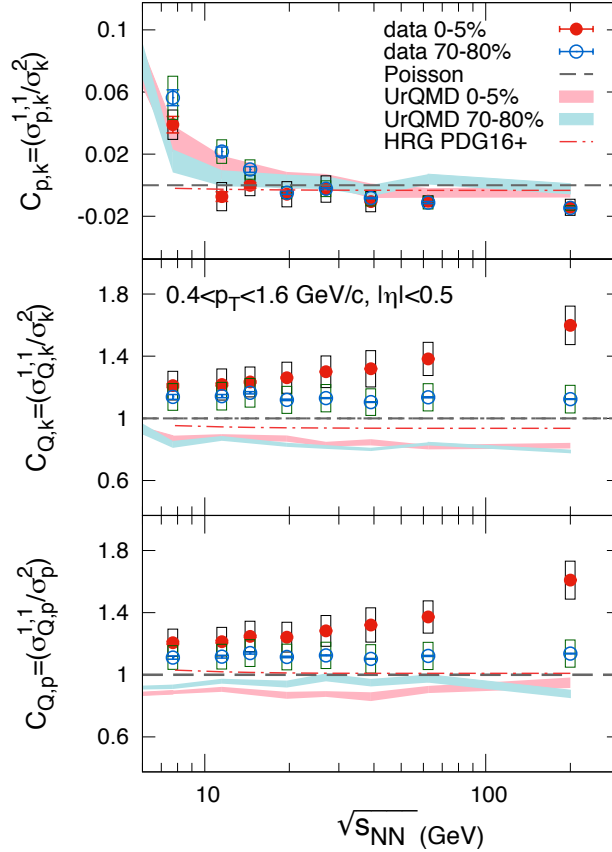


Figure 6.13: Beam energy dependence of off-diagonal to diagonal cumulant ratios of net-charge and net-proton (upper panel) and for net-charge and net-kaon (lower panel) for Au+Au collisions at  $\sqrt{s_{NN}} = 7.7, 11.5, 14.5, 19.6, 27, 39, 62.4$  and 200 GeV. Vertical line and box represent statistical and systematic error, respectively. The broken lines represent the Poisson baseline. The band represents the UrQMD results for 0-5% central collisions.

The Poisson expectation is denoted as dotted lines, and the UrQMD calculations for 0-5% central events are represented as red/blue bands. We find that the value of  $\sigma_{p,k}^{11}/\sigma_k^2$  decrease with increase in energy.  $\sigma_{p,k}^{11}/\sigma_k^2$  is positive at lower energies whereas negative at higher energy and the sign changes happens around 14.5-19.6 GeV. This indicates that at lower energies net-proton and net-kaon are more correlated and they are anti-correlated at higher energies.  $\sigma_{Q,p}^{11}/\sigma_p^2$  and  $\sigma_{Q,k}^{11}/\sigma_k^2$  are increases linearly for 0-5% central collision as a function of beam energy. Both HRG and UrQMD models under-predict the data and can not describe the strong energy dependence of  $C_{Q,k}$  and  $C_{Q,p}$ .

Let us first discuss the trend of net-proton and net-kaon correlated fluctuations. Total proton and kaon correlated fluctuations were previously reported by STAR and NA49 collaborations [117, 118]. However, in this work, we measure the correlated fluctuation in the net-quantities.  $C_{p,k}$  shows a very weak energy dependence above beam energy 20 GeV in both central and peripheral events. The HRG calculation for  $C_{p,k}$  is close to zero. The UrQMD model produces values consistent with zero at higher energies within the uncertainties. From Fig. 6.13, we can observe that the  $C_{p,k}$  is significantly positive ( $4\sigma$  above zero at 7.7 GeV) at lowest BES energy and significantly negative ( $3\sigma$  below zero at 200 GeV) at higher energies. Resonance decays, like,  $\Lambda(1520) \rightarrow pK^-$  ( $22.5 \pm 0.5\%$ ) can contribute to  $C_{p,k}$  [119]. This decay can increase the net-proton number but shall decrease the net-kaon number, resulting in a negative  $p$ - $K$  correlation. This cannot be responsible for a positive  $C_{p,K}$  value in lower energies. The associated production  $pp \rightarrow p\Lambda(1115)K^+$  may contribute to the positive correlation in  $C_{p,k}$  [120]. Such hadronic scattering process occurs more in lower energies due to presence of more proton and will associate with more production of positive kaon resulting in a positive value of  $C_{p,k}$  correlation. This mechanism is already implemented in the UrQMD model [115] and may explained the trend seen in Fig. 6.13. It must be noted that associated production is followed by the resonance decay  $\Lambda(1115) \rightarrow p + \pi^-$

(with a branching ratio of 63.9%) further contributes to a positive net-proton to net-kaon correlation. We find that, in the UrQMD model, the forced decay of all produced  $\Lambda(1115)$  increase the  $C_{p,k}$  by about 30% at 7.7 GeV (Appendix A). However, we find a negligible effect at higher energies due to the equal production of  $\Lambda$  and anti- $\Lambda$ 's. In the QGP phase, the positive strangeness is carried by a strange anti-quark and associated with a negative baryon number. This strong anti-correlation between net-strangeness and net-baryon in the QGP phase is expected to have weak  $T$  and  $\mu_B$  dependence [59]. Since changing  $\sqrt{s_{NN}}$  changes both  $T$  and  $\mu_B$ , it is not straightforward to directly compare the  $\sqrt{s_{NN}}$  dependence of  $C_{p,k}$  shown in Fig. 6.13 to the behavior predicted for  $C_{B,S}$  in [59]. Nevertheless, the current data on  $C_{p,k}$  may provide some important insights into baryon-strangeness correlations that are expected to change at the onset of de-confinement. On the other hand, a very different trend is observed in  $C_{Q,k}$  and  $C_{Q,p}$ . Both observables show significantly higher values in central (0-5%) events compares to peripheral (70-80%) events. The excess correlation in  $C_{Q,k}$  and  $C_{Q,p}$  cannot be explained by both thermal (HRG) and non-thermal (UrQMD) predictions of hadrons.  $C_{Q,p}$  gets contribution from  $\Delta^{++} \rightarrow \pi^+ + p$  [121]. The double charge of  $\Delta^{++}$  simultaneously increase both net-charge and net-proton. On the other hand, resonance decays like  $K^{*0}(892) \rightarrow \pi^\pm + K^\mp$  or  $\phi(1020) \rightarrow K^+ + K^-$  [121] will not change  $C_{Q,k}$  as they do not lead to correlated production of net-charge and net-kaon. Decays like  $K^{*\pm}(892) \rightarrow K_S^0 + \pi^\pm$  increases both the net-strangeness and the net-charge in the system. However, It is not clear such decays lead to correlated production of net-kaon and net-charge, therefore, a small contribution to  $C_{Q,k}$  from hadronic phase is not unexpected. Definitely more theoretical inputs are needed to interpret the excess correlations seen for  $C_{Q,p}$  and  $C_{Q,k}$ , indeed come from the resonance states that have not been included in the existing hadronic models. It will also be important to understand if the growth of these cumulants with collision energy can be explained by model calculations that include contributions from the QGP phase.



## Chapter 7

# Isothermal compressibility estimation from multiplicity fluctuations

A set of various thermodynamic response functions, like, conserved charge susceptibilities, specific heat and compressibility are related to the system equation of state (EOS) and predicted as a useful tool to study the phase diagram of nuclear matter. These response functions are a set of basic macroscopic quantities, such as the pressure, the temperature, the volume, the entropy and energy density. In the previous chapters, we have discussed different conserved charge cumulants in the high-energy nuclear collision by studying net-particle fluctuations which are expected to provide information about conserved charge susceptibilities. In this chapter, we will discuss the first estimation of isothermal compressibility ( $k_T$ ) of hadronic matter formed in relativistic nuclear collisions [122].

The isothermal compressibility of a system is defined by the relative change of the system volume due to a change in the pressure at constant temperature. Thus,  $k_T$  can be expressed as the second derivative of the free energy w.r.t. the pressure which is expected to show a singularity in a second order phase transition. The study of  $k_T$  can provide information about the

nature of the transition [123, 124, 125]. The Lattice QCD calculations have shown that at zero baryon chemical potential, there is crossover transition between quark-gluon plasma phase and hadronic phase [13]. On the other hand, QCD inspired phenomenological models foresee a first order phase transition at high  $\mu_B$  [126, 127]. This suggests there should exist a QCD critical point where the first order transition terminates [128]. The current focus of experimental and theoretical programs is to understand the phase diagram and to locate the critical point by exploring multiple observables. Since isothermal compressibility is sensitive to the phase transition, its study on the  $\mu_B$  dependency can be a useful measurement in this direction.

Here we have estimated the  $k_T$  of the system created in high energy heavy-ion collisions using event-by-event particle number fluctuations in the mid-rapidity region, as prescribed in reference [123]. In previous studies, it had been proposed that enhanced fluctuations of produced multiplicity is a signature of phase transition and critical point [37, 32]. The experimental data of event-by-event multiplicity fluctuations at the RHIC and SPS experiment have been used in combination with temperatures and volumes of the system at the chemical freeze-out to extract the values of  $k_T$ . Finally, we compare these results to the hadron resonance gas (HRG) model and three different event generators. These results will provide important measures for the ongoing heavy-ion collisions experimental program at RHIC and LHC. Also, our results give guidance for upcoming experiments at the Facility for Antiproton and Ion Research (FAIR) at GSI and the Nuclotron-based Ion Collider (NICA) at JINR, Dubna.

## 7.1 Observables

Isothermal compressibility ( $k_T$ ) is defined as the relative change in volume given a change in pressure at constant temperature [123],

$$k_T|_{(T, \langle N \rangle)} = -\frac{1}{V} \left( \frac{\partial V}{\partial P} \right)_{(T, \langle N \rangle)}, \quad (7.1)$$

where  $T$  = temperature,  $V$  = volume and  $P$  = pressure of the system.  $\langle N \rangle (= \mu)$  stands for the mean particle yield. In the GCE framework,  $k_T$  is directly related to the mean particle yield and the variance ( $\sigma^2$ ) of the multiplicity distribution, i.e.,

$$\sigma^2 = \frac{k_B T \langle N \rangle^2}{V} k_T, \quad (7.2)$$

where  $k_B$  is the Boltzmann constant. In the experiment, charged particle multiplicity fluctuations are evaluated in terms of the scaled variance ( $\omega_{ch}$ ) of the multiplicity distribution, defined as,

$$\omega_{ch} = \frac{\sigma^2}{\mu} = \frac{\langle N_{ch}^2 \rangle - \langle N_{ch} \rangle^2}{\langle N_{ch} \rangle}, \quad (7.3)$$

Using equation 7.2 and 7.3,  $k_T$  can be expressed in terms of multiplicity fluctuations as follows,

$$k_T = \frac{\omega_{ch} V}{k_B T \mu}. \quad (7.4)$$

In inelastic collisions case, at chemical freeze-out surface, hadron multiplicities get frozen. Ensemble average thermodynamic properties like  $T$  and  $V$  can be extracted from the mean hadron yield and  $k_T$  can be accessed through the measurements of the event-by-event multiplicity fluctu-

ations.

## 7.2 Multiplicity fluctuations from experimental data

Charged particle multiplicity fluctuations were measured for a wide range of collision energies by the E802 Collaboration at BNL-AGS [129], NA49 [130, 131], WA98 [132], NA61 [133], CERES experiments at SPS-CERN [134], and PHENIX experiment at RHIC-BNL [135]. One can note that all these measurements used different kinematic cuts, so they could not be compared directly. Also, different measurement has different detection efficiencies. However, the results from different experiments can be presented on the same footing if properly scaled by pseudorapidity acceptance [136].

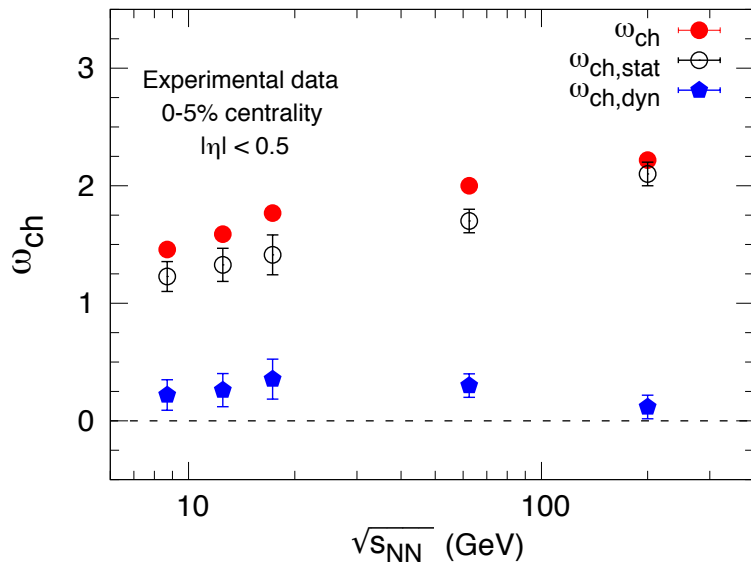


Figure 7.1: Collision-energy dependence of  $\omega_{ch}$  of charged particle multiplicity distributions for central (0-5%) A+A collisions from the available experimental data [135, 129, 130, 131, 134]. The statistical component has been shown using participant model. The dynamical fluctuation is obtained by subtraction the statistical component from the measured values.

The collision energy dependence of  $\omega_{ch}$  values for 0-5% central A + A collisions measured in the

range  $|\eta| < 0.5$  are displayed in Fig. 7.1. The solid circles represent experimental scaled variance values, which is increasing with the increase in collision energy. Both statistical and dynamical components contribute to the width of the charged particle distributions. Only the dynamical components of scaled variance are connected to thermodynamic volume fluctuations. Thus in this work, the dynamical component has been used to extract  $k_T$ . The dynamical component is extracted from observed particle distribution by subtracting the statistical part. Significant contribution to the statistical fluctuations originate from the event-by-event initial collision geometry fluctuation. This is because, in a fixed centrality class, the impact parameters (or,  $N_{part}$  fluctuates) in each event to another. In participant model [32], the  $A + A$  collisions are treated as the superposition of nucleon-nucleon interactions. Thus in a participant model multiplicity fluctuations can be expressed as a superposition of a number of participant fluctuation and the number of produced particle fluctuation per participant. Thus  $\omega_{ch}$  can be expressed as,

$$\omega_{ch} = \omega_n + \langle n \rangle \omega_{N_{part}}, \quad (7.5)$$

where,  $n$  = number of produced charged particles per participant,  $\omega_n$  = fluctuation in  $n$ , and  $\omega_{N_{part}}$  = fluctuation in number of participant. Now,  $\omega_n$  can be calculated assuming the distribution of charge particle follows a binomial distribution [32, 132].

$$\omega_n = 1 - f + f\omega_m, \quad (7.6)$$

here  $f$  denote the fraction of particles in proton-proton ( $p + p$ ) collision. The value of  $\omega_m$  are extracted from the total number of charged particles of  $p + p$  collisions data [137, 138, 132, 139]. In

a narrow centrality bin  $\omega_{N_{\text{part}}}$  close to unity, as observed in peripheral collisions. Using the values of  $\omega_n, \langle n \rangle$  and  $\omega_{N_{\text{part}}}$  the statistical component of  $\omega_{ch}$  then extracted. In Fig. 7.1 the  $\omega_{ch,stat}$  are presented by open symbols as a function of beam energy. Note that the uncertainties in  $\omega_{ch,stat}$  are derived from uncertainties in  $n$  and  $\omega_n$ . In Fig. 7.1 the dynamical fluctuations (represented as  $\omega_{ch,dyn}$ ) are represented by solid diamond symbols and are extracted by subtracting the statistical fluctuations from measured value. Within the error bars, the  $\omega_{ch,dyn}$  remain almost constant with beam energy. However, a diminishing pattern is observed for  $\sqrt{s_{NN}} > 20$  GeV. To conclude the nature of the fluctuations as a function of beam energy more experimental data are needed at low and intermediate energies.

### 7.3 Multiplicity fluctuations from event generators

In this study, we have compared the data results with three different event generators, UrQMD (Ultra-relativistic Quantum Molecular Dynamics) [79, 80], AMPT (A Multi-Phase Transport) [140, 141], and EPOS [142, 143, 144]. In chapter 3, we have already discussed the UrQMD model. Using the AMPT model, charged particle multiplicity fluctuations have been studied for default (DEF) as well as string melting (SM) mode in reference [136]. In the SM mode, hadronization takes place via quark coalescence, whereas in the default mode, hadronization takes place via the string fragmentation. The EPOS is a (3+1) viscous hydrodynamic model incorporating multiple scattering approaches. The hydrodynamical evolution starts from flux tube (or relativistic strings) initial conditions, generated by the Gribov-Regge (GR) framework [144]. The string formation occurs due to initial scatterings, which later breaks into segments identified as hadrons. One of the salient features of the model is the classification of two regions of physical interest on the basis of density, such as core (high density) and corona (low density) [143]. In a centrality dependence mechanism, the corona takes over a major role at low multiplicity and large rapidity events.

However, for central collisions, a core with collective hadronization is created from corona because of a large number of inelastic collisions between nucleons.

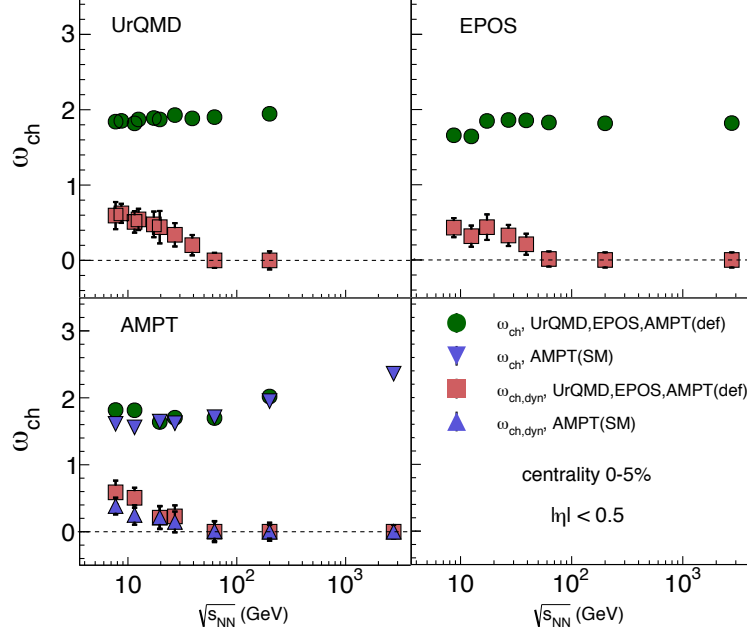


Figure 7.2: Collision energy dependence of  $\omega_{ch}$  of multiplicity distributions for 0-5% central  $A + A$  (Au+Au or Pb+Pb) collisions for AMPT (both DEF and SM), UrQMD and EPOS. The dynamical multiplicity fluctuations ( $\omega_{ch,dyn}$ ) are obtained after subtracting the statistical fluctuations from participant model.

For the present study, we have generated a large number of events for  $Au + Au$  collisions at  $\sqrt{s_{NN}} = 7.7-200$  GeV, corresponding to the RHIC beam energies, and for  $Pb + Pb$  collision at  $\sqrt{s_{NN}} = 2.76$  TeV, corresponding to LHC energies. For all cases, the multiplicity fluctuation has been obtained within the standard kinematic range,  $|\eta| < 0.5$  and  $0.2 < p_T < 2.0$  GeV/c. The centrality selection has been done using the charged particle multiplicities in the range  $-1.0 < p_T < -0.5$  and  $0.5 < p_T < 1.0$  to minimize the auto-correlation effect as described in chapter 5. To minimize the geometrical fluctuation, centrality bin width correction has been done similarly as described in chapter 5.

Figure 7.2 shows the scaled variance for 0-5% central collisions as a function of collision energy from UrQMD, AMPT and EPOS event generators. Statistical uncertainty are calculated using the general error propagation method [66]. It is observed that the fluctuations remain almost constant over the entire energy range in UrQMD and EPOS events. The statistical components of the fluctuations have been estimated from the participant model calculations, using the same procedure as discussed in the previous section. The dynamical components ( $\omega_{ch,dyn}$ ) are also shown in Fig. 7.2 which is obtained after subtracting the statistical fluctuations. It is observed that in all cases the dynamical fluctuations decrease with the increase in energy up to  $\sqrt{s_{NN}} = 62.4$  GeV, beyond which the fluctuations are close to zero. Since resonance decays play an important role for the production of particles, the multiplicity fluctuation results have been studied with resonance decay on as well as resonance decay off for AMPT and EPOS models for Au+Au collisions at  $\sqrt{s_{NN}} = 200$  GeV and Pb+Pb collisions at  $\sqrt{s_{NN}} = 2.76$  TeV, respectively. No significant difference was observed in the two results of scaled variances. So it is inferred that resonance decay effects on multiplicity fluctuations are negligible.

## 7.4 Isothermal compressibility from HRG model

In this study, we have also estimated the isothermal compressibility using the HRG model. In chapter 3, we have already discussed the HRG model. The HRG model has been found to provide a good description of the mean hadron yields using a few thermodynamic parameters at freeze-out (for a recent compilation of the freeze-out parameters see reference [87]).  $k_T$  can be directly calculated in HRG model from equation 7.1, Where instead of total number charged particles the species dependence ( $i$ ) of hadrons used. Then the pressure  $P(T, \{\mu_i\})$  can be expressed as,

$$dP = \left(\frac{\partial P}{\partial T}\right)dT + \sum_i \left(\frac{\partial P}{\partial \mu_i}\right)d\mu_i. \quad (7.7)$$

Then by taking partial derivative w.r.t. volume

$$\left(\frac{\partial P}{\partial V}\right)\Big|_{T,\{N_i\}} = \sum_i \left(\frac{\partial P}{\partial \mu_i}\right)\left(\frac{\partial \mu_i}{\partial V}\right)\Big|_{T,\{N_i\}}, \quad (7.8)$$

where the first factor is to compute from the equation for  $P$  and the second factor  $\left(\frac{\partial \mu_i}{\partial V}\right)\Big|_{T,\{N_i\}}$  is computed from the condition of constancy of  $N_i$  as follows,

$$dN_i = \left(\frac{\partial N_i}{\partial T}\right)dT + \left(\frac{\partial N_i}{\partial V}\right)dV + \left(\frac{\partial N_i}{\partial \mu_i}\right)d\mu_i. \quad (7.9)$$

Now, when  $N_i$  is fixed, the above equation becomes,

$$\left(\frac{\partial \mu_i}{\partial V}\right)\Big|_{T,\{N_i\}} = \frac{\left(\frac{\partial N_i}{\partial V}\right)}{\left(\frac{\partial N_i}{\partial \mu_i}\right)}. \quad (7.10)$$

Within ideal thermal gas,  $\frac{\partial N_i}{\partial V} = \frac{\partial P}{\partial \mu_i}$ . Thus, equation 7.8 becomes

$$\left(\frac{\partial P}{\partial V}\right)\Big|_{T,\{N_i\}} = \sum_i \frac{\left(\frac{\partial P}{\partial \mu_i}\right)^2}{\left(\frac{\partial N_i}{\partial \mu_i}\right)}, \quad (7.11)$$

finally  $k_T$  can be expressed as,

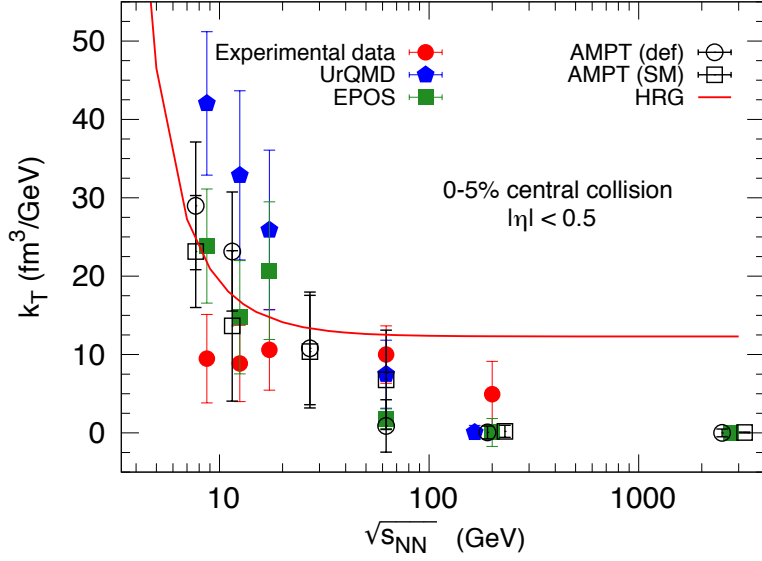


Figure 7.3: Isothermal compressibility ( $k_T$ ) for available experimental data for 0-5% central Au+Au (Pb+Pb) collisions as a function of collision energy. Results for presented for three different event generators, AMPT, UrQMD and EPOS. A uniform pseudo-rapidity cut ( $|\eta| < 0.5$ ) has been maintained for all cases. Results from HRG calculations are superimposed.

$$k_T|_{T,\{N_i\}} = \frac{1}{V} \frac{1}{\sum_i \left( \frac{\partial P}{\partial \mu_i} \right)^2 / \left( \frac{\partial N_i}{\partial \mu_i} \right)}. \quad (7.12)$$

Using the above prescription, the  $k_T$  has been calculated in the HRG model for  $Au + Au$  collisions as a function of beam energy, as presented in the solid curve in Fig. 7.3. It is observed that  $k_T$  decrease with collision energy up to  $\sqrt{s_{\text{NN}}} = 20$  GeV, beyond which it remain almost constant. This implies that even at the hadronic freeze-out stages, the nature of the matter produced is very different at low energies compared to that of the high energy nuclear collisions.

## 7.5 Compilation of $k_T$

Finally, the values of isothermal compressibility are estimated from available experimental data as well as from event generators using the values of  $\omega_{ch,dyn}$  (presented in Fig. 7.1 and 7.2) and the mean charged particle multiplicities within same kinematic condition. Both the chemical freeze-out temperature ( $T_{ch}$ ) and volume ( $V$ ) are obtained from reference [87].  $T_{ch}$  and  $V$  of the system have been estimated by fitting the experimentally measured identified particle yields using thermal model approach [78, 145, 146, 113, 87].

A compilation of  $k_T$  for central  $A + A$  collisions has been presented in Fig. 7.3. The results are presented as a function  $\sqrt{s_{NN}}$  using available experimental data, HRG calculations as well as three different event generators. From the available experimental data, it is observed that the  $k_T$  remains almost constant within the uncertainties. At the LHC energy, calculations from AMPT and EPOS have been presented. The estimated  $k_T$  values from event generators seem to decrease with an increase in  $\sqrt{s_{NN}}$ . The HRG calculation shows a sharp decrease in  $k_T$  at low  $\sqrt{s_{NN}}$  then remains almost constant at  $\sqrt{s_{NN}} > 20$  GeV. Thus to validate our finding more experimental data points is needed with large precession at lower energies.

It is noted that several sources of uncertainty may affect the extraction of  $k_T$ . The evaluation of the statistical component of the fluctuation may cause one of the most significant sources of uncertainty. In addition the charge particle production from resonance decay may affect the  $k_T$  extraction. To check, we have studied this effect for  $Au + Au$  collision at  $\sqrt{s_{NN}} = 200$  GeV and  $Pb + Pb$  collisions at  $\sqrt{s_{NN}} = 2.76$  TeV using AMPT and EPOS by turning on and off the higher mass resonances. We find a negligible difference (very small and within the error bars) for multiplicity fluctuations. Other sources of fluctuations which affect the extraction of  $\omega_{ch,dyn}$  include uncertainty in the initial state fluctuations and fluctuations in the amount of stopping. Given the uncertainties from different sources which could not be considered presently, the extracted values

are the upper limits of  $k_T$ .

## 7.6 Summary

To summarize, we have estimated the isothermal compressibility of the system formed at the time of chemical freeze-out in heavy-ion collisions for collision energy from 7.7 GeV to 2.76 TeV. We have shown that  $k_T$  is connected to the particle multiplicity fluctuation in the central rapidity region and the multiplicity fluctuations have been obtained from available experimental data and event generators. The dynamical fluctuations ( $\omega_{ch,dyn}$ ) are extracted by subtracting the statistical components from the total fluctuations using contributions from the number of participating nucleons. The chemical freeze-out temperature and volume were taken from the thermal model fits of the experimentally measured particle yields. Within quoted uncertainties, the values of  $k_T$  from the experimental data remain almost constant as a function of  $\sqrt{s_{NN}}$ . Using the event generators, we have seen that  $k_T$  decreases with an increase of the beam energy. The estimation of  $k_T$  relies on several assumptions, most importantly on the estimation of dynamical fluctuations. The results of  $k_T$  represent the upper limits because of unknown contributions to the statistical components. In this work, we have also calculated the values of  $k_T$  from HRG model for a large range of collision energy. The HRG calculation shows a sharp decrease in  $k_T$  at low  $\sqrt{s_{NN}}$  then remains almost constant at  $\sqrt{s_{NN}} > 20$  GeV. A higher value of  $k_T$  at low energies compared to higher energies indicates that the collision system is more compressible at the lower energies. This study gives a strong impetus for the second phase of the beam energy scan program of RHIC and planned experiments at FAIR and NICA.

# Chapter 8

## Summary

The major goals of the RHIC Beam Energy Scan program are to map the QCD phase diagram, understand the phase transition in detail and to search for the Critical point of the phase transition. Study of fluctuations and correlations provide important signals towards achieving these goals. In this thesis, a study of second-order diagonal and off-diagonal cumulants of net-charge, net-proton, and net-kaon multiplicity distribution has been presented in  $Au + Au$  collisions for eight different collision energies,  $\sqrt{s_{NN}} = 7.7, 11.5, 14.5, 19.6, 27, 39, 62.4$  and 200 GeV using STAR detector at RHIC. A detailed simulation study has also been done using HRG and UrQMD model corresponding to a wide range of collision energies from 4 GeV up to 200 GeV. Besides, an estimation of isothermal compressibility at chemical freeze-out has been carried out as a part of the thesis work.

The main motivation of studying off-diagonal susceptibilities is to understand the mechanism behind the correlated production of hadrons that carry different conserved charges. From theoretical calculations using lattice QCD, it is expected that the correlated production of two different conserved charges contains information about the degrees of freedom of the system. The main finding of this STAR data analysis is the following. Within the experimentally available acceptance,

---

we observe strong linear dependence of the off-diagonal cumulants as a function of the pseudo-rapidity window. However, in UrQMD simulation, the growth of the off-diagonal cumulants is weaker than the experimental data. The centrality dependence of cumulants has been studied as a function of  $\langle N_{part} \rangle$ . The diagonal cumulants of net-charge, net-proton and net-kaon increase as a function of  $\langle N_{part} \rangle$  because of the increase in system volume towards central collisions. The width of net-proton distributions decreases as a function of beam energy in the central collision because of baryon stopping at lower energies. The correlations between net-charge and net-kaon, and net-charge and net-proton increase with centrality. On the contrary, there is a growing anti-correlation behaviour observed between net-proton and net-kaon with centrality. At low beam energy ( $\sqrt{s_{NN}} < 27$  GeV), this correlation becomes positive. The centrality dependence of the off-diagonal cumulants  $\sigma_{Q,k}^{1,1}$  and  $\sigma_{Q,p}^{1,1}$  are linearly increased with centrality. We studied the "Koch ratios"  $C_{p,k} = \sigma_{p,k}^{1,1}/\sigma_k^2$ ,  $C_{Q,k} = \sigma_{Q,k}^{1,1}/\sigma_k^2$  and  $C_{Q,p} = \sigma_{Q,p}^{1,1}/\sigma_p^2$  to remove the trivial volume dependence. It is observed that the normalized  $p$ - $k$  correlation is significantly positive ( $4\sigma$  above zero at 7.7 GeV) at the lowest BES energy and significantly negative ( $3\sigma$  below zero at 200 GeV) at higher energies. For top central bins,  $C_{p,k}$  changes sign around 19.6 GeV. HRG and UrQMD model predictions fail to explain the negative value of  $C_{p,k}$  at higher beam energies. The experimental  $C_{p,k}$  data for STAR BES energies will help to understand the baryon-strange correlation that predicted to have different  $T$  and  $\mu_B$  dependence in partonic and hadronic phases. The other ratios,  $C_{Q,p}$  and  $C_{Q,k}$ , are the measure of excess correlation in  $Q$ - $p$  and  $Q$ - $k$ .  $Q$  contains both net-proton and net-kaon. So,  $C_{Q,p}$  and  $C_{Q,k}$  removes the trivial self correlation. Both the ratios growth with energy in the central collision and cannot explain by HRG or UrQMD model. More theoretical inputs are needed to understand the origin of excess correlation. The measurement of full cumulant matrix of net-particle multiplicity distributions as a function of beam energy, centrality and  $\eta$ -acceptance window will improve the estimation of freeze-out parameters extracted by HRG and

lattice calculations that help to map the QCD phase diagram.

There are several limitation and/or effects in the experimental measurements which need to be properly understood to interpret the results and compare with theoretical calculations. A detailed simulation study has been done using HRG and UrQMD model to understand such effects like detector acceptance and particle species dependence in the experimental measurements of the cumulants for heavy-ion collisions. From this model study, we showed that,  $\chi_Q^2$ ,  $\chi_{BQ}^{11}$  and  $\chi_{QS}^{11}$  can be measured accurately with the event-by-event measurements of the limited particle set:  $\pi^\pm$ ,  $K^\pm$ ,  $p$  and  $\bar{p}$ , while the measured  $\chi_B^2$  from net proton roughly scale as half of that expected from the complete particle set due to the missing neutrons. We should have  $|\eta_{\max}| \leq 0.5$  acceptance in order to have the ratio of conserved charge in the bath to the total conserved charge from system and bath much smaller than half as it should be for grand canonical fluctuations at least for all lower beam energies. Finally, in this simulation work, we construct the normalized susceptibilities and cumulants. It is found that the suitably normalized susceptibilities show a conserved charge ordering in the  $p_T$  acceptance in HRG as well as in UrQMD. The net-charge susceptibilities saturate to their maximum value at smaller  $p_{T_{\max}}$  value followed by net strangeness and net baryon. For a thermal medium, the  $p_{T_{\max}}$  dependence arises from the different masses of the relevant degrees of freedom that contribute to these conserved charge fluctuations. For a hadronic medium, this implies a clear ordering in the different conserved charges. Under being normalized, they are independent of the fireball volume and thus can be reliably compared between experiments and theory. Experimental observation of such ordering will confirm the presence of the hadronic medium at the time of freeze-out of the susceptibilities. On the other hand, a negative result will hopefully lead to more interesting physics. It will be interesting in this context to study the influence of critical fluctuations on such ordering.

In addition, as a part of the thesis work, an estimation of isothermal compressibility ( $k_T$ ) at the

---

chemical freeze-out has been carried out using experimentally observed event-by-event multiplicity fluctuations from 7.7 GeV to 2.76 TeV. These estimated results are compared with calculations from different event generators, like AMPT, UrQMD, and EPOS as well as HRG model. The dynamical fluctuations are extracted by subtracting the statistical components from the total fluctuations. The chemical freeze-out temperature and volume were taken from the thermal model fits of the experimentally measured particle yields. Within quoted uncertainties, the values of  $k_T$  from the experimental data remain almost constant as a function of  $\sqrt{s_{NN}}$ . Using the event generators, we have seen that  $k_T$  decreases with an increase of the beam energy. The HRG calculation shows a sharp decrease in  $k_T$  at low  $\sqrt{s_{NN}}$  then remains almost constant at  $\sqrt{s_{NN}} > 20$  GeV. A higher value of  $k_T$  at low energies compared to higher energies indicates that the collision system is more compressible at the lower energies.

The experimental results presented in this thesis are limited by the current acceptance of the STAR detector. It has been proposed that in the second phase of RHIC beam energy scan program (BES-II) the inner Time Projection Chamber (iTTPC) upgrade will provide a wider pseudo-rapidity acceptance ( $|\eta| < 1.7$  unit), better momentum resolution, better  $dE/dx$  resolution as well as better centrality resolution along with EPD upgrade. Therefore, in BES-II program at RHIC, it is possible to measure higher order off-diagonal cumulants with high-statistics data and improved techniques of detector efficiency correction.

## Appendix A

# Effect of $\Lambda$ decay using UrQMD

In chapter 6, we mention that the resonance decay  $\Lambda(1115) \rightarrow p + \pi^-$  (with a branching ratio of 63.9%) can contribute in the positive net-proton to net-kaon correlation. Here we have studied this effect using UrQMD model. In this study, we force decay the  $\Lambda$  (and  $\bar{\Lambda}$ ) to  $p\pi^-$  (and  $\bar{p}\pi^+$ ) and compared the results with decay off events for  $\sqrt{s_{NN}} = 7.7$  and 200 GeV as shown in Fig. A.1.

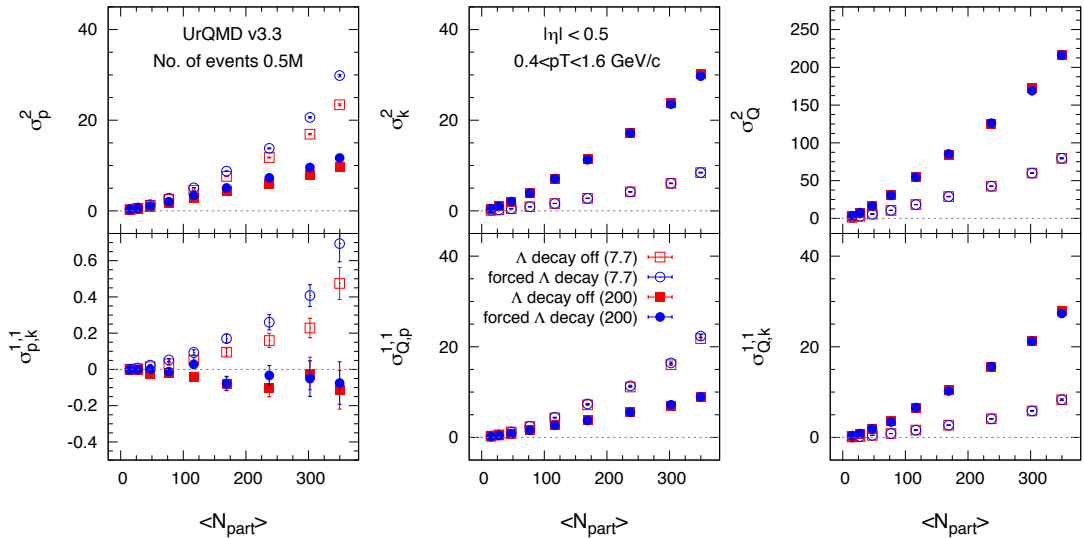


Figure A.1: Effect of  $\Lambda^0$  decay on second order diagonal and off-diagonal cumulants of net-proton, net-charge and net-kaon multiplicity distributions for Au+Au collisions at  $\sqrt{s_{NN}} = 7.7$  (open markers) and 200 (solid markers) GeV using UrQMD model.

We observed almost no difference at 200 GeV. Because at higher energy, lambda and anti-lambda are produced with an equal amount [147]. However, at lower energies, like, 7.7 GeV, there is a small difference observed. From this simulation study, it is apparent that  $\Lambda$ -decay can add a little extra positive correlation to  $\sigma_{BS}$ . It can also be noted that  $\sigma_{QB}$  almost unaffected, because of  $Q$  remain unchanged during the decay.

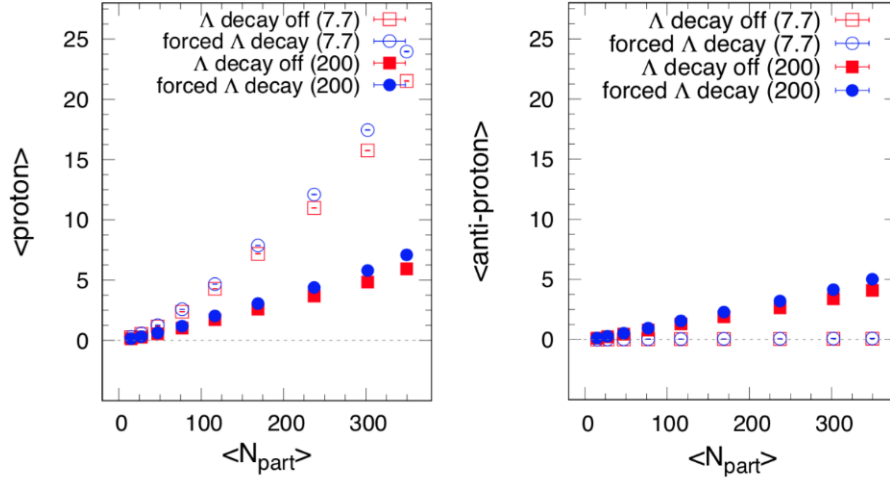


Figure A.2: Effect of  $\Lambda^0$  decay on average  $p$  and  $\bar{p}$  as a function of  $\langle N_{part} \rangle$  for Au+Au collisions at  $\sqrt{S_{NN}} = 7.7$  (open markers) and 200 (solid markers) GeV using UrQMD model.

# Appendix B

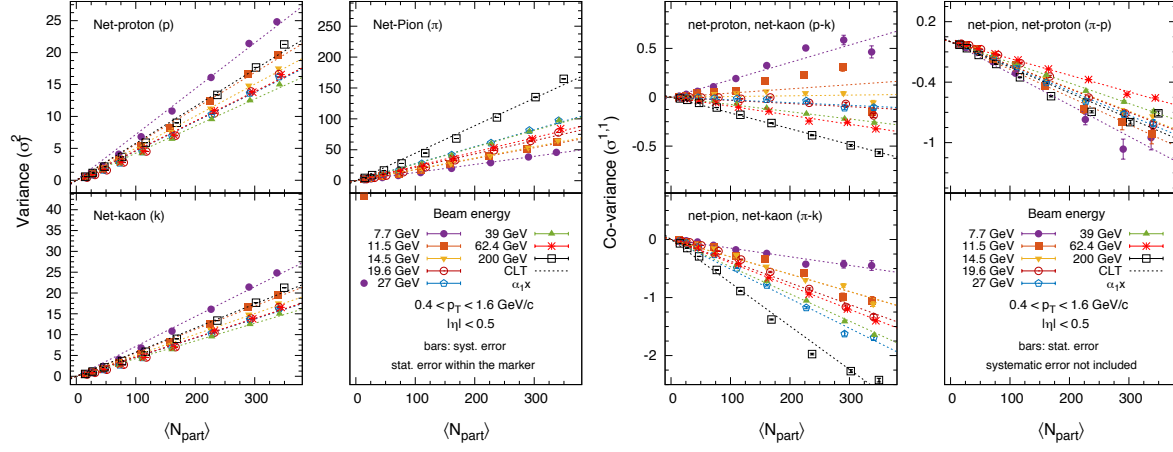
## Net $\pi$ , K, p correlation

### Centrality and acceptance dependence net- $\pi$ , K, p correlation

The centrality dependence  $2^{nd}$ -order diagonal cumulants ( $\sigma^2$ ) of net-proton, net-kaon and net-pion multiplicity distribution for 0-5% most central  $Au+Au$  collisions at  $\sqrt{s_{NN}} = 7.7, 11.5, 14.5, 19.6, 27, 39, 62.4$  and 200 GeV as a function  $\langle N_{part} \rangle$  are shown in Fig. B.1a. The centrality dependence  $2^{nd}$ -order off-diagonal cumulants between net-pion, net-kaon and net-proton are presented in Fig. B.1b. The results are corrected for centrality and finite centrality bin width effect. Both  $\pi$ - $p$  and  $\pi$ - $k$  correlation are negative and increase with centrality. The  $\eta$ -acceptance dependence  $2^{nd}$ -order diagonal and off-diagonal cumulants of net-pion, net-kaon and net-charge for 0-5% most central  $Au + Au$  collisions are shown in Fig. B.1c and B.1d, respectively, at eight different beam energies. A common transverse momentum acceptance ( $0.4 < p_T < 1.6$  GeV/c) is used in this analysis.

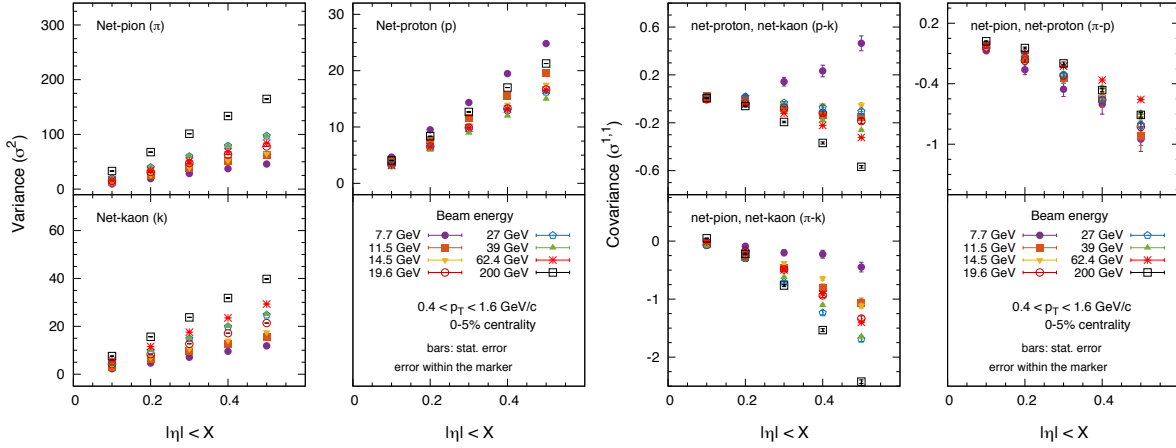
### Energy dependence net- $\pi$ , K, p correlation

The beam energy dependence of cumulant ratios,  $\sigma_{p,k}^{11}/\sigma_p\sigma_k$  (upper panel),  $\sigma_{\pi,p}^{11}/\sigma_\pi\sigma_p$  (middle panel) and  $\sigma_{\pi,k}^{11}/\sigma_\pi\sigma_k$  for two different centrality (0-5% and 70-80%) at  $\sqrt{s_{NN}} = 7.7, 11.5, 14.5,$



(a) Centrality dependence diagonal cumulants

(b) Centrality dependence off-diagonal cumulants



(c)  $\eta$ -window dependence diagonal cumulants

(d)  $\eta$ -window dependence off-diagonal cumulants

Figure B.1: Centrality and acceptance dependence of  $2^{nd}$ -order diagonal and off-diagonal cumulants of net-pion, net-kaon and net-proton multiplicity distributions for  $Au + Au$  collisions at  $\sqrt{s_{NN}} = 7.7, 11.5, 14.5, 19.6, 27, 39, 62.4$  and  $200$  GeV. Error bars are statistical.

19.6, 27, 39, 62.4 and 200 GeV are presented in Fig. 6.13.

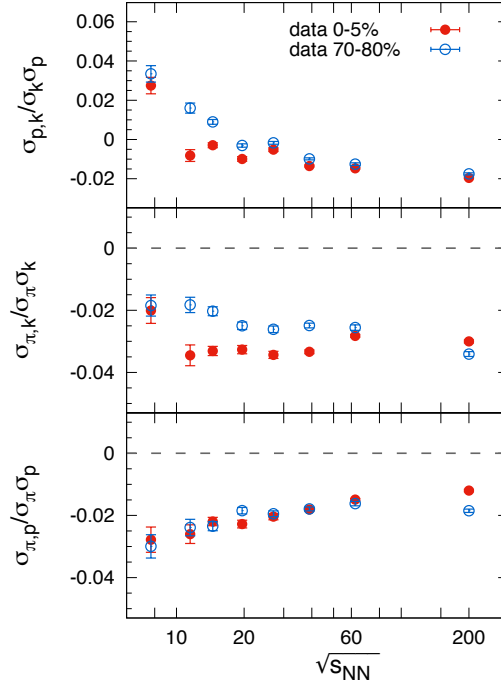


Figure B.2: Beam energy dependence of the ratios of off-diagonal to diagonal cumulants net-charge and net-proton (upper panel) and for net-pion and net-kaon (lower panel) for Au+Au collisions at  $\sqrt{s_{NN}} = 7.7, 11.5, 14.5, 19.6, 27, 39, 62.4$  and 200 GeV.



# Bibliography

- [1] H. Fritzsche and M. Gell-Mann, in *Murray Gell-Mann: Selected Papers* (World Scientific, 2010) pp. 241–261.
- [2] M. Gell-Mann, in *Murray Gell-Mann: Selected Papers* (World Scientific, 2010) pp. 128–145.
- [3] D. H. Perkins, *Introduction to high energy physics* (Cambridge University Press, 2000).
- [4] D. J. Gross and F. Wilczek, *Physical Review Letters* **30**, 1343 (1973).
- [5] H. D. Politzer, *Physical Review Letters* **30**, 1346 (1973).
- [6] S. Bethke, *Nuclear Physics B-Proceedings Supplements* **234**, 229 (2013).
- [7] J. C. Collins and M. J. Perry, *Physical Review Letters* **34**, 1353 (1975).
- [8] E. V. Shuryak, *Physics Letters B* **78**, 150 (1978).
- [9] F. Karsch, in *Lectures on quark matter* (Springer, 2002) pp. 209–249.
- [10] F. Karsch, arXiv preprint hep-ph/0103314 (2001).
- [11] A. Bazavov, T. Bhattacharya, M. Cheng, C. DeTar, H.-T. Ding, S. Gottlieb, R. Gupta, P. Hegde, U. M. Heller, F. Karsch, *et al.*, *Physical Review D* **85**, 054503 (2012).
- [12] Y. Aoki, Z. Fodor, S. Katz, and K. Szabo, *Physics Letters B* **643**, 46 (2006).

- [13] Y. Aoki, G. Endrődi, Z. Fodor, S. Katz, and K. Szabo, *Nature* **443**, 675 (2006).
- [14] S. Ejiri, *Physical Review D* **78**, 074507 (2008).
- [15] K. Rajagopal and F. Wilczek, in *At The Frontier of Particle Physics: Handbook of QCD (In 3 Volumes)* (World Scientific, 2001) pp. 2061–2151.
- [16] H. Satz, arXiv preprint arXiv:0903.2778 (2009).
- [17] A. Adare, S. Afanasiev, C. Aidala, N. Ajitanand, Y. Akiba, H. Al-Bataineh, J. Alexander, A. Al-Jamel, K. Aoki, L. Aphecetche, *et al.*, *Physical Review Letters* **104**, 132301 (2010).
- [18] J. Rafelski and B. Müller, *Physical Review Letters* **48**, 1066 (1982).
- [19] G. Agakishiev, M. Aggarwal, Z. Ahammed, A. Alakhverdyants, I. Alekseev, J. Alford, B. Anderson, C. Anson, D. Arkhipkin, G. Averichev, *et al.*, *Physical Review Letters* **108**, 072301 (2012).
- [20] T. Matsui and H. Satz, *Physics Letters B* **178**, 416 (1986).
- [21] A. Adare, S. Afanasiev, C. Aidala, N. Ajitanand, Y. Akiba, H. Al-Bataineh, J. Alexander, A. Al-Jamel, K. Aoki, L. Aphecetche, *et al.*, *Physical review letters* **98**, 232301 (2007).
- [22] A. Adare, S. Afanasiev, C. Aidala, N. Ajitanand, Y. Akiba, H. Al-Bataineh, J. Alexander, A. Al-Jamel, K. Aoki, L. Aphecetche, *et al.*, *Physical review letters* **101**, 232301 (2008).
- [23] C. Adler, Z. Ahammed, C. Allgower, J. Amonett, B. Anderson, M. Anderson, G. Averichev, J. Balewski, O. Barannikova, L. Barnby, *et al.*, *Physical Review Letters* **89**, 202301 (2002).
- [24] M. L. Miller, K. Reygers, S. J. Sanders, and P. Steinberg, *Annu. Rev. Nucl. Part. Sci.* **57**, 205 (2007).

- 
- [25] J. Adams, C. Adler, M. Aggarwal, Z. Ahammed, J. Amonett, B. Anderson, M. Anderson, D. Arkhipkin, G. Averichev, S. Badyal, *et al.*, Physical Review Letters **91**, 072304 (2003).
- [26] A. Saini and S. Bhardwaj, Journal of Nuclear and Particle Physics **4**, 164 (2014).
- [27] R. Fries, B. Müller, C. Nonaka, and S. Bass, Physical Review Letters **90**, 202303 (2003).
- [28] D. Molnar and S. A. Voloshin, Physical Review Letters **91**, 092301 (2003).
- [29] J. Adams, C. Adler, M. Aggarwal, Z. Ahammed, J. Amonett, B. Anderson, M. Anderson, D. Arkhipkin, G. Averichev, S. Badyal, *et al.*, Physical Review Letters **92**, 052302 (2004).
- [30] J. Adams, M. Aggarwal, Z. Ahammed, J. Amonett, B. Anderson, D. Arkhipkin, G. Averichev, S. Badyal, Y. Bai, J. Balewski, *et al.*, Physical Review C **72**, 014904 (2005).
- [31] B. Abelev, M. Aggarwal, Z. Ahammed, B. Anderson, D. Arkhipkin, G. Averichev, Y. Bai, J. Balewski, O. Barannikova, L. Barnby, *et al.*, Physical Review C **75**, 054906 (2007).
- [32] H. Heiselberg, Physics Reports **351**, 161 (2001).
- [33] J. Randrup, V. Koch, and A. Majumder, in *AIP Conference Proceedings*, Vol. 842 (AIP, 2006) pp. 95–97.
- [34] L. Stodolsky, Physical review letters **75**, 1044 (1995).
- [35] E. V. Shuryak, Physics Letters B **423**, 9 (1998).
- [36] S. Basu, S. Chatterjee, R. Chatterjee, T. K. Nayak, and B. K. Nandi, Physical Review C **94**, 044901 (2016).
- [37] M. Stephanov, K. Rajagopal, and E. Shuryak, Physical Review Letters **81**, 4816 (1998).
- [38] S. Jeon and V. Koch, arXiv preprint hep-ph/0304012 (2003).

- [39] S. Gupta, arXiv preprint arXiv:1508.01136 (2015).
- [40] L. Landau, *Course of Theoretical Physics* **5** (1980).
- [41] V. Koch, in *Relativistic Heavy Ion Physics* (Springer, 2010) pp. 626–652.
- [42] E. V. Shuryak and M. A. Stephanov, *Physical Review C* **63**, 064903 (2001).
- [43] M. Stephanov, *Physical review letters* **102**, 032301 (2009).
- [44] F. Karsch and K. Redlich, *Physics Letters B* **695**, 136 (2011).
- [45] R. Gavai and S. Gupta, *Physics Letters B* **696**, 459 (2011).
- [46] M. Stephanov, *Physical review letters* **107**, 052301 (2011).
- [47] C. Ratti, M. A. Thaler, and W. Weise, *Physical Review D* **73**, 014019 (2006).
- [48] B.-J. Schaefer, J. M. Pawłowski, and J. Wambach, *Physical Review D* **76**, 074023 (2007).
- [49] V. Skokov, B. Friman, and K. Redlich, *Physics Letters B* **708**, 179 (2012).
- [50] L. Adamczyk, J. Adkins, G. Agakishiev, M. Aggarwal, Z. Ahammed, I. Alekseev, J. Alford, C. Anson, A. Aparin, D. Arkhipkin, *et al.*, *Physical Review Letters* **112**, 032302 (2014).
- [51] L. Adamczyk, J. Adkins, G. Agakishiev, M. Aggarwal, Z. Ahammed, I. Alekseev, J. Alford, C. Anson, A. Aparin, D. Arkhipkin, *et al.*, *Physical review letters* **113**, 092301 (2014).
- [52] A. Adare, S. Afanasiev, C. Aidala, N. Ajitanand, Y. Akiba, R. Akimoto, H. Al-Bataineh, J. Alexander, H. Al-Ta'ani, A. Angerami, *et al.*, *Physical Review C* **93**, 011901 (2016).
- [53] L. Adamczyk, J. Adams, J. Adkins, G. Agakishiev, M. Aggarwal, Z. Ahammed, N. Ajitanand, I. Alekseev, D. Anderson, R. Aoyama, *et al.*, *Physics Letters B* **785**, 551 (2018).
- [54] X. Luo and N. Xu, *Nuclear Science and Techniques* **28**, 112 (2017).

- 
- [55] S. He, X. Luo, Y. Nara, S. Esumi, and N. Xu, *Physics Letters B* **762**, 296 (2016).
- [56] J. Xu, S. Yu, F. Liu, X. Luo, *et al.*, *Physical Review C* **94**, 024901 (2016).
- [57] R. Gavai and S. Gupta, *Physical Review D* **73**, 014004 (2006).
- [58] A. Majumder and B. Müller, *Physical Review C* **74**, 054901 (2006).
- [59] V. Koch, A. Majumder, and J. Randrup, *Physical review letters* **95**, 182301 (2005).
- [60] A. Bazavov, H.-T. Ding, P. Hegde, O. Kaczmarek, F. Karsch, E. Laermann, Y. Maezawa, S. Mukherjee, H. Ohno, P. Petreczky, *et al.*, *Physical review letters* **111**, 082301 (2013).
- [61] A. Bazavov, H.-T. Ding, P. Hegde, O. Kaczmarek, F. Karsch, E. Laermann, Y. Maezawa, S. Mukherjee, H. Ohno, P. Petreczky, *et al.*, *Physical review letters* **113**, 072001 (2014).
- [62] F. Karsch, *Nuclear Physics A* **967**, 461 (2017).
- [63] V. Vovchenko, M. I. Gorenstein, and H. Stoecker, *Physical review letters* **118**, 182301 (2017).
- [64] A. Chatterjee, S. Chatterjee, T. K. Nayak, and N. R. Sahoo, *Journal of Physics G: Nuclear and Particle Physics* **43**, 125103 (2016).
- [65] Z. Yang, X. Luo, B. Mohanty, *et al.*, *Physical Review C* **95**, 014914 (2017).
- [66] M. G. Kendall, *Advanced Theory Of Statistics Vol-I* (Charles Griffin: London, 1943).
- [67] E. Lukacs, (1970).
- [68] M. Abramowitz and I. A. Stegun, *Handbook of mathematical functions: with formulas, graphs, and mathematical tables*, Vol. 55 (Courier Corporation, 1965).
- [69] A. Bonyár, in *Design and Technology in Electronic Packaging (SIITME), 2015 IEEE 21st International Symposium for* (IEEE, 2015) pp. 25–30.

- [70] Wikipedia contributors, “[Cumulant — Wikipedia, the free encyclopedia](#),” (2010).
- [71] R. Pathria and P. Beale, *Statistical Mechanics* (Elsevier Science, 1996).
- [72] P. Alba, W. Alberico, R. Bellwied, M. Bluhm, V. M. Sarti, M. Nahrgang, and C. Ratti, *Physics Letters B* **738**, 305 (2014).
- [73] A. Bazavov, H.-T. Ding, P. Hegde, O. Kaczmarek, F. Karsch, E. Laermann, S. Mukherjee, P. Petreczky, C. Schmidt, D. Smith, *et al.*, *Physical review letters* **109**, 192302 (2012).
- [74] S. Borsányi, Z. Fodor, S. Katz, S. Krieg, C. Ratti, and K. Szabo, *Physical review letters* **111**, 062005 (2013).
- [75] G. Odyniec, in *Journal of Physics: Conference Series*, Vol. 455 (IOP Publishing, 2013) p. 012037.
- [76] M. Aggarwal, Z. Ahammed, A. Alakhverdyants, I. Alekseev, B. Anderson, D. Arkhipkin, G. Averichev, J. Balewski, L. Barnby, S. Baumgart, *et al.*, arXiv preprint arXiv:1007.2613 (2010).
- [77] P. Braun-Munzinger, K. Redlich, and J. Stachel, in *Quark–Gluon Plasma 3* (World Scientific, 2004) pp. 491–599.
- [78] J. Cleymans, H. Oeschler, K. Redlich, and S. Wheaton, *Physical Review C* **73**, 034905 (2006).
- [79] M. Bleicher, E. Zabrodin, C. Spieles, S. A. Bass, C. Ernst, S. Soff, L. Bravina, M. Belkacem, H. Weber, H. Stöcker, *et al.*, *Journal of Physics G: Nuclear and Particle Physics* **25**, 1859 (1999).

- [80] S. A. Bass, M. Belkacem, M. Bleicher, M. Brandstetter, L. Bravina, C. Ernst, L. Gerland, M. Hofmann, S. Hofmann, J. Konopka, *et al.*, Progress in Particle and Nuclear Physics **41**, 255 (1998).
- [81] M. Bleicher, S. Jeon, and V. Koch, Physical Review C **62**, 061902 (2000).
- [82] M. Bleicher, M. Belkacem, C. Ernst, H. Weber, L. Gerland, C. Spieles, S. A. Bass, H. Stöcker, and W. Greiner, Physics Letters B **435**, 9 (1998).
- [83] S. Haussler, H. Stöcker, and M. Bleicher, Physical Review C **73**, 021901 (2006).
- [84] N. R. Sahoo, S. De, and T. K. Nayak, Physical Review C **87**, 044906 (2013).
- [85] B. Sharma, M. M. Aggarwal, N. R. Sahoo, and T. K. Nayak, Physical Review C **91**, 024909 (2015).
- [86] K. A. Olive, P. D. Group, *et al.*, Chinese Physics C **38**, 090001 (2014).
- [87] S. Chatterjee, S. Das, L. Kumar, D. Mishra, B. Mohanty, R. Sahoo, and N. Sharma, Advances in High Energy Physics **2015** (2015).
- [88] J. Steinheimer and M. Bleicher, Journal of Physics G: Nuclear and Particle Physics **43**, 015104 (2015).
- [89] J. Steinheimer, Phys. Rev. C **93**, 064908 (2016).
- [90] A. Bzdak and V. Koch, Physical Review C **86**, 044904 (2012).
- [91] M. Bleicher, Phys. Rev. C **62**, 061902 (2000).
- [92] A. Bzdak, V. Koch, and V. Skokov, Physical Review C **87**, 014901 (2013).
- [93] A. Bzdak and V. Koch, Physical Review C **91**, 027901 (2015).

- [94] F. Karsch, K. Morita, and K. Redlich, *Physical Review C* **93**, 034907 (2016).
- [95] H. Petersen, D. Oliinychenko, J. Steinheimer, and M. Bleicher, *Nuclear Physics A* **956**, 336 (2016).
- [96] M. Nahrgang, T. Schuster, M. Mitrovski, R. Stock, and M. Bleicher, *The European Physical Journal C* **72**, 2143 (2012).
- [97] H. Hahn, E. Forsyth, H. Foelsche, M. Harrison, J. Kewisch, G. Parzen, S. Peggs, E. Raka, A. Ruggiero, A. Stevens, *et al.*, *Nuclear Instruments and Methods in Physics Research Section A: Accelerators, Spectrometers, Detectors and Associated Equipment* **499**, 245 (2003).
- [98] M. Aggarwal, S. Badyal, P. Bhaskar, V. Bhatia, S. Chattopadhyay, S. Das, R. Datta, A. Dubey, M. D. Majumdar, M. Ganti, *et al.*, *Nuclear Instruments and Methods in Physics Research Section A: Accelerators, Spectrometers, Detectors and Associated Equipment* **499**, 751 (2003).
- [99] S. collaboration, “detector subsystem documentation,” <https://www.star.bnl.gov/central/experiment/subsystems.php> (1988).
- [100] M. Anderson, J. Berkovitz, W. Betts, R. Bossingham, F. Bieser, R. Brown, M. Burks, M. C. de la Barca Sánchez, D. Cebra, M. Cherney, *et al.*, *Nuclear Instruments and Methods in Physics Research Section A: Accelerators, Spectrometers, Detectors and Associated Equipment* **499**, 659 (2003).
- [101] H. Bichsel, *Nuclear Instruments and Methods in Physics Research Section A: Accelerators, Spectrometers, Detectors and Associated Equipment* **562**, 154 (2006).
- [102] W. Llope, F. Geurts, J. Mitchell, Z. Liu, N. Adams, G. Eppley, D. Keane, J. Li, F. Liu,

- L. Liu, *et al.*, Nuclear Instruments and Methods in Physics Research Section A: Accelerators, Spectrometers, Detectors and Associated Equipment **522**, 252 (2004).
- [103] J. Adams, M. Aggarwal, Z. Ahammed, J. Amonett, B. Anderson, D. Arkhipkin, G. Averichev, S. Badyal, Y. Bai, J. Balewski, *et al.*, Physics Letters B **616**, 8 (2005).
- [104] C. Adler, A. Denisov, E. Garcia, M. Murray, H. Stroebele, and S. White, Nuclear Instruments and Methods in Physics Research Section A: Accelerators, Spectrometers, Detectors and Associated Equipment **470**, 488 (2001).
- [105] H. Appelshäuser, J. Bächler, S. Bailey, L. Barnby, J. Bartke, R. Barton, H. Białkowska, C. Blyth, R. Bock, C. Bormann, *et al.*, The European Physical Journal A-Hadrons and Nuclei **2**, 383 (1998).
- [106] D. Kharzeev and M. Nardi, Physics Letters B **507**, 121 (2001).
- [107] X. Luo, J. Xu, B. Mohanty, and N. Xu, Journal of Physics G: Nuclear and Particle Physics **40**, 105104 (2013).
- [108] J. Adam *et al.* (STAR), (2019), [arXiv:1903.05370 \[nucl-ex\]](https://arxiv.org/abs/1903.05370) .
- [109] [STAR note:  \$V\_z\$  correction](#).
- [110] C. Lippmann, Nuclear Instruments and Methods in Physics Research Section A: Accelerators, Spectrometers, Detectors and Associated Equipment **666**, 148 (2012).
- [111] M. Shao, O. Barannikova, X. Dong, Y. Fisyak, L. Ruan, P. Sorensen, and Z. Xu, Nuclear Instruments and Methods in Physics Research Section A: Accelerators, Spectrometers, Detectors and Associated Equipment **558**, 419 (2006).

- [112] The effect of efficiency correction and error calculations are implemented in the open-source package, **SMoment**. The code package can be downloaded from <https://github.com/ptribedy/SMoment>.
- [113] B. Abelev, M. Aggarwal, Z. Ahammed, B. Anderson, D. Arkhipkin, G. Averichev, Y. Bai, J. Balewski, O. Barannikova, L. Barnby, *et al.*, *Physical Review C* **79**, 034909 (2009).
- [114] L. Adamczyk, J. Adkins, G. Agakishiev, M. Aggarwal, Z. Ahammed, N. Ajitanand, I. Alekseev, D. Anderson, R. Aoyama, A. Aparin, *et al.*, *Physical Review C* **96**, 044904 (2017).
- [115] C. Zhou, J. Xu, X. Luo, F. Liu, *et al.*, *Physical Review C* **96**, 014909 (2017).
- [116] STAR, [STAR Note SN0666 \(2016\)](https://drupal.star.bnl.gov/STAR/starnotes/public/sn0666), <https://drupal.star.bnl.gov/STAR/starnotes/public/sn0666>.
- [117] L. Adamczyk, J. Adkins, G. Agakishiev, M. Aggarwal, Z. Ahammed, I. Alekseev, J. Alford, A. Aparin, D. Arkhipkin, E. Aschenauer, *et al.*, *Physical Review C* **92**, 021901 (2015).
- [118] T. Anticic, B. Baatar, D. Barna, J. Bartke, H. Beck, L. Betev, H. Białkowska, C. Blume, M. Bogusz, B. Boimska, *et al.*, *Physical Review C* **83**, 061902 (2011).
- [119] C. Patrignani, P. D. Group, *et al.*, *Chinese physics C* **40**, 100001 (2016).
- [120] J. Balewski, A. Budzanowski, H. Dombrowski, W. Eyrich, C. Goodman, D. Grzonka, J. Haidenbauer, C. Hanhart, J. Hauffe, L. Jarczyk, *et al.*, *Physics Letters B* **420**, 211 (1998).
- [121] J. Beringer, J. Arguin, R. Barnett, K. Copic, O. Dahl, D. Groom, C. Lin, J. Lys, H. Murayama, C. Wohl, *et al.*, *Physical Review D-Particles, Fields, Gravitation and Cosmology* **86** (2012).
- [122] M. Mukherjee, S. Basu, A. Chatterjee, S. Chatterjee, S. P. Adhya, S. Thakur, and T. K. Nayak, *Physics Letters B* **784**, 1 (2018).

- [123] S. Mrówczyński, *Physics Letters B* **430**, 9 (1998).
- [124] B. Stokić, B. Friman, and K. Redlich, *Physics Letters B* **673**, 192 (2009).
- [125] A. Mekjian, S. Lee, and L. Zamick, *Physics Letters B* **621**, 239 (2005).
- [126] M. Fukugita, M. Okawa, and A. Ukawa, *Physical Review Letters* **63**, 1768 (1989).
- [127] B.-J. Schaefer and J. Wambach, *Nuclear Physics A* **757**, 479 (2005).
- [128] Z. Fodor and S. D. Katz, *Journal of High Energy Physics* **2004**, 050 (2004).
- [129] T. Abbott, Y. Akiba, D. Alburger, D. Beavis, P. Beery, M. Bloomer, P. Bond, C. Chasman, Z. Chen, Y. Chu, *et al.*, *Physical Review C* **52**, 2663 (1995).
- [130] C. Alt, T. Anticic, B. Baatar, D. Barna, J. Bartke, L. Betev, H. Białkowska, C. Blume, B. Boimska, M. Botje, *et al.*, *Physical Review C* **78**, 034914 (2008).
- [131] C. Alt, T. Anticic, B. Baatar, D. Barna, J. Bartke, L. Betev, H. Białkowska, C. Blume, B. Boimska, M. Botje, *et al.*, *Physical Review C* **75**, 064904 (2007).
- [132] M. Aggarwal, Z. Ahammed, A. Angelis, V. Antonenko, V. Arefiev, V. Astakhov, V. Avdeitchikov, T. Awes, P. Baba, S. Badyal, *et al.*, *Physical Review C* **65**, 054912 (2002).
- [133] N. Abgrall, A. Aduszkiewicz, B. Andrieu, T. Anticic, N. Antoniou, J. Argyriades, A. Asryan, B. Baatar, A. Blondel, J. Blumer, *et al.*, *Physical Review C* **84**, 034604 (2011).
- [134] H. Sako, H. Appelshäuser, C. Collaboration, *et al.*, *Journal of Physics G: Nuclear and Particle Physics* **30**, S1371 (2004).
- [135] A. Adare, S. S. Adler, S. Afanasiev, C. Aidala, N. Ajitanand, Y. Akiba, H. Al-Bataineh, J. Alexander, A. Al-Jamel, K. Aoki, *et al.*, *Physical Review C* **78**, 044902 (2008).

- [136] M. Mukherjee, S. Basu, S. Choudhury, and T. K. Nayak, *Journal of Physics G: Nuclear and Particle Physics* **43**, 085102 (2016).
- [137] J. Whitmore, *Phys. Rep.* **27**, 187 (1976).
- [138] K. Aamodt, A. A. Quintana, D. Adamová, A. Adare, M. Aggarwal, G. A. Rinella, A. Agocs, S. A. Salazar, Z. Ahammed, N. Ahmad, *et al.*, *Physical Review Letters* **106**, 032301 (2011).
- [139] S. Chatrchyan, V. Khachatryan, A. Sirunyan, A. Tumasyan, W. Adam, T. Bergauer, M. Dragicevic, J. Erö, C. Fabjan, M. Friedl, *et al.*, *The European Physical Journal C* **74**, 3053 (2014).
- [140] Z.-W. Lin, C. M. Ko, B.-A. Li, B. Zhang, and S. Pal, *Physical Review C* **72**, 064901 (2005).
- [141] B. Zhang, C. M. Ko, B.-A. Li, and Z. Lin, *Physical Review C* **61**, 067901 (2000).
- [142] K. Werner, I. Karpenko, T. Pierog, M. Bleicher, and K. Mikhailov, *Physical Review C* **82**, 044904 (2010).
- [143] K. Werner, *Physical review letters* **98**, 152301 (2007).
- [144] K. Werner, B. Guiot, I. Karpenko, and T. Pierog, *Physical Review C* **89**, 064903 (2014).
- [145] P. Braun-Munzinger, J. Stachel, and C. Wetterich, *Physics Letters B* **596**, 61 (2004).
- [146] J. Cleymans, H. Oeschler, K. Redlich, and S. Wheaton, *Physics Letters B* **615**, 50 (2005).
- [147] A. Andronic, P. Braun-Munzinger, and J. Stachel, *Nuclear Physics A* **772**, 167 (2006).